EVALUATION AND ANALYSIS OF SEASAT-A SCANNING MULTICHANNEL MICROWAVE RADIOMETER (SMMR) ANTENNA PATTERN CORRECTION (APC) ALGORITHM

FINAL REPORT FOR SUB-TASK 3: INTERIM T_B VS. FINAL T_B WITH GAUSSIAN COEFFICIENTS

Prepared under JPL contract number 955368 by:

J. L. Kitzis
S. N. Kitzis

Environmental Sensing Algorithm Development Company

8238 Fenwick Street
Sunland, California 91040

May 25, 1979

This work was performed for the Jet Propulsion Laboratory, California Institute of Technology sponsored by the National Aeronautics and Space Administration under Contract NAS7-100.

This report contains information prepared by Environmental Sensing Algorithm Development Company under JPL sub-contract. Its content is not necessarily endorsed by the Jet Propulsion Laboratory, California Institute of Technology, or the National Aeronautics and Space Administration.

ABSTRACT

This report presents a "snapshot" of the work completed to date towards evaluating the brightness temperature data produced by the SMMR final Antenna Pattern Correction (APC) algorithm. As the algorithm evolves, further evaluation will be performed. The current evaluation consists of 1) a direct comparison of the outputs of the final and interim APC algorithms, and 2) an analysis of a possible relationship between observed cross-track gradients in the interim brightness temperatures and a previously noted asymmetry in the antenna temperature data. The results obtained from these two investigations are the subject of this report.

CONTENTS

TABLE

CONTENTS (Continued)

FIGURE

CONTENTS (Continued)

FIGURE

CONTENTS (Continued)

FIGURE

CONTENTS (Continued)

FIGURE

1.0 SUMMARY

This report presents a "snapshot" of the work completed to date towards evaluating the brightness temperature data produced by the SMMR final Antenna Pattern Correction (APC) algorithm. As the algorithm evolves, further evaluation will be performed. The current evaluation consists of 1) a direct comparison of the outputs of the final and interim APC algorithms, and 2) an analysis of a possible relationship between observed cross-track gradients in the interim brightness temperatures (T_B) and a previously noted asymmetry in the antenna temperature (T_A) data.

The more important conclusions of the study are:

(1) As expected, the final APC algorithm appears to diminish sidelobe effects caused by land masses adjacent to the SMMR swath. As also expected, the cells immediately adjacent to land still contain sidelobe contamination.

(2) The brightness temperatures produced by the final APC are often significantly lower than corresponding values produced by the interim APC. This bias is different for each SMMR channel and varies both with scan position and the mean brightness temperature level being observed.

(3) The final brightness temperature values exhibit anomalous behavior at land-sea interfaces in that the values tend to "ring" when crossing such a transition boundary.

(4) It appears that the cross-track gradients present in the interim T_B data may be modeled as a cos β coupling in the T_A data. However, it appears that the sidelobe corrections are introducing additional effects which are masking this relationship in the final T_B data.

2.0 INTRODUCTION

This report summarizes the work completed to date towards evaluating the brightness temperature data produced by the SMMR final APC algorithm. Prior work regarding the interim APC output is documented in references 1 and 2. There are some differences between the interim APC and the final APC in addition to those due to sidelobe corrections. They are attributable to 1) T_A bias corrections, and 2) new values for the cold space sidelobe contributions, which have been added since the time of the first GOASEX workshop. The version of the final APC evaluated here does not contain corrections for Faraday rotation or non-nominal spacecraft attitude. In addition, the sidelobe corrections currently applied in the final algorithm are approximate in that smooth Gaussian functions with constant sidelobe levels beyond a critical cut-off angle are substituted for the actual antenna patterns. The true antenna pattern functions will be incorporated into the APC algorithm in the near future. As the algorithm evolves, further evaluations will be performed.

The current evaluation consists of two principal efforts:

(1) The brightness temperature outputs of the final and interim APC algorithms are directly compared to evaluate the effects of the newly implemented sidelobe corrections.

(2) A previously noted cross-track asymmetry in the antenna temperature data (see reference 1) is investigated in order to account for instrument-induced cross-track gradients observed in the interim brightness temperatures.

The results obtained from these two investigations, along with newly-developed software analysis tools, will be discussed in later sections of this report. Many of the techniques used in the present evaluation were initially developed during the previous Part B study. The software tools and models thus inherited will not be described here as they are already documented in reference 2.

3.0 TECHNICAL DISCUSSION

3.1 Comparison of Final and Interim APC Brightness Temperatures.

Using various software analysis tools, a preliminary comparison of the final and interim APC brightness temperature outputs has been performed. The present comparison has been limited to a relatively small number of SMMR passes due to time constraints. Additional data should be analyzed in order to verify our preliminary conclusions. This additional analysis will be performed shortly as part of the continuing final APC evaluation.

The present comparison of the final and interim APC algorithms has been performed with the primary intent of evaluating the impact of the newly implemented sidelobe corrections. The following results are expected from this type of comparison:

(1) The final and interim algorithms should generally produce similar brightness temperatures at locations farther than 1,000 kilometers from land.

(2) When the SMMR swath crosses a land-sea interface, the final algorithm should produce a sharper change in brightness temperature values than the interim algorithm.

(3) When the SMMR swath parallels a land-sea interface, the output of the final algorithm should be less sensitive to the nearby land than the interim algorithm.

Our initial observations of final and interim output data do not in all cases agree with the expectations listed above. A discussion of these observations follows.

3.1.1 Comparison Without Land Interference. An important analysis tool developed for this study produces computer plots of final and interim brightness temperature values versus latitude. These plots allow a direct comparison to be made between the final and interim outputs. We have extensively studied a portion of orbit number 1255, which appears to exhibit clearer weather conditions than the other available SMMR passes. Sixty plots relating to this orbit segment have been produced.

These sixty plots consist of six sets of ten plots each, corresponding to the ten SMMR channels. Of the six sets, three consist of data from the left, center, and right portions of the SMMR scan for the interim and final algorithms. The remaining three sets consist of similar data except that the final algorithm output values are calculated without applying sidelobe corrections.

A summary of the differences observed between the final and interim values in all sixty plots is displayed in Table 1. The entries in Table 1 were estimated directly from the appropriate plots and represent average differences between the two algorithms in the region between -20° and 5° latitude. The thirty plots corresponding to the sidelobe - corrected final values are displayed as Figures 1.1 through 3.10. Two plots (Figures 4.1 and 4.2) are given as examples of the full set of thirty plots corresponding to the final algorithm without sidelobe corrections.

The following observations are made regarding this set of data:

(1) Between the latitudes of -20° and +5°, the data exhibits generally constant weather conditions, although some small-structure clouds are present, as can be seen in the higher frequency channels. The feature which peaks at about 12° latitude is the northern hemisphere Intertropical Convergence Zone.

(2) In general, the final brightness temperature values which have been corrected for sidelobes show more point-to-point variation then do either the interim values or the final values which have not been corrected for sidelobes. This may be attributable to an effectively higher degree of resolution achieved by the final sidelobe corrections. Alternatively, it may instead be due to "noise" amplification caused by the sidelobe corrections. Further study is needed to determine what is actually causing this effect.

(3) In general, the brightness temperature values produced by the final APC with sidelobe corrections are lower than the corresponding interim values. This is especially true for the 18, 21, and 37 GHz channels. However, as the brightness temperature level rises, the differences between final and interim values diminish, with the final brightness temperatures sometimes rising higher than the interim values.

(4) As can be seen from the middle portion of Table 1, the differences between the two algorithms vary across the scan, being greater at the edges of the swath than at the center. Generally, the differences at one edge of the swath are greater than those at the opposite edge. As will be seen later, the resulting asymmetry causes the cross-track gradients observed in the final algorithm to be different from those observed in the interim. These swath-edge effects may be partially explained by imperfections in the map-derived T_B estimates from outside the swath. These estimates have a larger effect on the cells near the edge of the swath than on those in the center.

(5) As can be seen from the upper portion of Table 1, there are some differences between the interim APC and the final APC without sidelobe corrections. These differences appear to be fairly constant across the scan. They are attributable to two types of constants which have assumed new values since the time of the first GOASEX workshop: 1) a bias correction has been applied to the antenna temperature data used as input to the final APC algorithm, and 2) the constants within the APC which define the cold space sidelobe contributions to the antenna temperatures have been re-evaluated and changed accordingly. The differences shown in the upper portion of Table 1 are the result of these changes. Note that the largest differences correspond to the 6.6 GHz vertical channel.

(6) The entries in the lower portion of Table 1 may be interpreted as the changes in brightness temperatures due solely to the final sidelobe corrections. In most cases, these numbers are much larger than expected.

(7) A very brief examination of similar plots produced for orbits 1178, 1206, and 1212 tends to substantiate the above observations made for orbit 1255.

3.1.2 Comparison for Land-Sea Interface Crossing. We have chosen orbit number 1212 as an example of the SMMR swath's crossing of a coastline. For orbit 1212, the left edge of the SMMR swath (cell 1 for each grid) first crosses the Kenai Peninsula at a latitude of 59°, then the Cook Inlet at 60°, then the Alaskan mainland between 60° and 64°, then the Norton Sound at 64°, and finally crosses the Seward Peninsula at 65°.

Figures 5.1 through 5.10 contain plots of final and interim brightness temperatures for the portion of orbit 1212 between 30° and 70° north latitude. Note that these plots have a different vertical scaling from those displayed in Figures 1 through 4. The following observations are made regarding this set of plots:

(1) The differences between final and interim brightness temperatures generally agree with those tabulated for orbit 1255 in Table 1. As previously discussed in Section 3.1.1, these differences diminish as the overall brightness temperature level rises, with the final values occasionally rising above the interim values. An example of this effect in orbit 1212 is the cloud feature at

45° north latitude. As also discussed in Section 3.1.1, the final values generally show more point-to-point variation than the interim values.

(2) As expected, the brightness temperature values increase sharply at land boundaries, with the higher frequency channels showing a sharper increase than the lower frequency channels. For example, Cook Inlet is imperceptible at the 6.6 and 10.7 GHz channels due to their lower degree of resolution, while it is evident as a sharp decrease in brightness temperature values at 60° latitude for the higher frequency channels.

(3) The final brightness temperature values exhibit anomalous behavior at each land-sea interface, in that the values seem to "ring" when crossing such a transition boundary. The values undershoot the ambient temperature level on the ocean side of the interface, and overshoot the ambient level on the land side. A clear example of this phenomenon appears in Figure 5.5 for the 18 GHz vertical channel. In this plot, the ambient ocean level is 150° K, and the ambient land level is 260° K. An example of "ringing" appears between 59° and 61° north latitude where the final brightness temperature values dip to 145° K, and then overshoot to 270° K. Another example may be seen between 64° and 65° north latitude when the SMMR swath crosses Norton Sound. The most extreme case occurs in Figure 5.10 for the 37 GHz horizontal channel. In this plot, the ambient ocean level is about 135° K, but the "ringing" brightness temperature values decrease to about 90° K at both the first Alaskan coastline crossing and also over Norton Sound.

In most of the observed cases, the oscillation damps out within two cells of the transition boundary. This "ringing" may be caused by sidelobe overcompensation for adjacent cells, which becomes particularly evident near sharp temperature contrasts such as land-sea interfaces. Further refinement of the APC constants may alleviate this problem, but it is unlikely that accurate corrections will ever be possible for those cells immediately adjacent to land.

3.1.3 Comparison for Paralleling a Land-Sea Interface. We have also chosen orbit number 1212 as an example of the SMMR swath following a course parallel and extremely close to land. The right-hand edge of the swath for orbit 1212 runs parallel to the California coastline and comes within 50 kilometers of San Francisco. Plots of brightness temperature cross-track gradients have been produced for both the final and interim APC outputs using the cross-track gradient software documented in Reference 2. Figures 6.1 through 6.5 correspond to the five frequencies of interim APC output, while Figures 7.1 through 7.5 represent final APC output.

Several observations are made regarding these plots:

(1) The gradients shown in these plots are calculated from first-order least-squares curve fits to each row of brightness temperature

cells. These gradients result from both instrument and environmental effects. For example, the feature seen near 48° north latitude is a cloud band intersected diagonally by the SMMR swath. The cloud bank is observed first on the left-hand edge of the swath, causing an apparent negative cross-track gradient, and later on the right-hand edge, resulting in a positive cross-track gradient. The magnitude of this feature varies from channel to channel and is proportional to each channel's sensitivity to atmospheric water content and/or winds associated with the cloud band.

(2) The feature near 38° north latitude is due to sidelobe effects from the nearby California coast. These sidelobe effects appear as positive cross-track gradients since the brightness temperature values on the right-hand edge of the swath are closest to land and are elevated more than those on the left. This feature appears strongest for the 6.6 GHz channels and decreases with increasing frequency due to the narrower beam-widths at the higher frequencies. The sidelobe effect is stronger for the horizontal channels than for the vertical channels due to the fact that the horizontal temperatures over ocean are much lower than the vertical temperatures, whereas both are about the same over land.

(3) As expected, the final APC algorithm diminishes but does not completely remove these sidelobe effects near 38° latitude. This can be seen by comparing the gradient plots for the final APC brightness temperatures with those for the interim temperatures. For instance, the two maximum 6.6 GHz horizontal gradients for the interim data go off-scale with values of 6.14 and 6.32 degrees Kelvin per cell. The two corresponding gradients for the final data have been reduced to 3.34 and 3.56 degrees Kelvin per cell. The corresponding 6.6 GHz vertical gradients have been reduced from 3.30 and 3.26 to 2.46 and 1.77 degrees Kelvin per cell.

(4) Overall, the final APC algorithm would appear to reduce the differences between vertical and horizontal cross-track gradients for each frequency. This is most strikingly true of the 18 GHz channels. As can be seen in Table 7, the gradients for the final 18 GHz data are generally zero. However the RMS values corresponding to these first-order curve fits are extremely high (3 to 4 degrees Kelvin). This is in contrast to the interim 18 GHz data (Table 6), which exhibit non-zero gradients and relatively low RMS values (.5 to 1 degree Kelvin). We conclude that the cross-track variation in final brightness temperature values is not particularly linear, as previously discussed in Section 3.1.1, and thus cannot be approximated accurately by a first-order polynomial. This is substantiated by the numbers given in Table 1 which show non-linear variations in final brightness temperatures across the swath. Therefore, a zero cross-track gradient in the plots presented for the final APC should probably be interpreted as indicating the existence of non-linear variation across the scan rather than zero variation.

3.1.4 Brightness Temperature - Surface Truth Comparison. An additional comparison between final and interim APC brightness temperatures has been performed by comparing each to a set of model-predicted brightness temperatures. The model values are calculated from interpolated sea surface temperature (SST), sea surface wind speed (SSW), and water vapor content (WVC) values, using the same geophysical model as that described in reference 2. The model-calculated brightness temperatures assume a zero cloud liquid water content.

The results presented here represent data from a single block of SMMR APC output from orbit number 1135. This block has been chosen for our analysis because it exhibits significantly less cloud cover than the other blocks for which wind speed data is available. Model brightness temperatures are calculated for the sixteen grid-one locations of this block. The SMMR measured brightness temperature data consists of the cells from each channel's best grid which are located closest to the centers of the sixteen grid-one cells.

The SST data used as surface truth is derived from the National Marine Fisheries Services September monthly average field which is described in reference 1. The SSW data is a wind field provided by V. Cardone which has been produced from ship and buoy measured wind speeds, and SEASAT-A SASS-derived wind speeds. The atmospheric water vapor values are derived from measurements which are meridionally averaged over a full year (see reference 3).

Software has been developed to interpolate all surface truth data types to the locations of the sixteen grid-one cells within a SMMR block. For the block used in this comparison, sea surface temperatures range between 284.1 and 287.1 degrees Kelvin, sea surface wind speeds range from 12.6 to 16.4 meters/second, and water vapor content varies from 1.3 to 1.4 grams/cm^2.

Plots of measured versus calculated brightness temperatures and associated statistics are produced using previously developed software which is documented in reference 2. The plots representing interim APC output are displayed in Figures 8.1 and 8.2, while those containing final APC values are shown in Figures 9.1 and 9.2. Tables 8 and 9 display the biases observed between measured and model-predicted brightness temperatures for each SMMR channel. Several observations are made regarding these results:

(1) In agreement with the middle portion of Table 1, the biases observed for the final APC data are generally lower than those observed for the interim APC. As also indicated in Table 1, there is little difference between the two algorithms for the 6.6 and 10.7 GHz horizontal channels.

(2) As previously noted, the final APC brightness temperatures generally exhibit more scatter than the interim values. This is supported by the fact that the RMS values calculated for the final APC data are significantly larger than those for the interim data for all channels except 6.6 GHz.

(3) In agreement with the results obtained in the Part B study (reference 2), the vertical channels appear to be biased low, whereas the horizontal channels appear to be biased high with respect to model-predicted values. It is very probable, however, that all of the biases in Tables 8 and 9 are somewhat too high due to unmodeled cloud liquid water. In addition, V. Cardone has suggested that the higher wind speeds contained in his wind fields may be too low by about 2 meters/second. If so, this would also tend to elevate the observed biases. If corrections were applied to the observed biases to account for unmodeled cloud and wind speed effects, the positive biases observed for the horizontal channels would be decreased. However, at the same time, the negative biases observed for the vertical channels would become still more negative. Therefore, it appears that the vertical SMMR channels, particularly 18, 21, and 37 GHz, are probably biased low, though it is not possible at this time to accurately quantify these biases.

3.2 Discussion of cosβ Calculation. The present APC algorithms (both interim and final) assume the SMMR antenna ports to be perfectly linearly polarized. However, a cross-track asymmetry observed in the antenna temperature data (see reference 1) and the apparent existence of non-environmental cross-track gradients in the interim T_B values (references 1 and 2) suggest that this assumption may not be altogether valid. In an effort to check the validity of this assumption, we have performed a least-squares fit to averaged antenna temperature data, solving for a cosβ term which characterizes the degree of independent linear polarization of the SMMR antenna ports. A discussion of the techniques used in solving for cosβ follows.

3.2.1 Approach. Reference 4 contains an expression for the SMMR measured antenna temperatures as a function of brightness temperatures and the instrument antenna patterns. This function may be expressed as:

$$T_{A_P} = \frac{1}{\Lambda_p} \int_0^{2\pi} \int_0^{\pi} \left[T_{B_v}(\theta,\phi)\, G_{pv}(\theta,\phi) + T_{B_h}(\theta,\phi)\, G_{ph}(\theta,\phi) \right] d\theta d\phi \qquad \text{(Eq. 1)}$$

where:

$$G_{pv}(\theta,\phi) = g_{pv}(\theta,\phi)\ \cos^2\psi + g_{ph}(\theta,\phi)\ \sin^2\psi + \left[g_{pv}(\theta,\phi)\ g_{ph}(\theta,\phi)\right]^{1/2}\ \sin 2\psi\ \cos\beta_p$$

$$G_{ph}(\theta,\phi) = g_{ph}(\theta,\phi)\ \cos^2\psi + g_{pv}(\theta,\phi)\ \sin^2\psi - \left[g_{pv}(\theta,\phi)\ g_{ph}(\theta,\phi)\right]^{1/2}\ \sin 2\psi\ \cos\beta_p$$

and:

p = polarization (v for vertical or h for horizontal).

T_{A_p} = measured antenna temperature for the given polarization.

Λ_p = a normalization constant.

T_{B_v}, T_{B_h} = vertical and horizontal radiation brightness temperature fields over all space.

g_{pv}, g_{ph} = the instrument antenna pattern fields over all space, co-polarized (g_{vv} and g_{hh}) and cross-polarized (g_{vh} and g_{hv}).

ψ = SMMR scan angle.

$\cos\beta_p$ = term describing the relative phase characteristics of the SMMR antenna ports. ($\cos\beta_p = 0$ implies perfect linear polarization.)

The above expression may be approximated by assuming that the antenna pattern function is identically zero for all values of θ and ϕ except those defining the direction of the line of sight. The resulting narrow beam approximation may be written as:

$$T_{A_p} = T_{B_v} G_{pv} + T_{B_h} G_{ph} \qquad \text{(Eq. 2)}$$

---

where:

$$G_{pv} = g_{pv}\ \cos^2\psi + g_{ph}\ \sin^2\psi + (g_{pv}g_{ph})^{1/2}\ \sin 2\psi\ \cos\beta_p$$

$$G_{ph} = g_{ph}\ \cos^2\psi + g_{pv}\ \sin^2\psi - (g_{pv}g_{ph})^{1/2}\ \sin 2\psi\ \cos\beta_p$$

and:

T_{B_v}, T_{B_h} = vertical and horizontal brightness temperatures in the direction of the instrument line of sight.

g_{pv}, g_{ph} = instrument antenna patterns integrated over all space and divided by Λ_p.

and, p, T_{A_p}, ψ, cos β_p are as defined above.

The corrections performed by the interim APC algorithm in converting input T_A data into T_B data are based on this narrow beam approximation. This same approximation is used in our estimation of the cos β terms. A least-squares technique has been used to determine what value of cos β agrees best with the observed antenna temperatures along the scan for each channel. In addition to assuming the narrow beam approximation, this solution method assumes a constant brightness temperature along the scan. The technique used to find antenna temperature data satisfying this criterion is discussed later.

The first step towards solving for the cos β terms of Equation 2 is the calculation of the brightness temperatures T_{B_v} and T_{B_h}. Equation 2 may be re-written in matrix form as:

$$\begin{pmatrix} T_{A_v} \\ T_{A_h} \end{pmatrix} = \begin{pmatrix} G_{vv} & G_{vh} \\ G_{hv} & G_{hh} \end{pmatrix} \begin{pmatrix} T_{B_v} \\ T_{B_h} \end{pmatrix} \qquad \text{(Eq. 3)}$$

Multiplying through by the matrix inverse gives:

$$\begin{pmatrix} T_{B_v} \\ T_{B_h} \end{pmatrix} = \frac{1}{G_{vv}G_{hh} - G_{hv}G_{vh}} \begin{pmatrix} G_{hh} & -G_{vh} \\ -G_{hv} & G_{vv} \end{pmatrix} \begin{pmatrix} T_{A_v} \\ T_{A_h} \end{pmatrix} \qquad \text{(Eq. 4)}$$

Using the assumption of a constant brightness temperature along the scan, we choose to solve for T_{B_v} and T_{B_h} at the center of scan ($\psi = 0$). Setting ψ equal to zero eliminates the unknown cos β term from the equations, and gives:

$$\begin{pmatrix} T_{B_v}^{\circ} \\ T_{B_h}^{\circ} \end{pmatrix} = \frac{1}{g_{vv}g_{hh} - g_{hv}g_{vh}} \begin{pmatrix} g_{hh} & -g_{vh} \\ -g_{hv} & g_{vv} \end{pmatrix} \begin{pmatrix} T_{A_v}^{\circ} \\ T_{A_h}^{\circ} \end{pmatrix} \qquad \text{(Eq. 5)}$$

Where the zero superscript indicates temperatures evaluated at zero scan position. Note that the assumption of constant brightness temperatures along the scan greatly simplifies the solution procedure. The alternative is to simultaneously estimate T_{B_v}, T_{B_h}, and cos β at each sample point along the SMMR scan.

Given values for T_{B_v} and T_{B_h}, we now find that cos β which satisfies a least-squares criterion in the sense of minimizing the function L:

$$L = \sum_{i=1}^{n} \left[T_{A_{p_i}} - \overline{f(\psi_i, \beta_p)} \right]^2 \qquad \text{(Eq. 6)}$$

where:

$$\overline{f(\psi_i, \beta_p)} = T_{B_v}^{\circ} G_{pv} + T_{B_h}^{\circ} G_{ph}$$

and:

n = the number of scan positions for the given channel

$T_{A_{p_i}}$ = the antenna temperature measured at the i^{th} scan position

$\overline{\psi_i}$ = the scan angle for the i^{th} scan position

and

$T_{B_v}^{\circ}, T_{B_h}^{\circ}$ are as defined in equation 5, and

G_{pv}, G_{ph} are as defined in equation 2.

The minimization of L is accomplished by setting the partial derivative of L with respect to cos β equal to zero, and solving the resultant equation.

$$\frac{\partial L}{\partial \cos \beta_p} = \sum_{i=1}^{n} -2 \left[T_{A_{p_i}} - f(\psi_i, \beta_p) \right] \frac{\partial f(\psi_i, \beta_p)}{\partial \cos \beta_p} = 0 \qquad \text{(Eq. 7)}$$

where:

$$\frac{\partial f(\psi_i, \beta_p)}{\partial \cos \beta_p} = T_{B_v}{}^{\circ} \frac{\partial G_{pv}}{\partial \cos \beta_p} + T_{B_h}{}^{\circ} \frac{\partial G_{ph}}{\partial \cos \beta_p} = -C \sin 2\psi_i \qquad \text{(Eq. 8)}$$

and:

$$C = \left[T_{B_h}{}^{\circ} - T_{B_v}{}^{\circ} \right] (g_{pv} g_{ph})^{1/2}$$

Expanding equation 7 and solving for cos β yields:

$$\frac{\partial L}{\partial \cos \beta_p} = \sum_{i=1}^{n} 2C \left[T_{A_{p_i}} - G_{pv} T_{B_v}{}^{\circ} - G_{ph} T_{B_h}{}^{\circ} \right] \sin 2\psi_i = 0 \qquad \text{(Eq. 9)}$$

$$\cos \beta_p = \frac{-A_2}{CA_1} \qquad \text{(Eq. 10)}$$

where:

$$A_1 = \sum_{i=1}^{n} \sin^2 (2\psi_i)$$

$$A_2 = \sum_{i=1}^{n} \left[T_{A_{p_i}} - T_{B_v}{}^{\circ} (g_{pv} \cos^2 \psi_i + g_{ph} \sin^2 \psi_i) - T_{B_h}{}^{\circ} (g_{ph} \cos^2 \psi_i + g_{pv} \sin^2 \psi_i \right] \sin 2\psi_i$$

and:

C is as defined in equation 8.

In order to achieve a data set which satisfies the criterion of a constant brightness temperature along the scan, the above solution (Eq. 10) is applied to antenna temperature data which has been averaged over many scans. That is, each $T_{A_{p_i}}$ of equation 10 is actually an average over many scans of those antenna temperatures observed for scan position i of each scan. This approach helps to cancel out any

environmentally-induced cross-track gradients in the data, and reduces environmental "noise" observed from scan to scan and from footprint to footprint. However, we have found that indiscriminate averaging of data in this fashion does not always remove environmentally-induced gradients. Our efforts to further reduce these gradients will be discussed later.

3.2.2 Results. A computer program has been developed which calculates cos β for each of the ten SMMR channels. The technique used is that described above. In addition to printed output, the program produces computer plots of the averaged T_A data versus scan angle and the fitted curves resulting from the calculated cosβ values.

Our best estimates of cosβ for each SMMR channel are given in Table 10, along with the RMS statistic for each curve fitted to the averaged T_A data. The RMS statistic is the square root of the minimum value of L (Eq. 6) divided by n (the number of scan positions for the given channel). Figures 10.1 through 10.5 contain plots of the averaged T_A data and the curves fitted to the data using the calculated cosβ terms.

The cosβ estimates contained in Table 10 are the results of fitting data consisting of 103 SMMR scans from three different orbits. The orbit segments used have been chosen especially for their uniform atmospheric conditions. As mentioned earlier, one of the assumptions used in calculating cos β is a constant brightness temperature along the SMMR scan. In principle, the averaging of large amounts of T_A data will cancel out all environmental variations across the swath. Unfortunately, we have found that the weather conditions in the GOASEX region are so varied that indiscriminate averaging of the data at hand does not sufficiently remove environmental effects. Therefore, we have changed our strategy from one of averaging all data to one of identifying short orbit segments which exhibit uniform conditions across the SMMR swath. The cross-track gradient software discussed previously has been executed for many different orbits for the purpose of identifying segments which are characterized by uniform atmospheric conditions (i.e., zero environmental cross-track gradients).

The result is that 103 scans from equatorial regions of three ascending orbits (1126, 1198, and 1255) have been selected as our "best" data set. Estimates of cos β have been produced for this data set (Table 10) as well as a number of other combinations of SMMR data. As expected, the RMS statistics around the fitted curves indicate that the curve fits achieved using the "best" data set are indeed better than those of other runs.

The cos β values calculated for the 6.6 and 10.7 GHz channels show little variation from run to run. In addition, E. Christensen and B. Wind, using a completely different estimation technique, have produced very similar cos β estimates for these four channels. Therefore, our confidence in the cos β estimates for the lower frequency channels is quite high.

The cos β values calculated for the 18, 21, and 37 GHz channels do show significant variation from run to run. This variation is undoubtedly due to the greater sensitivity of these channels to varying atmospheric water content. Therefore, our confidence in the estimates for these channels is not as high as for those of the lower frequency channels.

Several observations are made regarding the results shown in Table 10 and Figures 10.1 through 10.5:

(1) The averaged T_A data points generally fall along very smooth curves.

(2) The curve fits to the averaged T_A data all have RMS values below .4 degrees Kelvin except for the 6.6 and 21 GHz horizontal channels. The RMS values for these two channels are near .6 degrees Kelvin.

(3) The curve fits for the 6.6 and 21 GHz horizontal channels are not as good at the ends of the scan as they are in the center. This might be attributable to slight inaccuracies in the antenna gain coefficients (g_{hv} and g_{hh}) corresponding to these two channels.

3.2.3 Correlation Between cos β and Cross-track Gradients. In order to increase our confidence in the calculation of the cos β values, we have produced plots of the total cross-track variations observed in the T_B data versus the cos β values calculated from the T_A data. The plotted T_B gradient values are averages of the gradients observed over the latitude range used in calculating cos β.

An example of this type of plot which corresponds to the cos β values calculated for the "best" data set is given in Figure 11.1. The cross-track variations plotted here are those observed in the interim APC output corresponding to this same "best" data set. The ten plotted points represent the T_B gradient - cos β pairs for the ten SMMR channels. The line shown in this plot represents the first-order least-squares curve fit to the data points. It is encouraging to note that the plotted points are fitted quite well by this line, and that the line passes close to the origin (i.e., a zero cos β corresponds to a zero cross-track gradient). The RMS statistic about the fitted line is .88 degrees Kelvin.

Figure 11.2 and 11.3 contain similar plots for a data set comprising a portion of orbit 1255. The T_B cross-track variations plotted in Figure 11.2 are calculated from interim APC brightness temperature data, while those plotted in Figure 11.3 are from the corresponding final APC data. Note that the cos β values correlate quite well with the interim T_B cross-track variations, but hardly at all with the final T_B gradients. We conclude from this that the cross-track gradients present in the interim T_B data may be modeled as a cos β coupling in the antenna temperature data. However, it appears that the sidelobe corrections are introducing additional effects which are masking this relationship in the final T_B data.

4.0 CONCLUSIONS

Several conclusions may be drawn from the results discussed in the previous section 3.0:

(1) There appears to exist a bias between the brightness temperatures produced by the final and interim APC algorithms. This bias is different for each SMMR channel and varies both with scan position and the mean brightness temperature level being observed.

As shown in Table 1, the brightness temperatures produced by the final APC are often significantly lower than corresponding values produced by the interim APC. This is especially true for the 18, 21, and 37 GHz channels. However, as the brightness temperature level rises, the differences between final and interim values diminish, with the final brightness temperatures sometimes rising above the interim values (e.g., the region near 45° latitude of figures 5.1 through 5.10).

As can be seen from the middle portion of Table 1, the differences between the two algorithms vary across the scan. The fact that the final brightness temperature values are often lower on the edges of the swath than in the center suggests that the sidelobe corrections being applied to the cells near the swath's edge may be too large. The sidelobe corrections for all cells involve brightness temperatures derived from a world brightness temperature map. But, the map-derived temperatures have a larger effect on the cells nearer the edge of the swath than on those in the center. Therefore, it appears that the map-derived temperatures may be too high. This could account for the overall lowering of the final brightness temperatures with respect to the interim values. It could also account for the final brightness temperatures being lower on the edges than in the center of the swath.

(2) The final brightness temperature values exhibit anomalous behavior at land-sea interfaces in that the values tend to "ring" when crossing such a transition boundary. The values undershoot the ambient temperature level on the ocean side of the interface, and overshoot the ambient level on the land side. Section 3.1.2 contains a more detailed discussion of this phenomenon. This "ringing" effect may indicate that the near sidelobe correction coefficients need further "fine-tuning."

(3) As discussed in Section 3.1.3, the final APC algorithm appears to diminish sidelobe effects caused by land masses adjacent to the SMMR swath. However, as expected, the cells immediately adjacent to land still contain sidelobe contamination.

(4) As discussed in section 3.1.4, the vertical channels appear to be biased low, whereas the horizontal channels appear to be biased high with respect to model-predicted values. This is true of both the final and interim APC brightness temperatures. If corrections were applied to these observed biases to account for unmodeled cloud and wind-speed effects, the positive biases

observed for the horizontal channels would be decreased. However, at the same time, the negative biases observed for the vertical channels would become still more negative. Therefore, it appears that the vertical SMMR channels, particularly 18, 21, and 37 GHz, are probably biased low, though it is not possible at this time to accurately quantify these biases.

(5) As discussed in section 3.2.3, it appears that the cross-track gradients present in the interim T_B data may be modeled as a cos β coupling in the antenna temperature data. However, it appears that the sidelobe corrections are introducing additional effects which are masking this relationship in the final T_B data. Our best estimates of cos β for each SMMR channel are given in Table 10, along with the RMS statistic for each curve fitted to the averaged antenna temperature data. Due to the greater sensitivity of the 18, 21, and 37 GHz channels to varying atmospheric water content, our confidence in the cos β estimates for these channels is not as high as for those of the lower frequency channels.

(6) The cos β curve fits for the 6.6 and 21 GHz horizontal channels are not as good at the ends of the scan as they are in the center. This might be attributable to slight inaccuracies in the antenna gain coefficients (g_{hv} and g_{hh}) corresponding to these two channels.

5.0 RECOMMENDATIONS

As mentioned in the introduction, further evaluation of the final APC algorithm will be performed as the algorithm matures. At this time, the only specific recommendation which can be made is that the cos β correction be implemented to reduce the observed T_B cross-track gradients. If this correction is not adequate for the higher frequency channels, then a more rigorous estimation of the cos β terms should be performed.

6.0 NEW TECHNOLOGY

No new technology has been developed in the course of this study.

7.0 REFERENCES

1. Kitzis, S.N. and Kitzis, J.L., "Evaluation and Analysis of SEASAT-A SMMR APC Algorithm: 6.6 GHz T_B vs. $T_{surface\ truth}$ Comparison Results," March 16, 1979.

2. Kitzis, S.N. and Kitzis, J.L., "Evaluation and Analysis of SEASAT-A SMMR APC Algorithm: T_B Measured vs T_B Calculated Comparison Results," April 13, 1979.

3. Peixoto, J.P. and Crisi, A.R., "Hemispheric Humidity Conditions During the IGY," AFCRL-65-794, November 1, 1965.

4. Njoku, E.G., "Antenna Pattern Correction Procedures for the SMMR," JPL Publication.

Table 1. Differences Between Final and Interim APC Data, Orbit 1255, 20°S to 5°N

A. Interim APC minus Final APC without Sidelobe Corrections

Channel	Left	Near Center	Right
6.6 V	3.25	3.25	3.25
6.6 H	.25	.00	.00
10.7 V	1.75	1.50	1.75
10.7 H	-1.50	-1.50	-1.50
18 V	1.25	1.25	1.25
18 H	- .50	- .50	- .50
21 V	.25	.25	.25
21 H	- .75	- .75	- .75
37 V	.00	.25	.00
37 H	.00	.00	.00

B. Interim APC minus Final APC with Sidelobe Corrections

Channel	Left	Near Center	Right
6.6 V	3.75	3.75	6.75
6.6 H	.25	.00	.75
10.7 V	5.50	2.50	7.50
10.7 H	.00	1.25	-1.25
18 V	11	5	7
18 H	4	3	7
21 V	7	3	8
21 H	6	6	7
37 V	11	3	9
37 H	11	5	8

C. Final APC without Sidelobe Corrections minus Final APC with Sidelobe Corrections

Channel	Left	Near Center	Right
6.6 V	.50	.50	3.50
6.6 H	.00	.00	.75
10.7 V	3.75	1.00	5.75
10.7 H	1.50	2.75	.25
18 V	10	4	6
18 H	5	4	8
21 V	7	3	8
21 H	7	7	8
37 V	11	3	9
37 H	11	5	8

Notes:

1. Data for each channel is taken from its best grid.
2. All differences are in degrees Kelvin.

Table 1. Diferences Between Final and Interim APC Data, Orbit 1255, 20°S to 5°N (Contd)

Notes: (Contd)

3. "Left" indicates data from the extreme left cells of all grids (columns 1, 1, 1, 1 of grids 1, 2, 3, 4 respectively).

4. "Right" indicates data from the extreme right cells of all grids (columns 4, 7, 11, 22).

5. "Near center" indicates data from columns 3, 5, 7, 14 of grids 1, 2, 3, 4 respectively.

6. Integer entries were measured to a resolution of 1°K. Accuracy (3σ) is estimated to be 3°K.

7. Other entries were measured to a resolution of 0.25°K. Accuracy (3σ) is estimated to be 1°K.

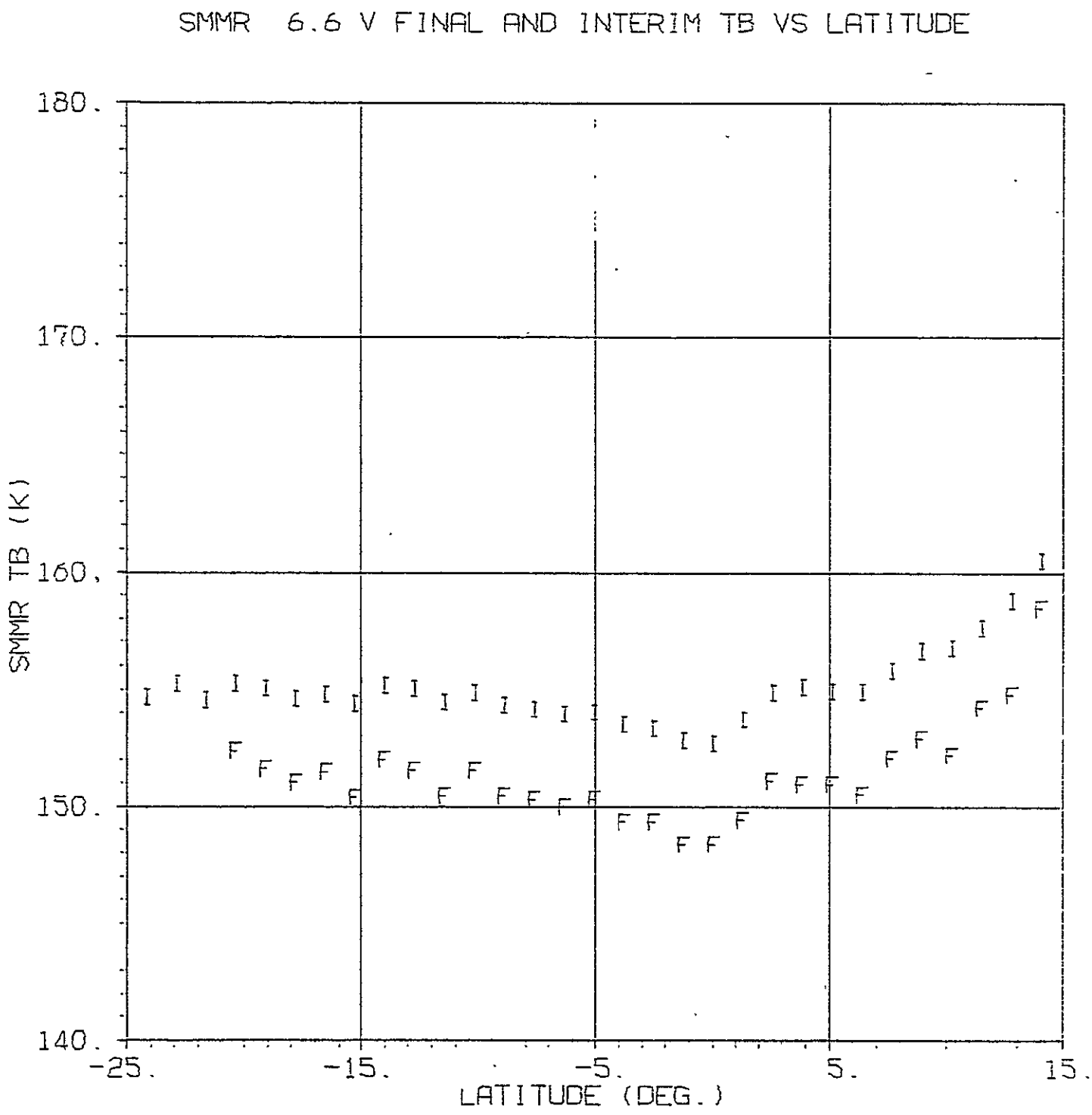

Figure 1.1. Orbit 1255, Grid 1, Column 1

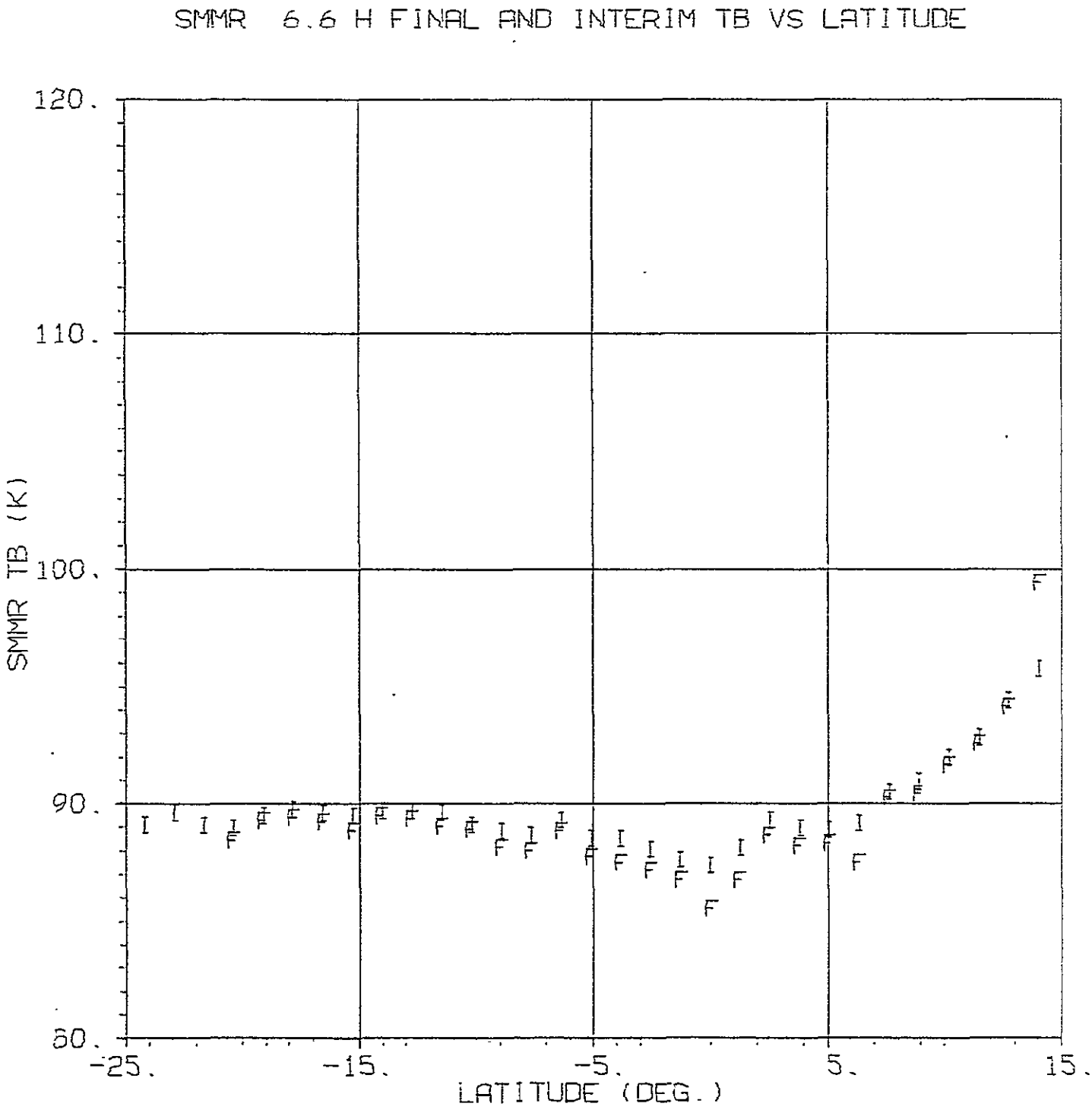

Figure 1.2. Orbit 1255, Grid 1, Column 1

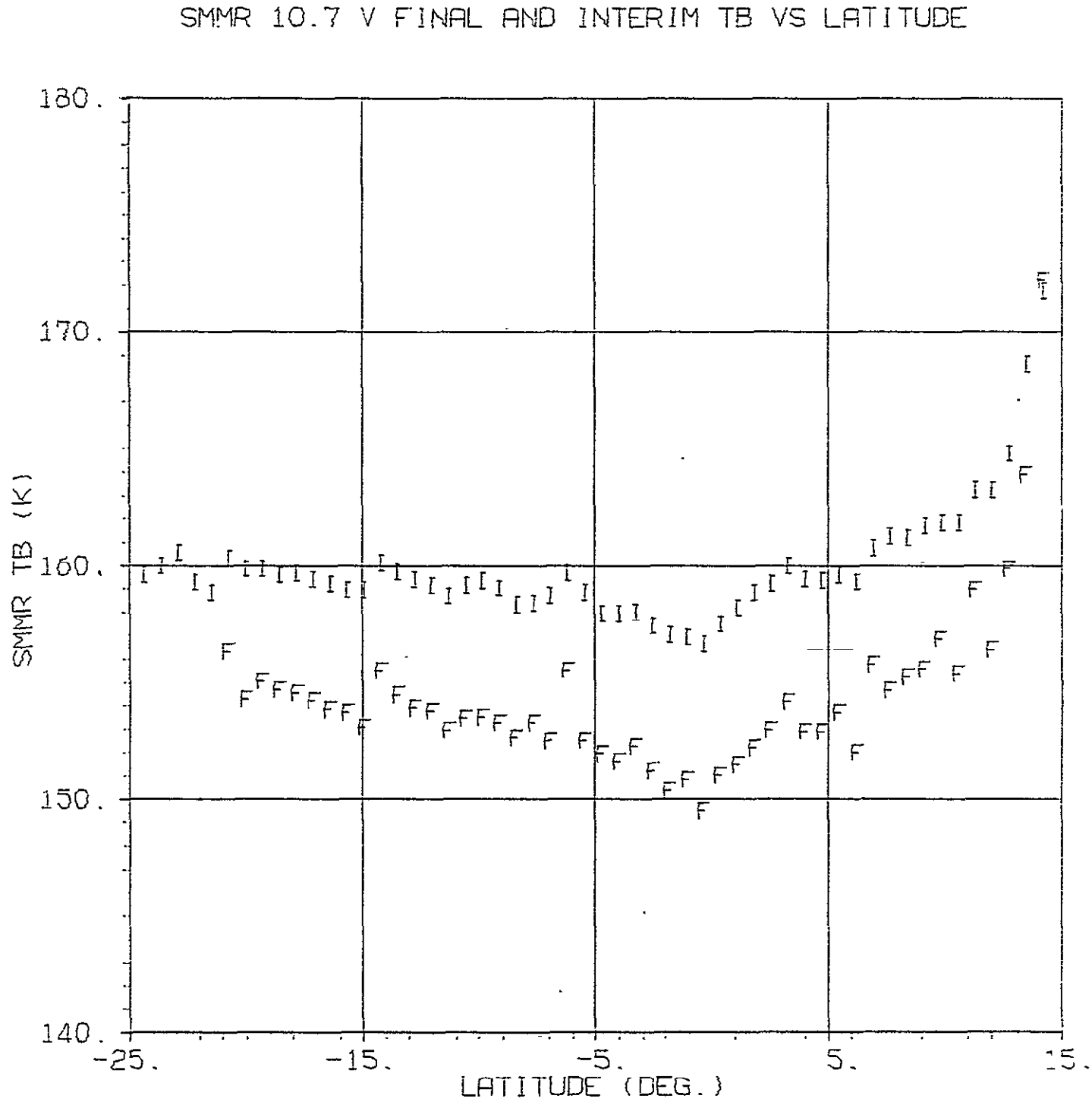

Figure 1.3. Orbit 1255, Grid 2, Column 1

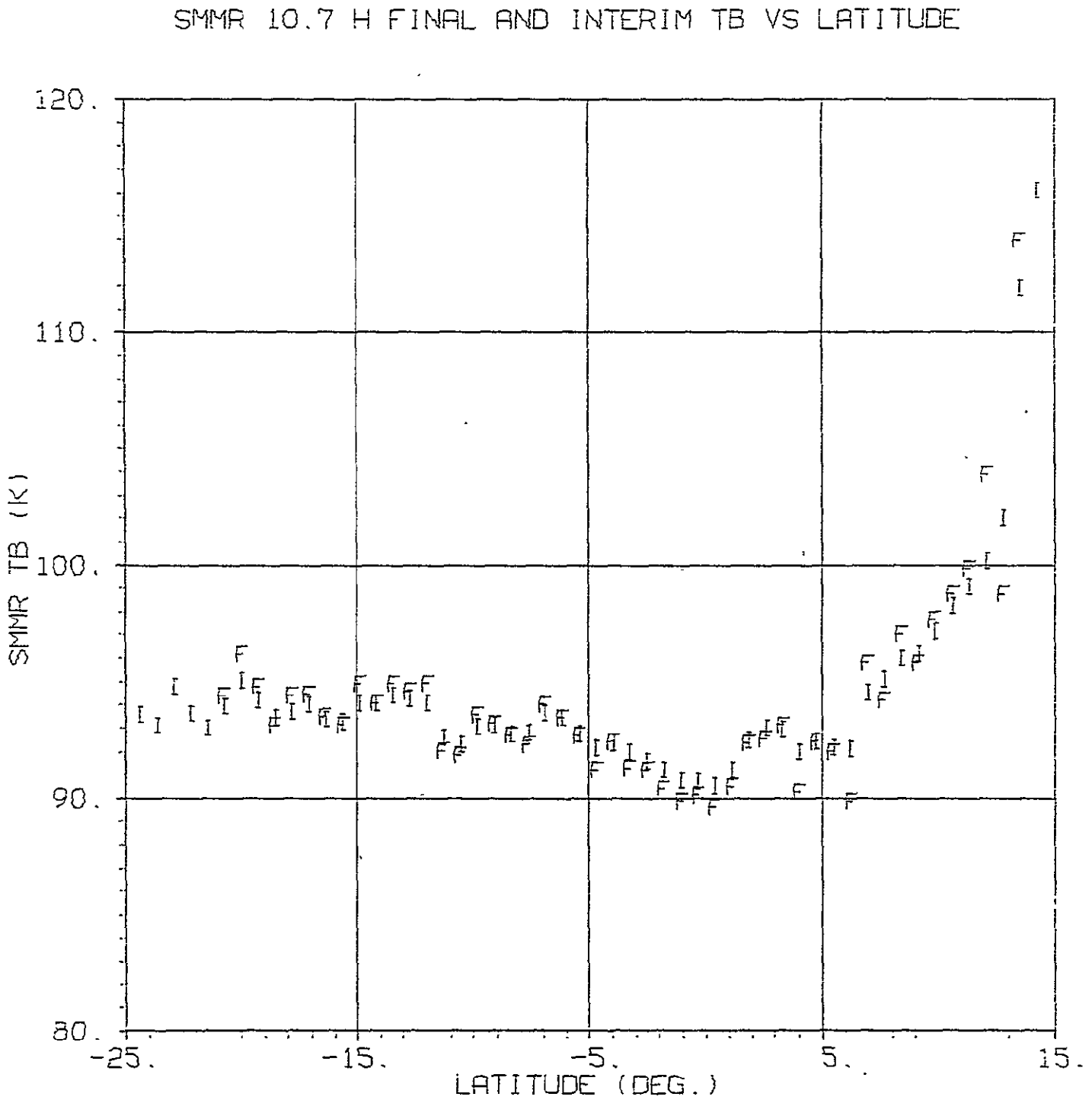

Figure 1.4. Orbit 1255, Grid 2, Column 1

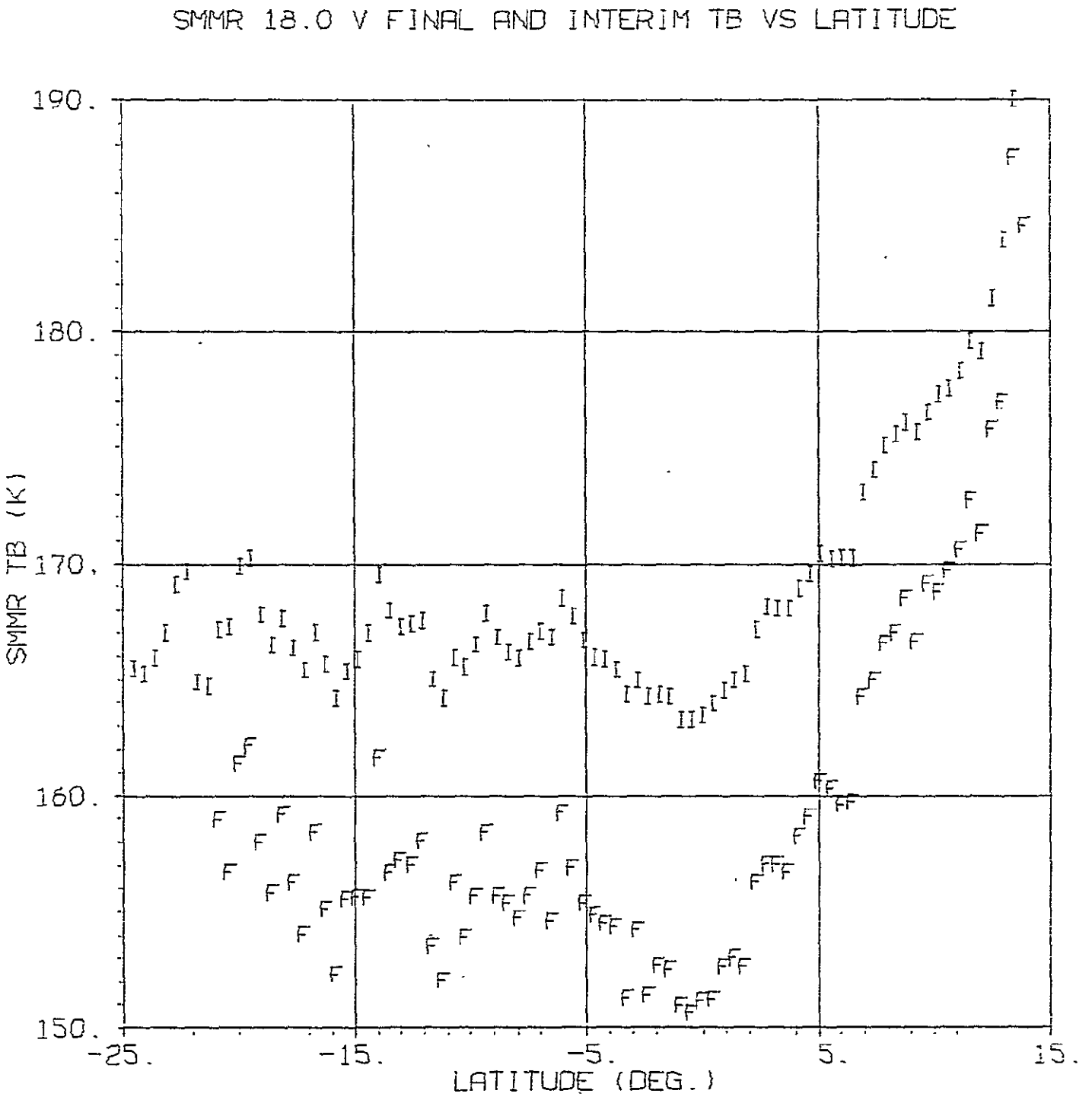

Figure 1.5. Orbit 1255, Grid 3, Column 1

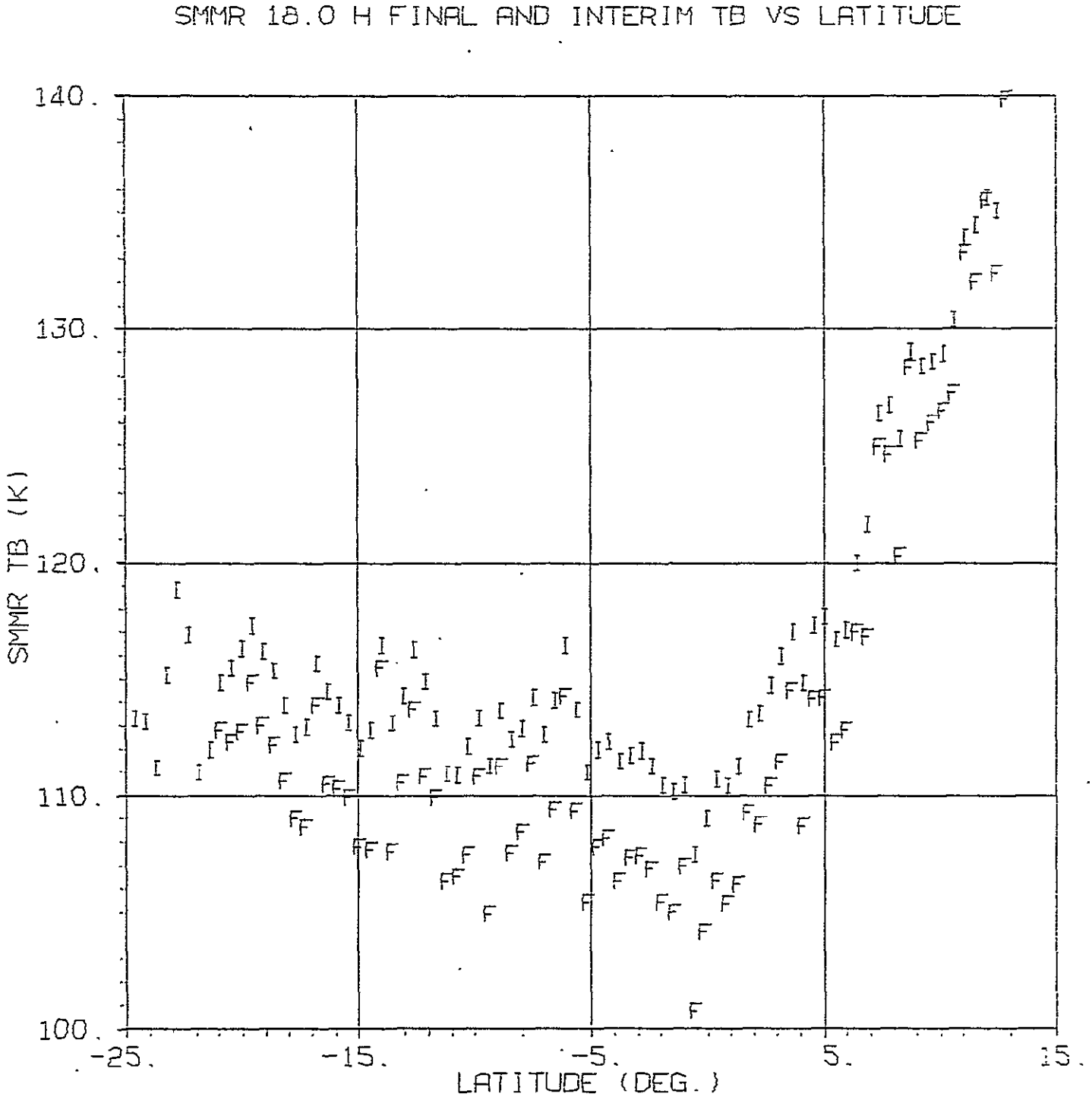

Figure 1.6. Orbit 1255, Grid 3, Column 1

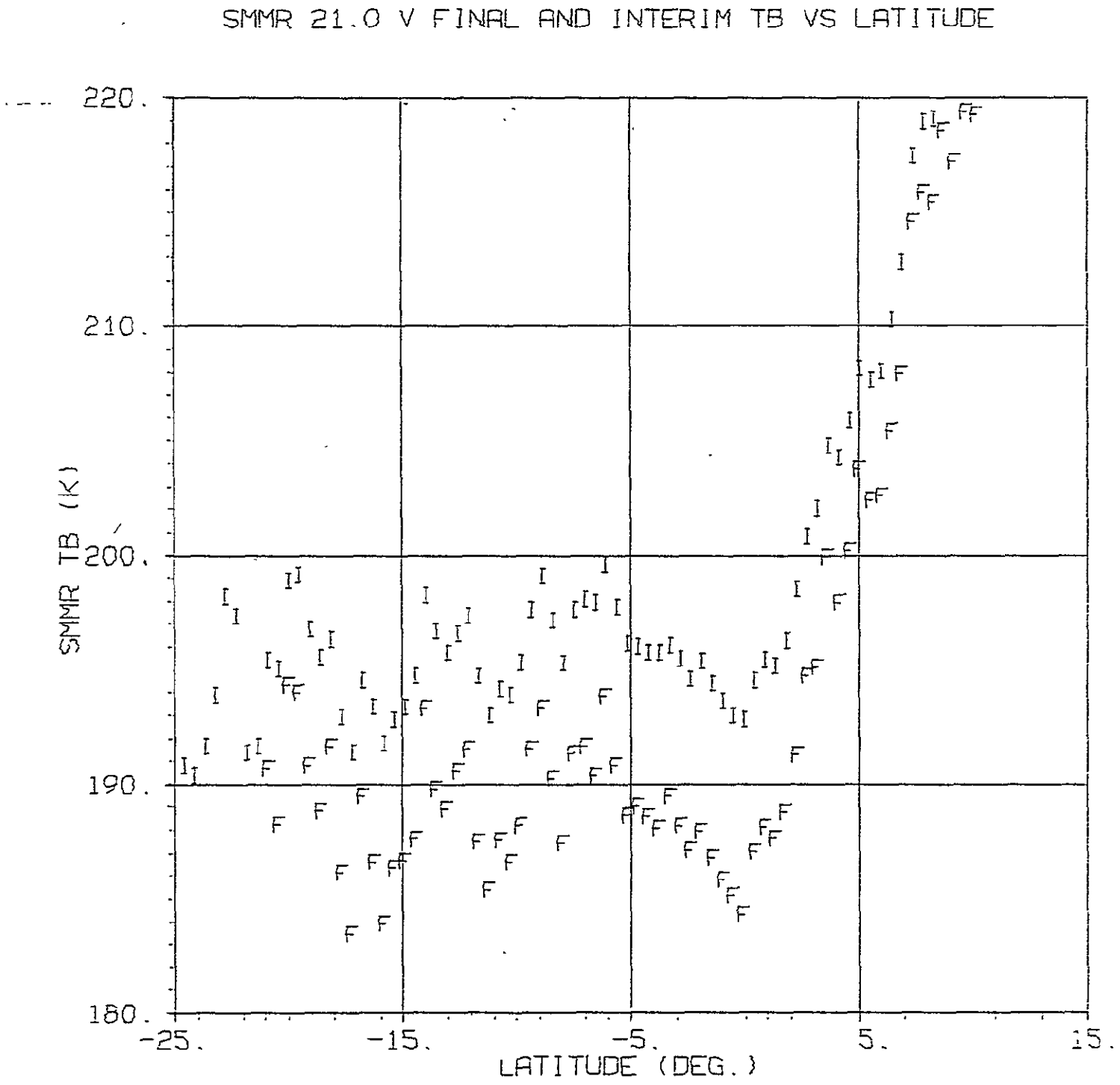

Figure 1.7. Orbit 1255, Grid 3, Column 1

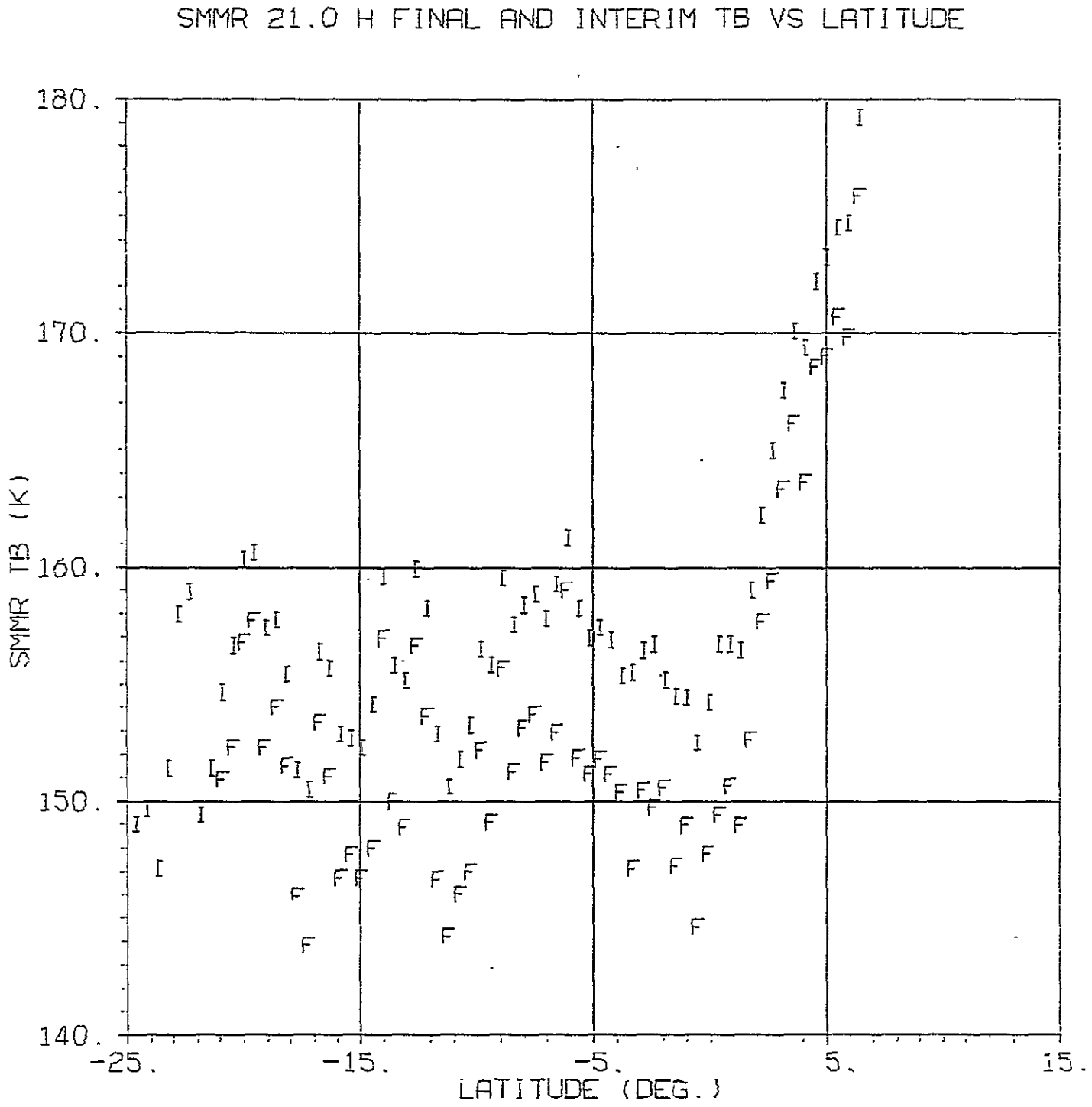

Figure 1.8. Orbit 1255, Grid 3, Column 1

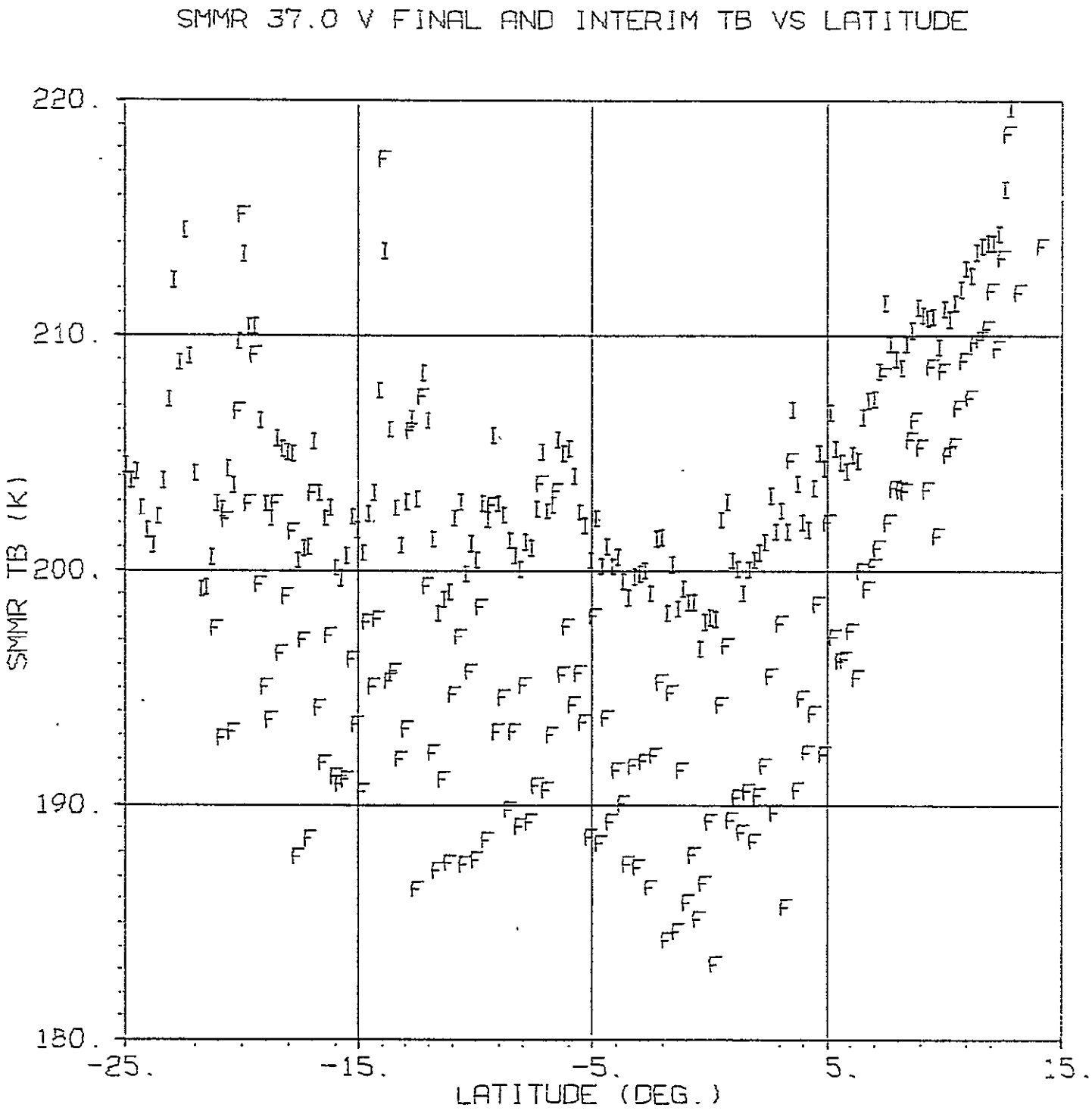

Figure 1.9. Orbit 1255, Grid 4, Column 1

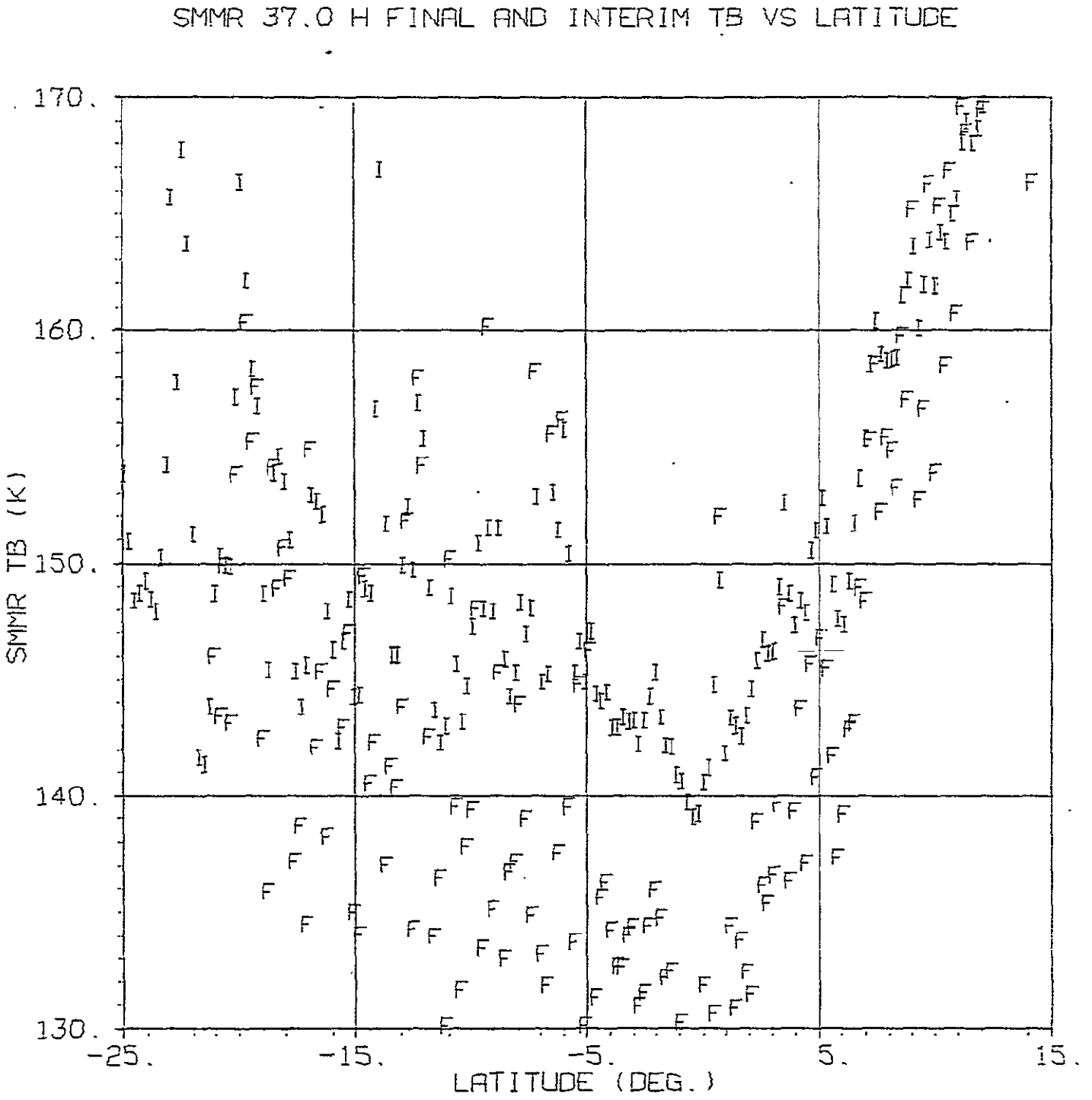

Figure 1.10. Orbit 1255, Grid 4, Column 1

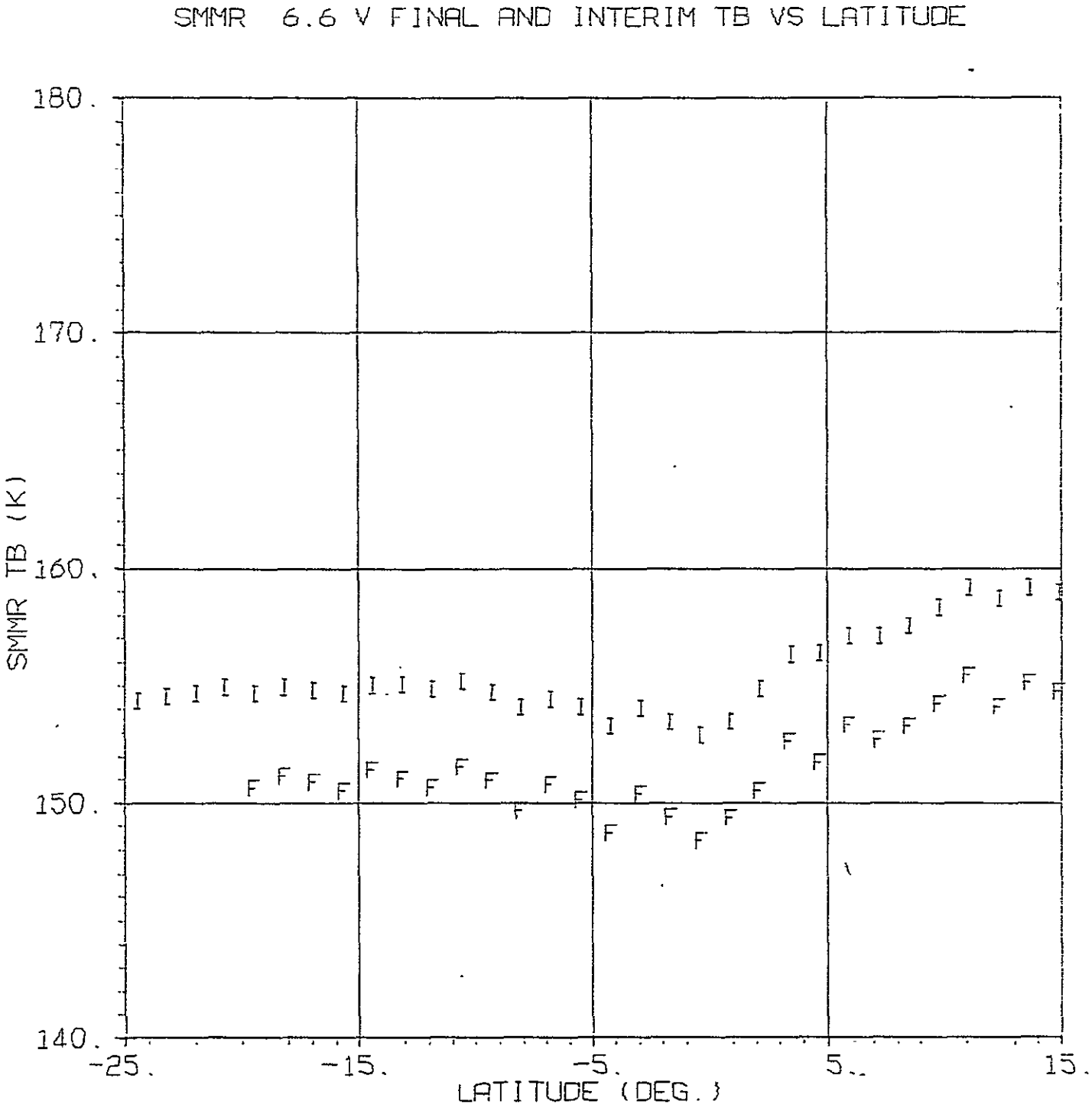

Figure 2.1. Orbit 1255, Grid 1, Column 3

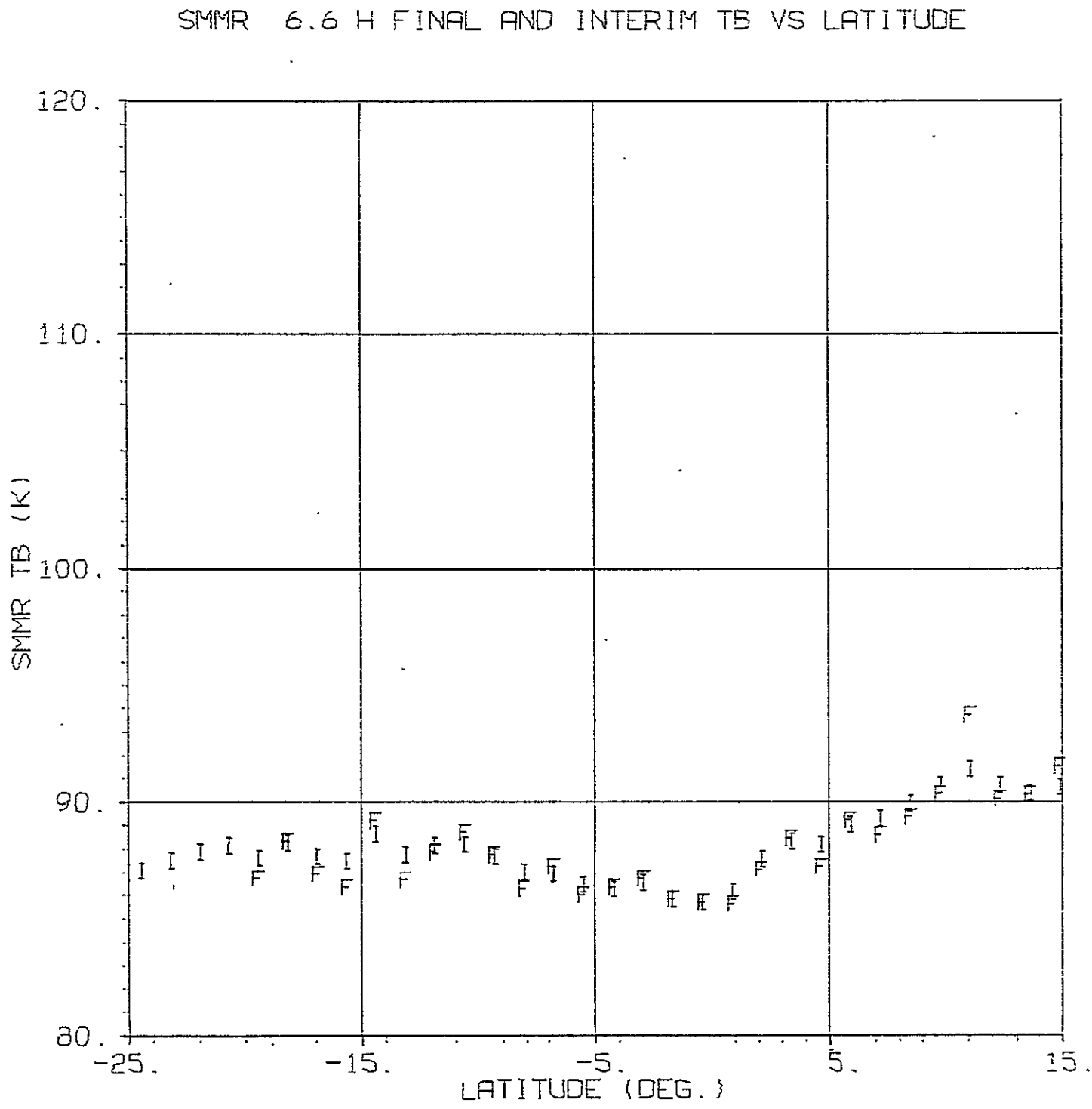

Figure 2.2. Orbit 1255, Grid 1, Column 3

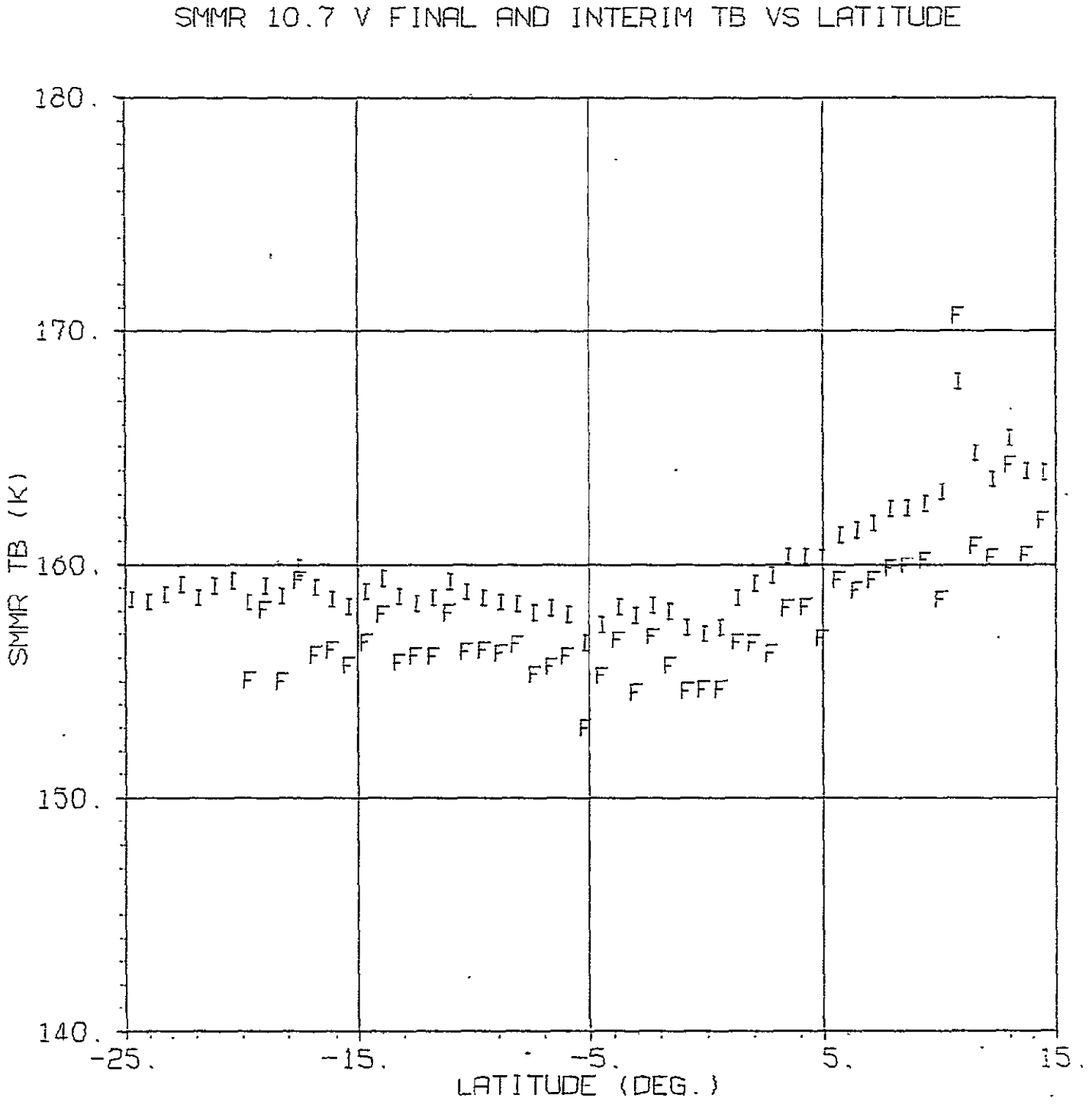

Figure 2.3. Orbit 1255, Grid 2, Column 5

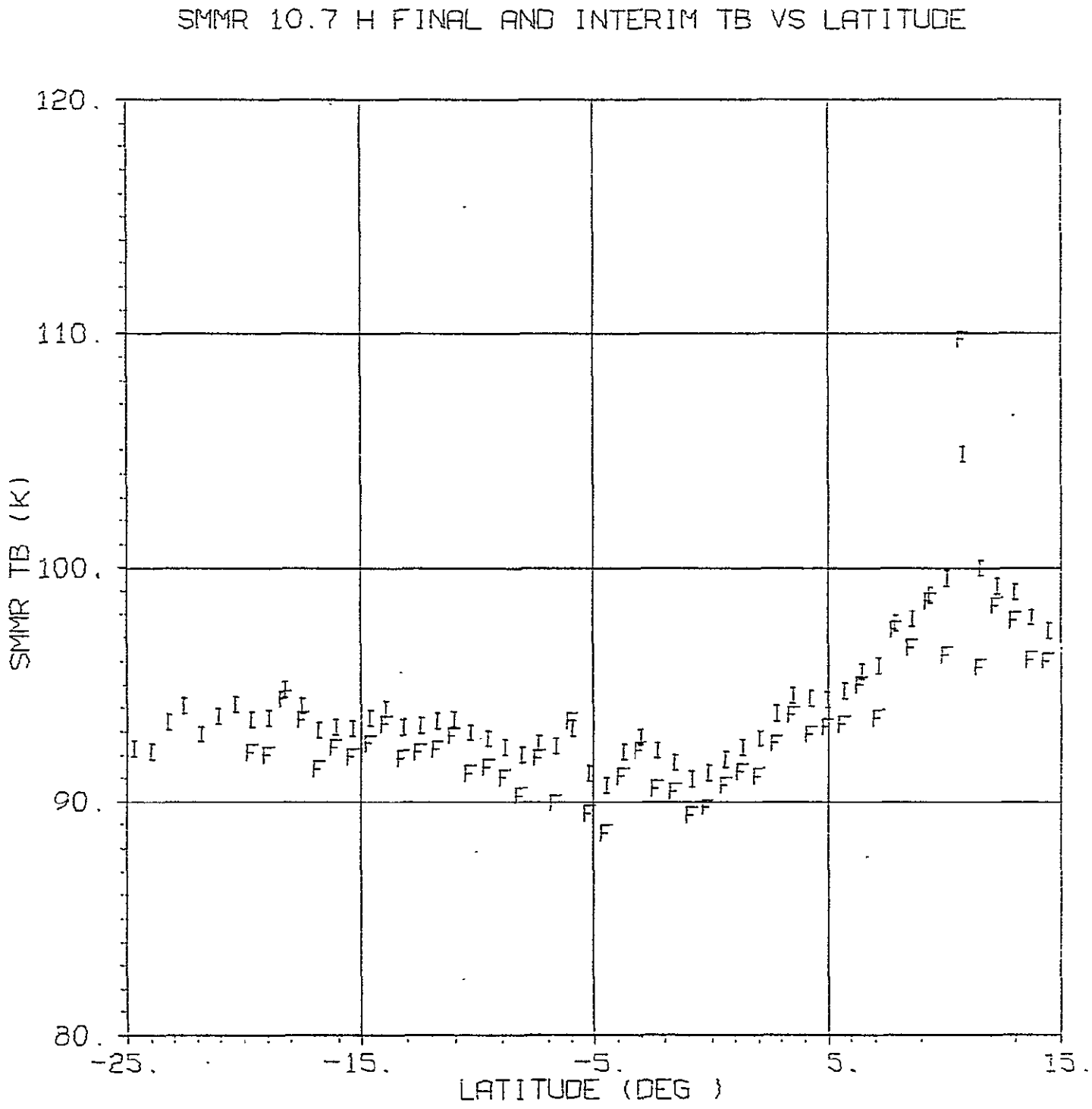

Figure 2.4. Orbit 1255, Grid 2, Column 5

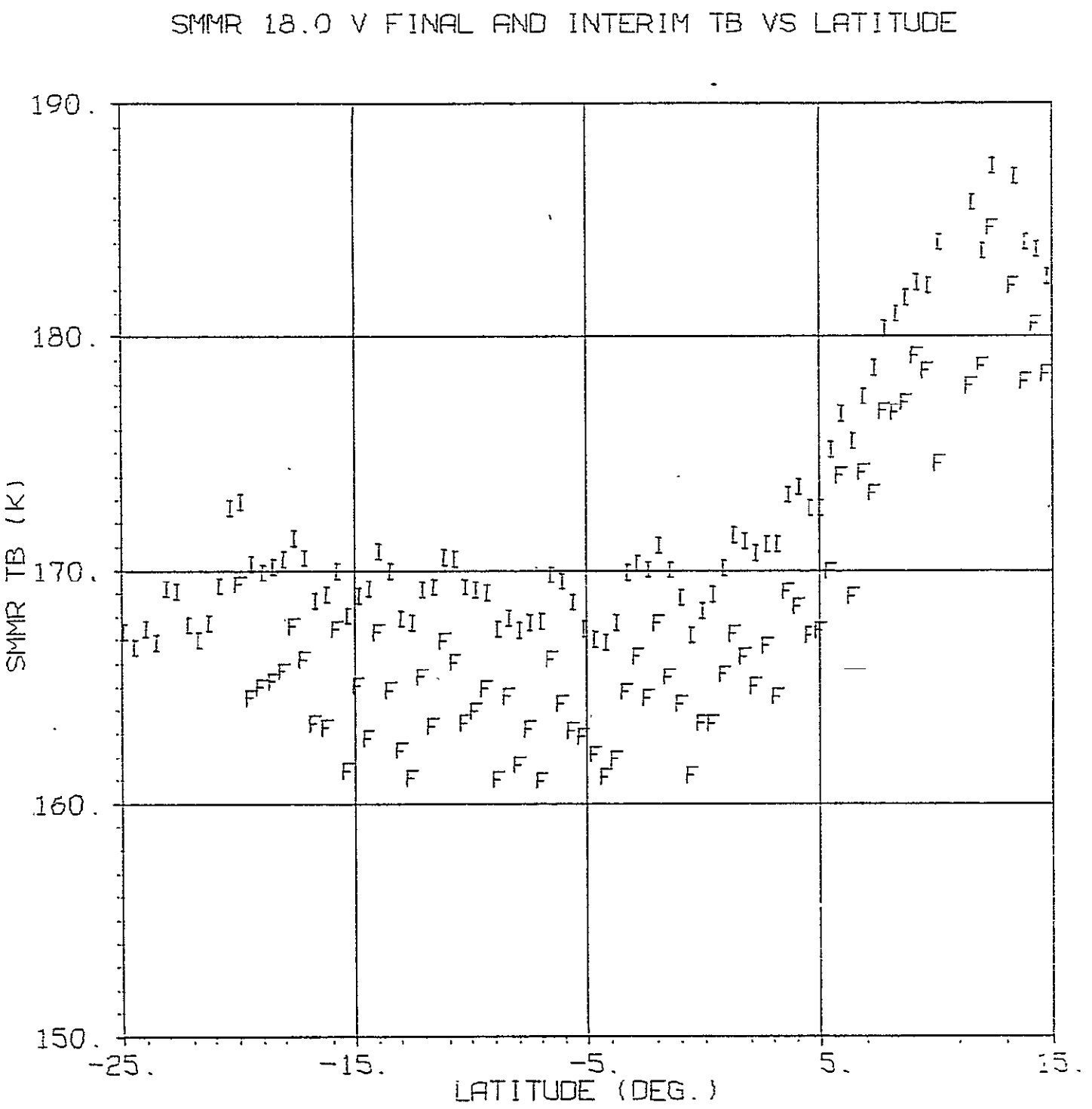

Figure 2.5. Orbit 1255, Grid 3, Column 7

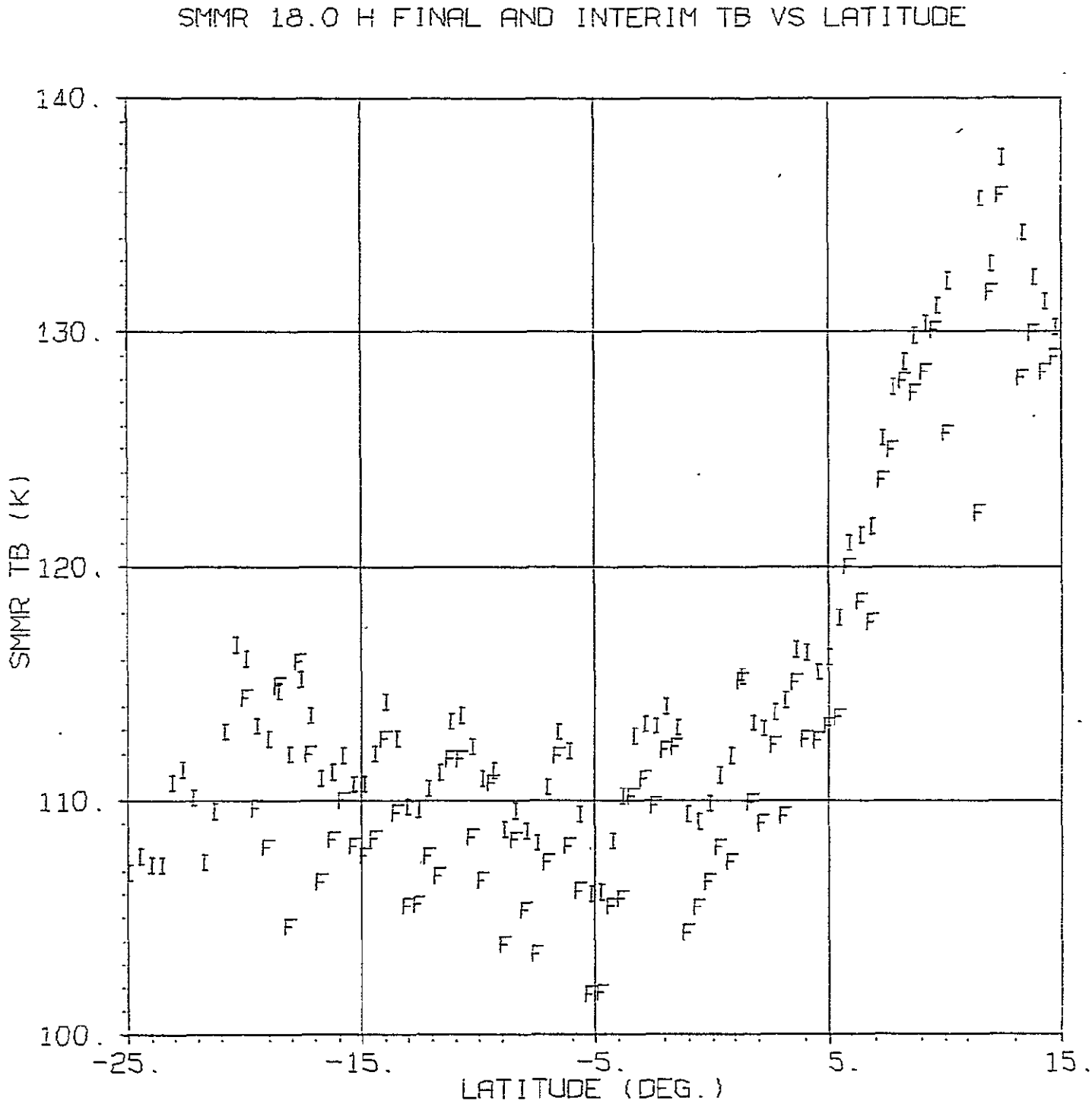

Figure 2.6. Orbit 1255, Grid 3, Column 7

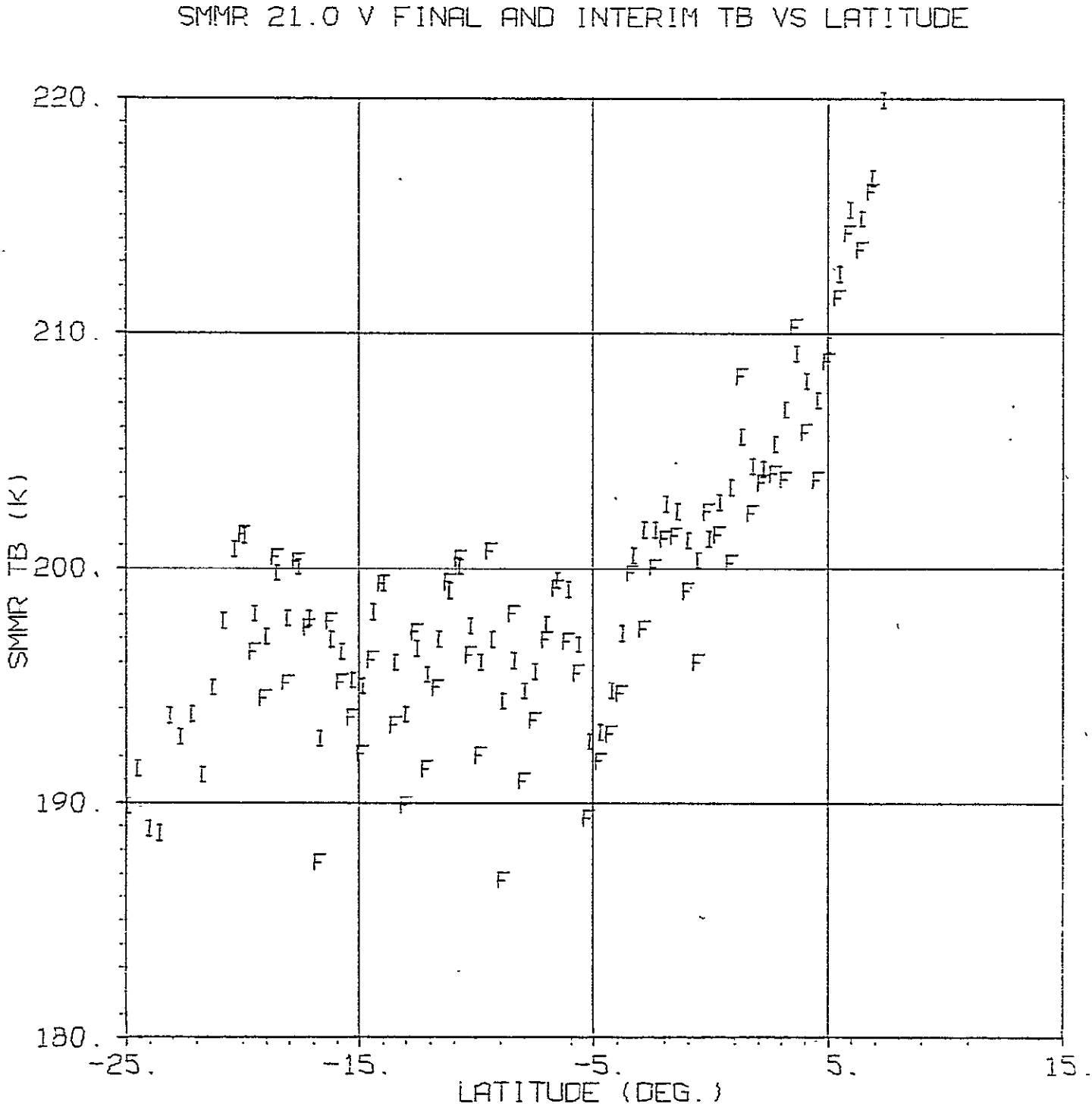

Figure 2.7. Orbit 1255, Grid 3, Column 7

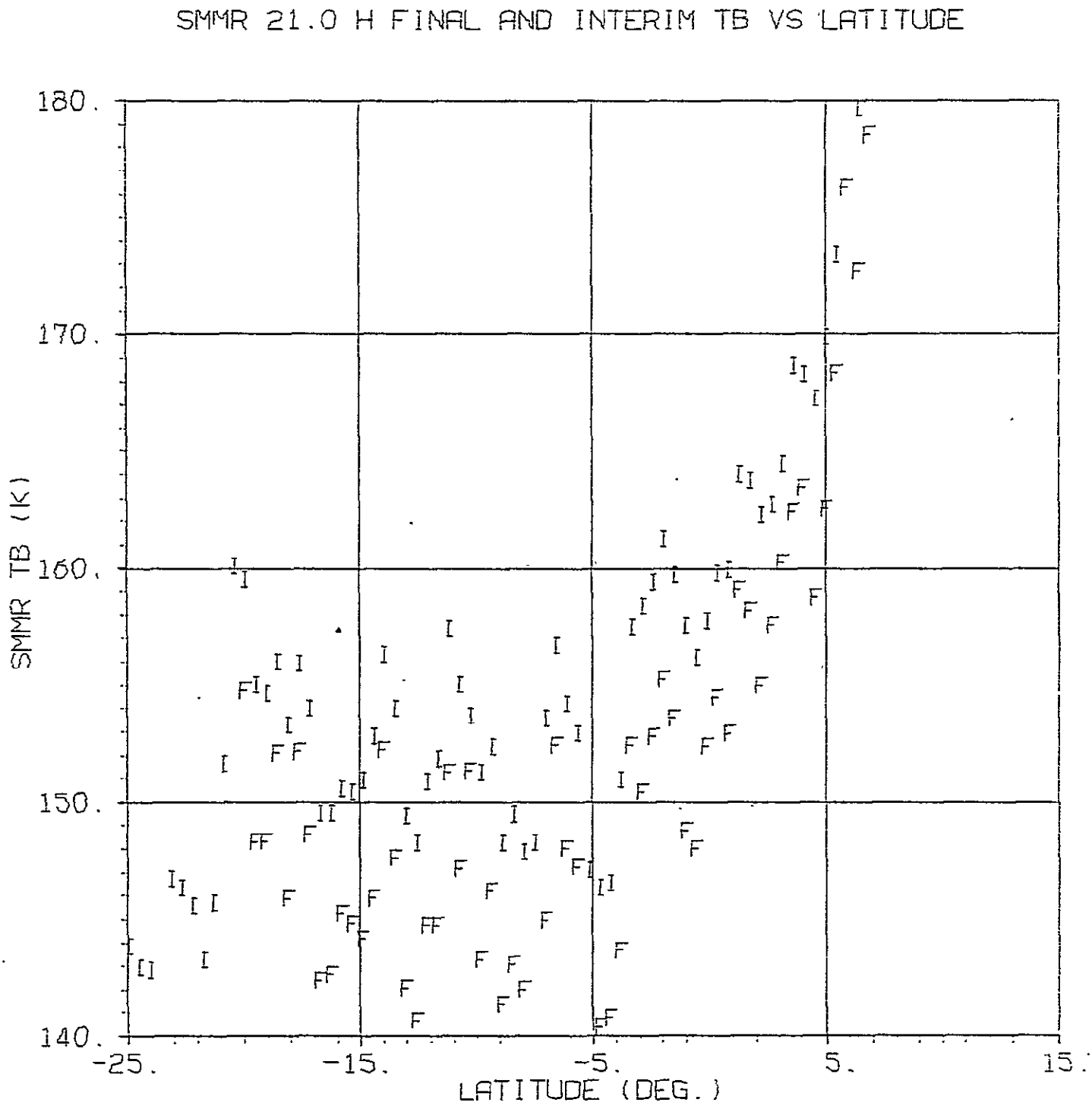

Figure 2.8. Orbit 1255, Grid 3, Column 7

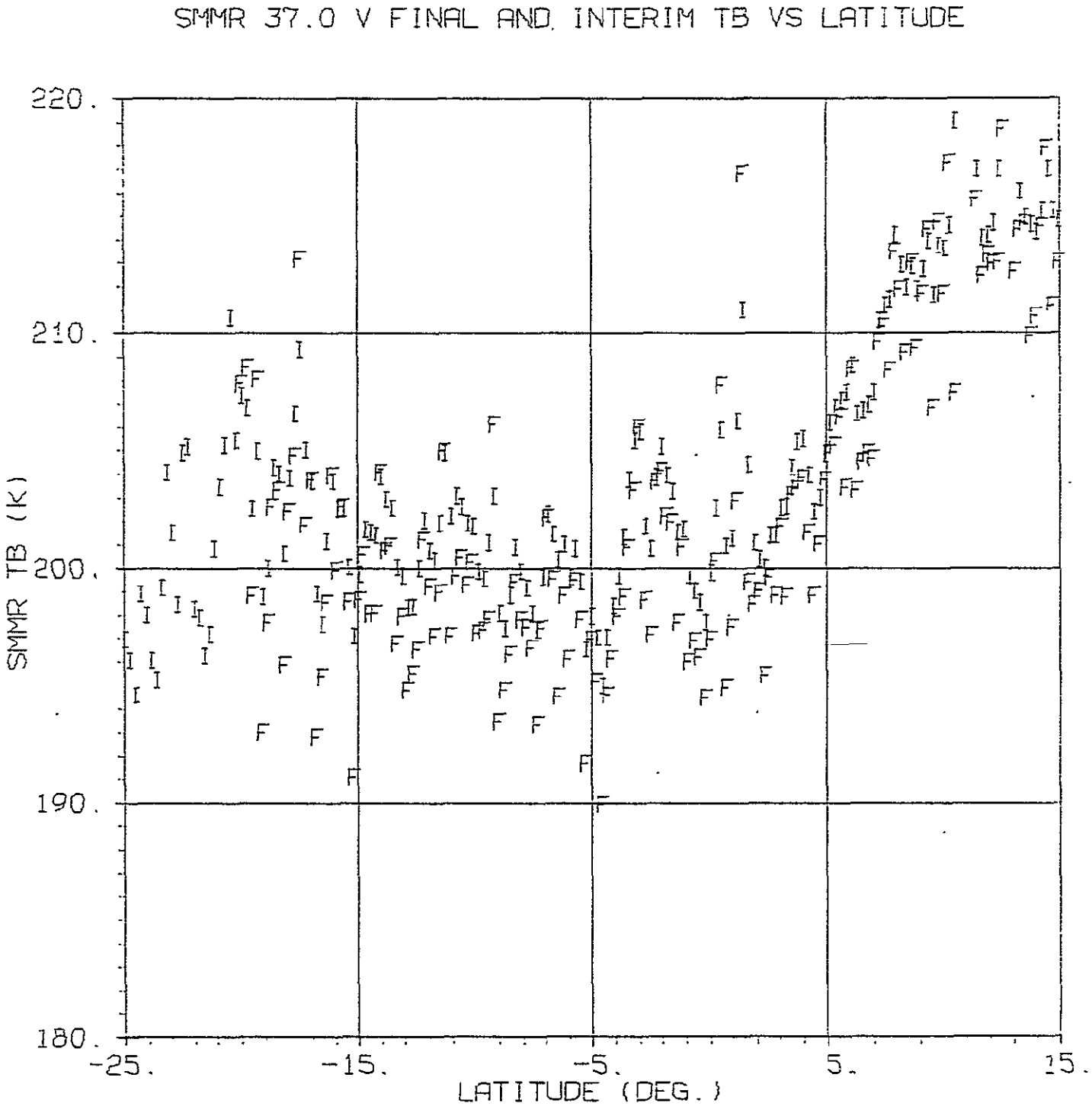

Figure 2.9. Orbit 1255, Grid 4, Column 14

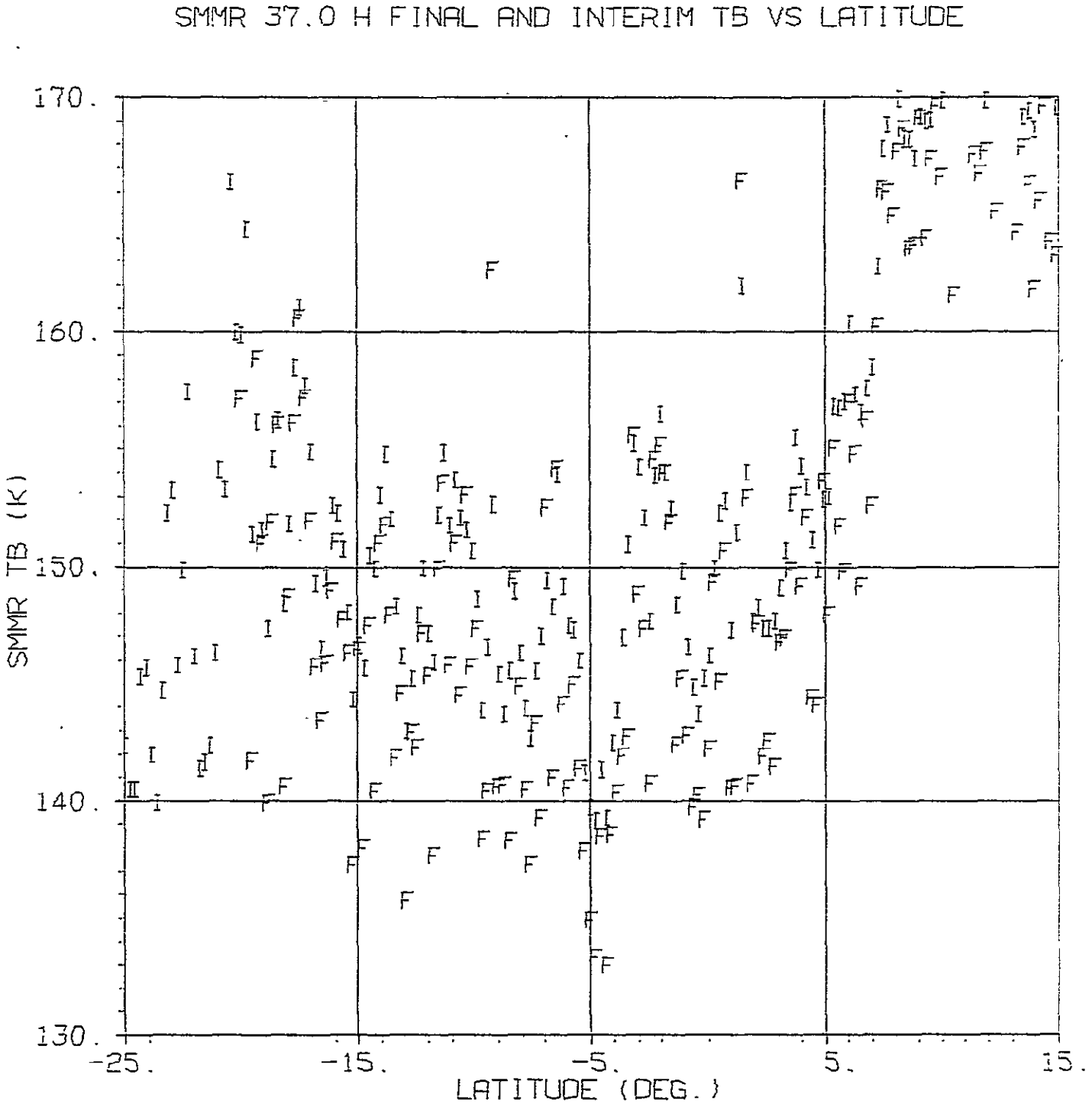

Figure 2.10. Orbit 1255, Grid 4, Column 14

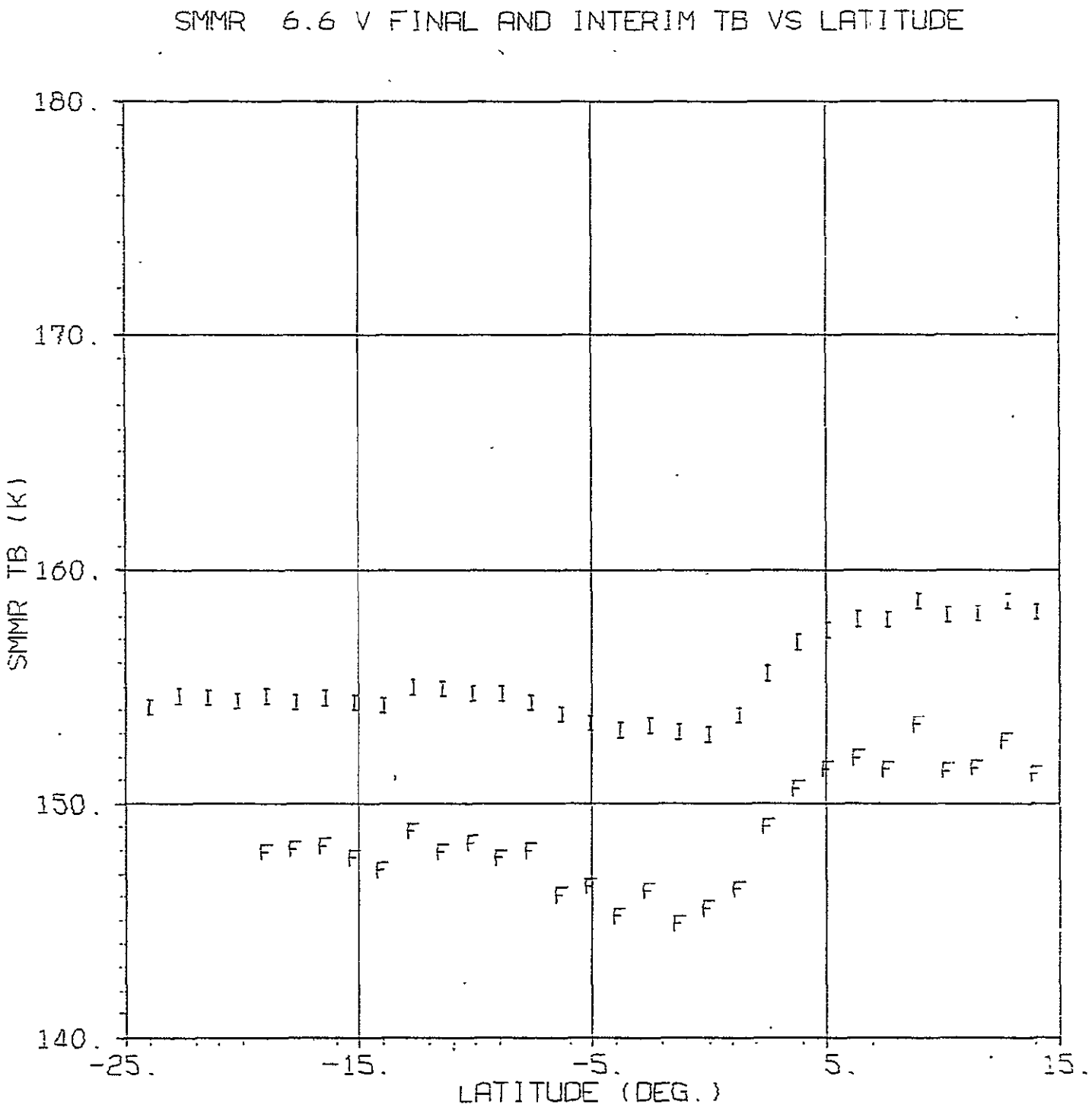

Figure 3.1. Orbit 1255 Grid 1, Column 4

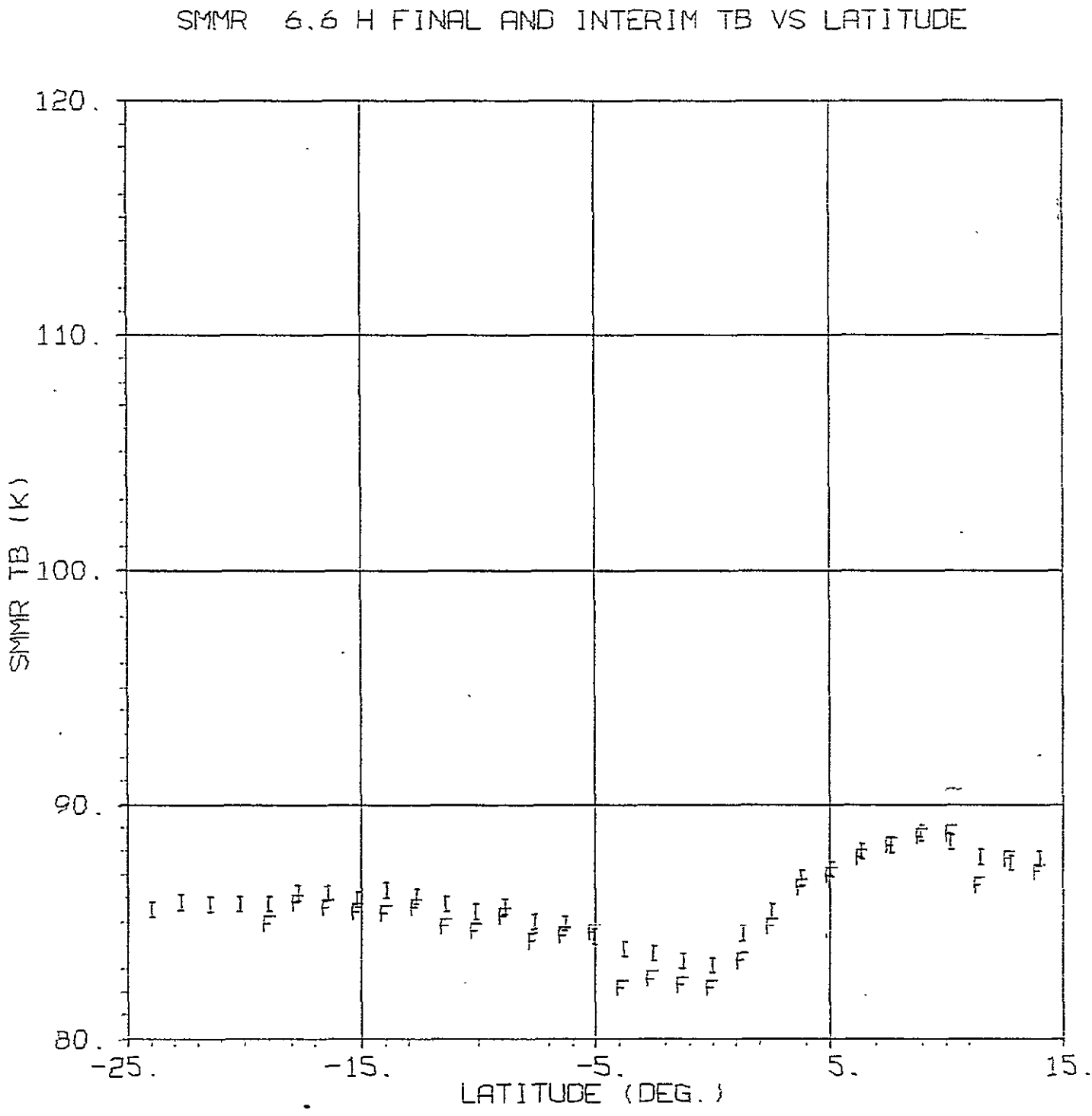

Figure 3.2. Orbit 1255, Grid 1, Column 4

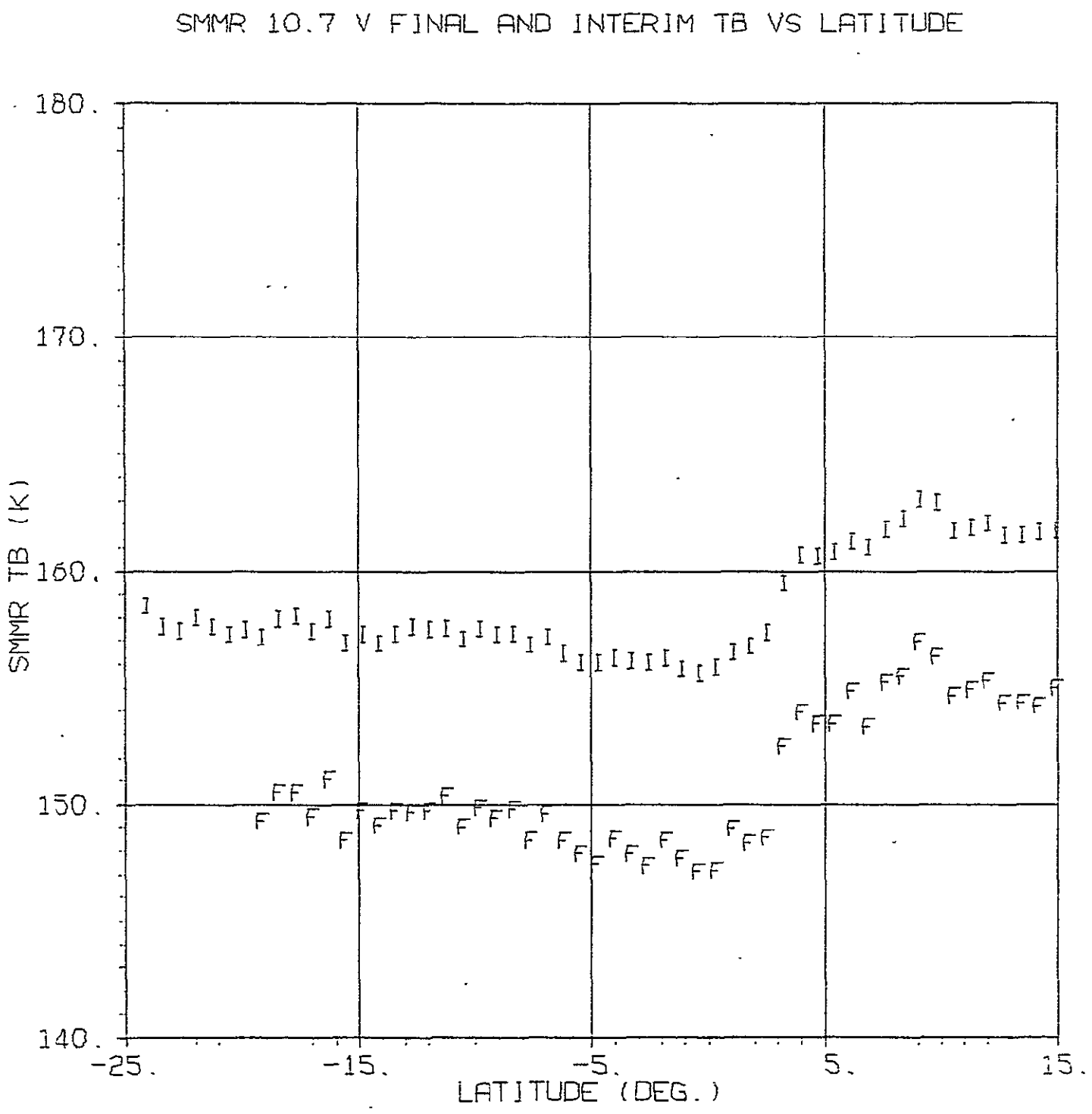

Figure 3.3. Orbit 1255, Grid 2, Column 7

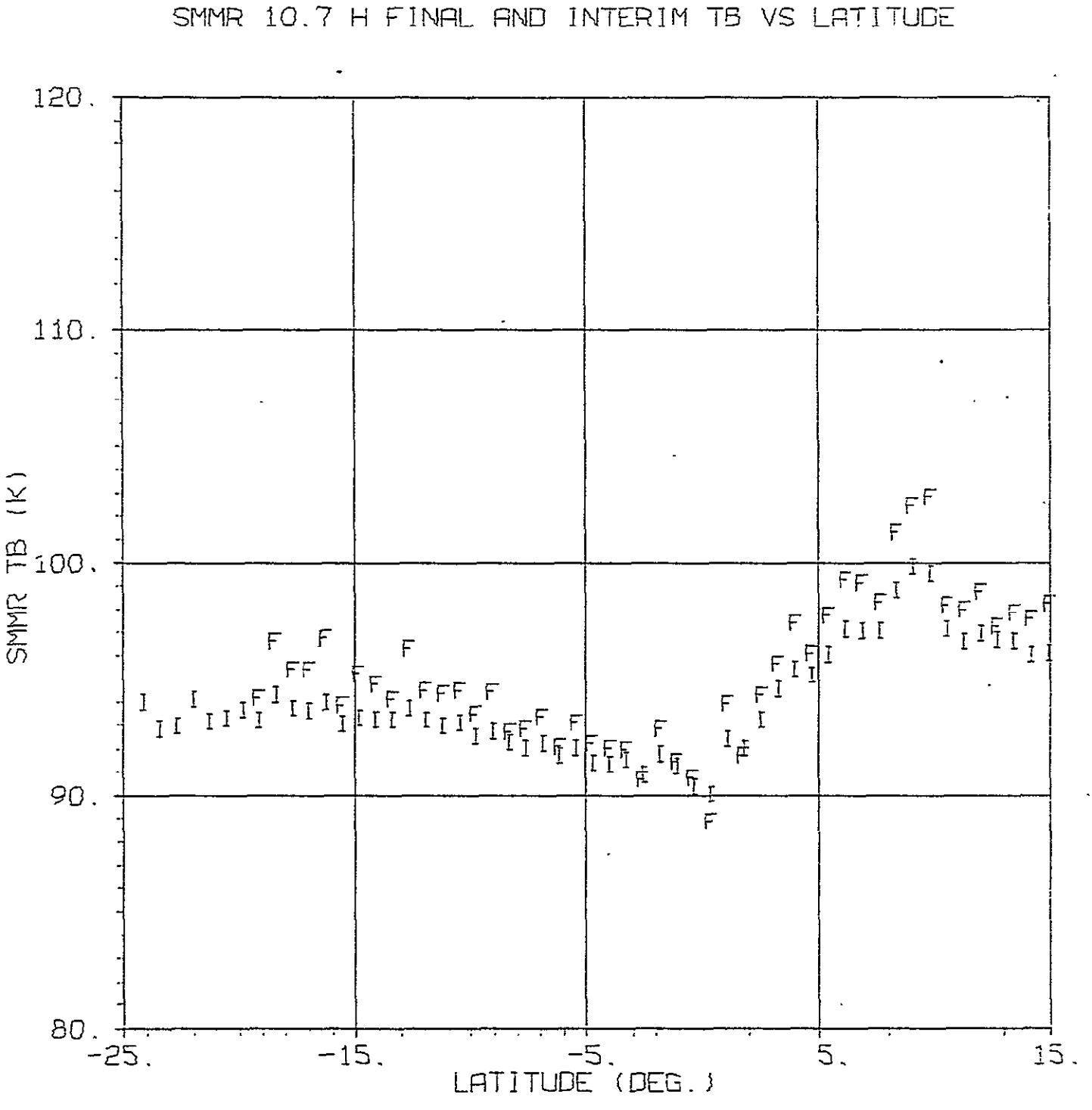

Figure 3.4. Orbit 1255, Grid 2, Column 7

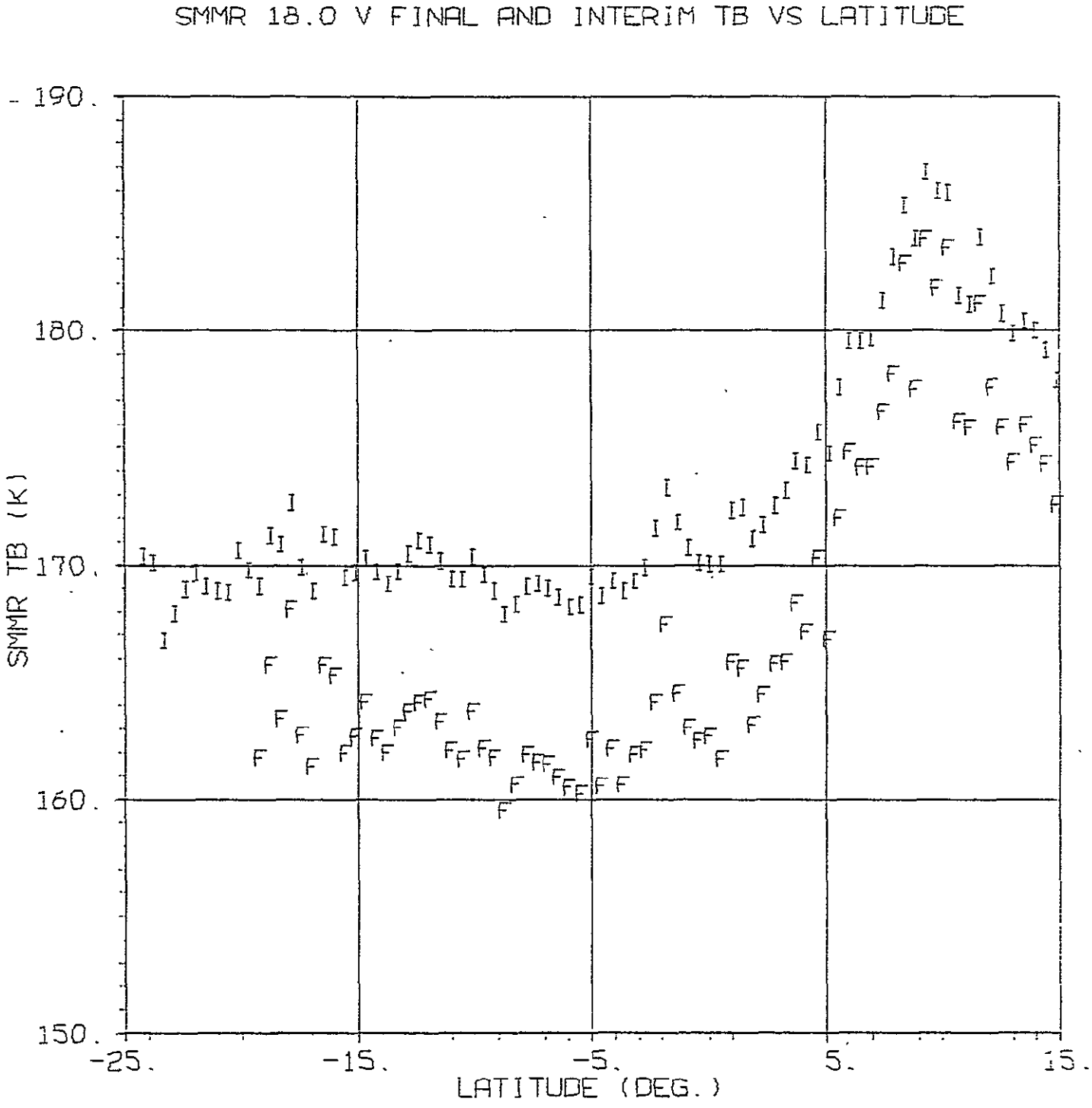

Figure 3.5. Orbit 1255, Grid 3, Column 11

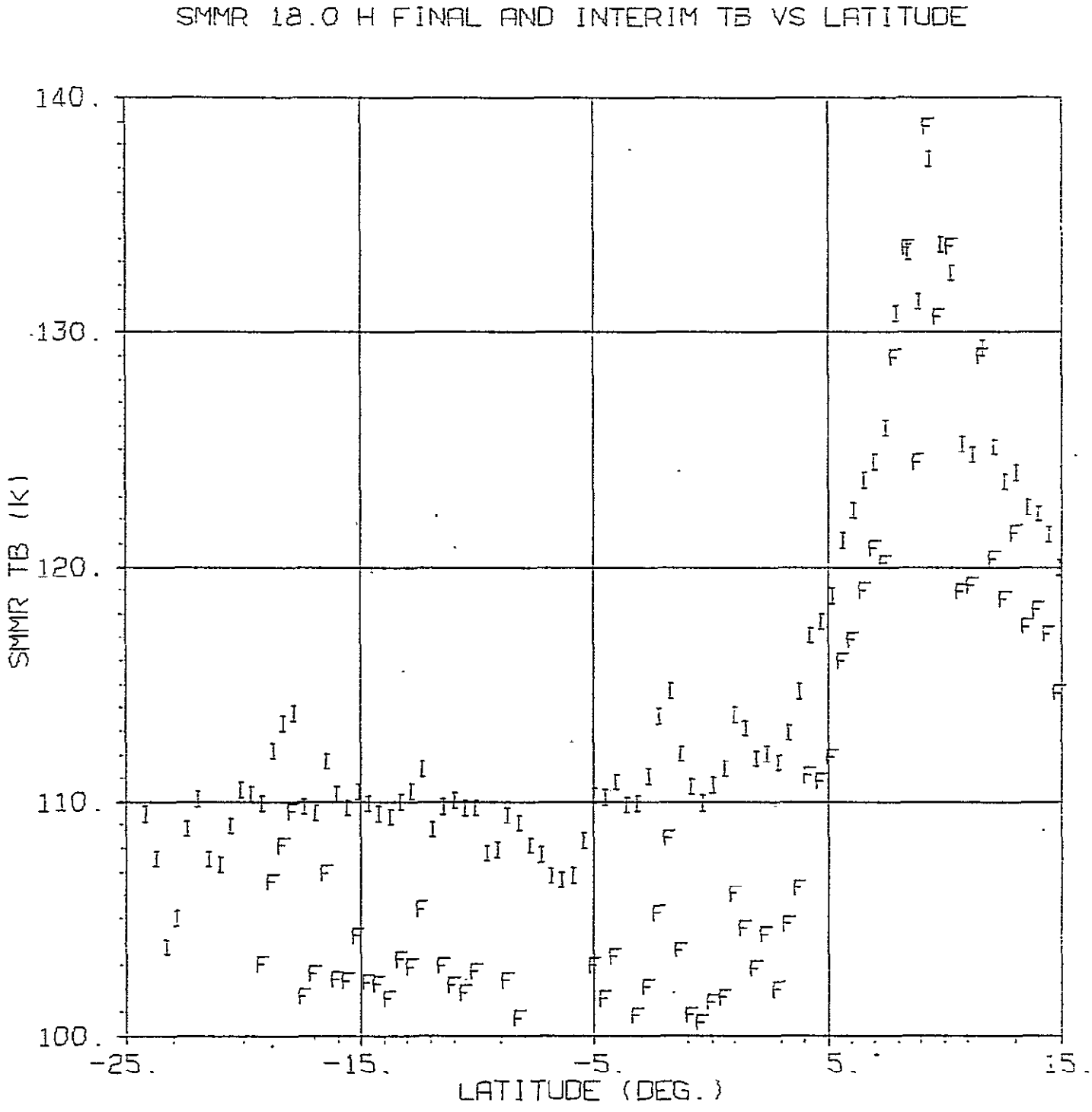

Figure 3.6. Orbit 1255, Grid 3, Column 11

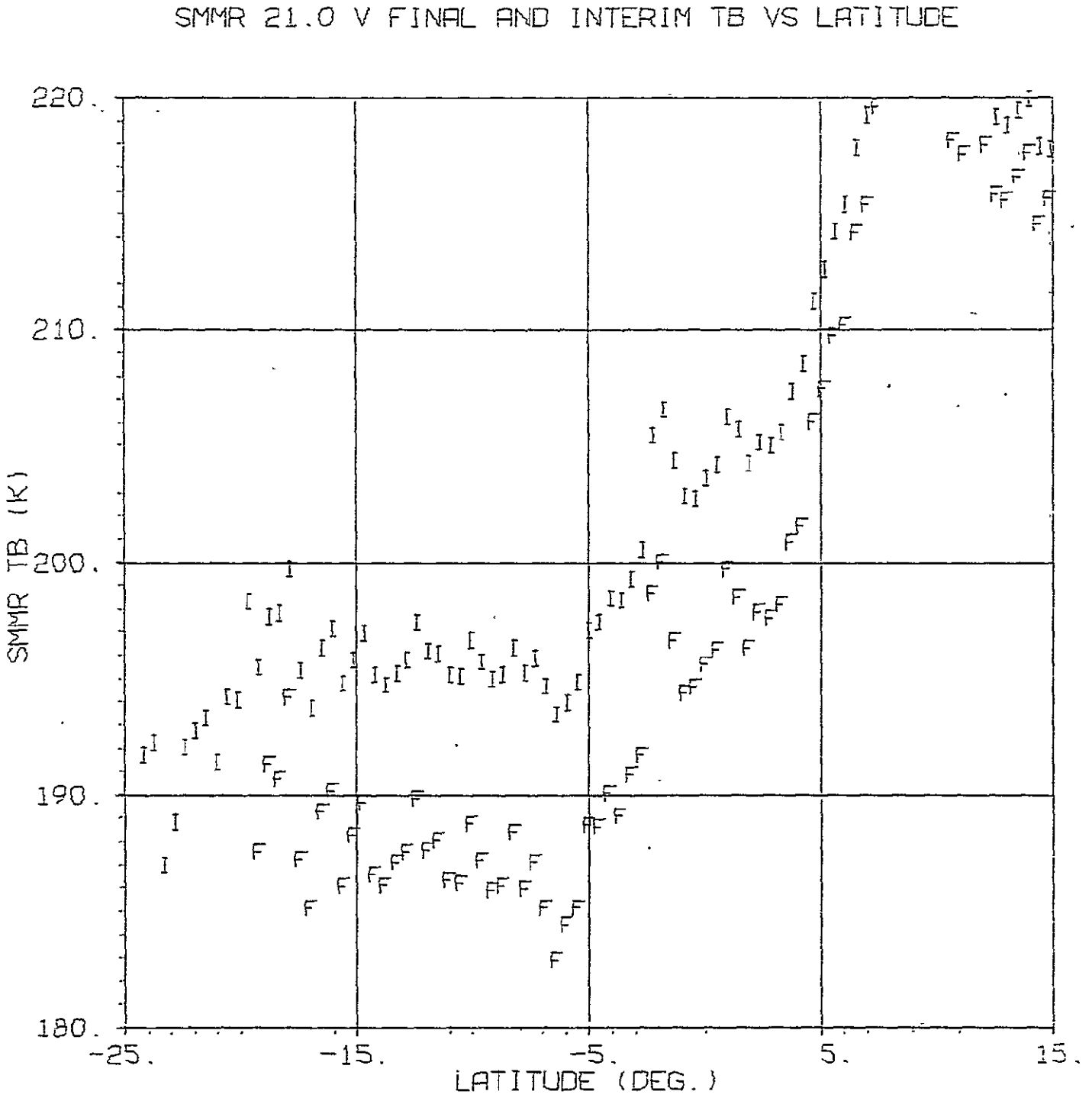

Figure 3.7. Orbit 1255, Grid 3, Column 11

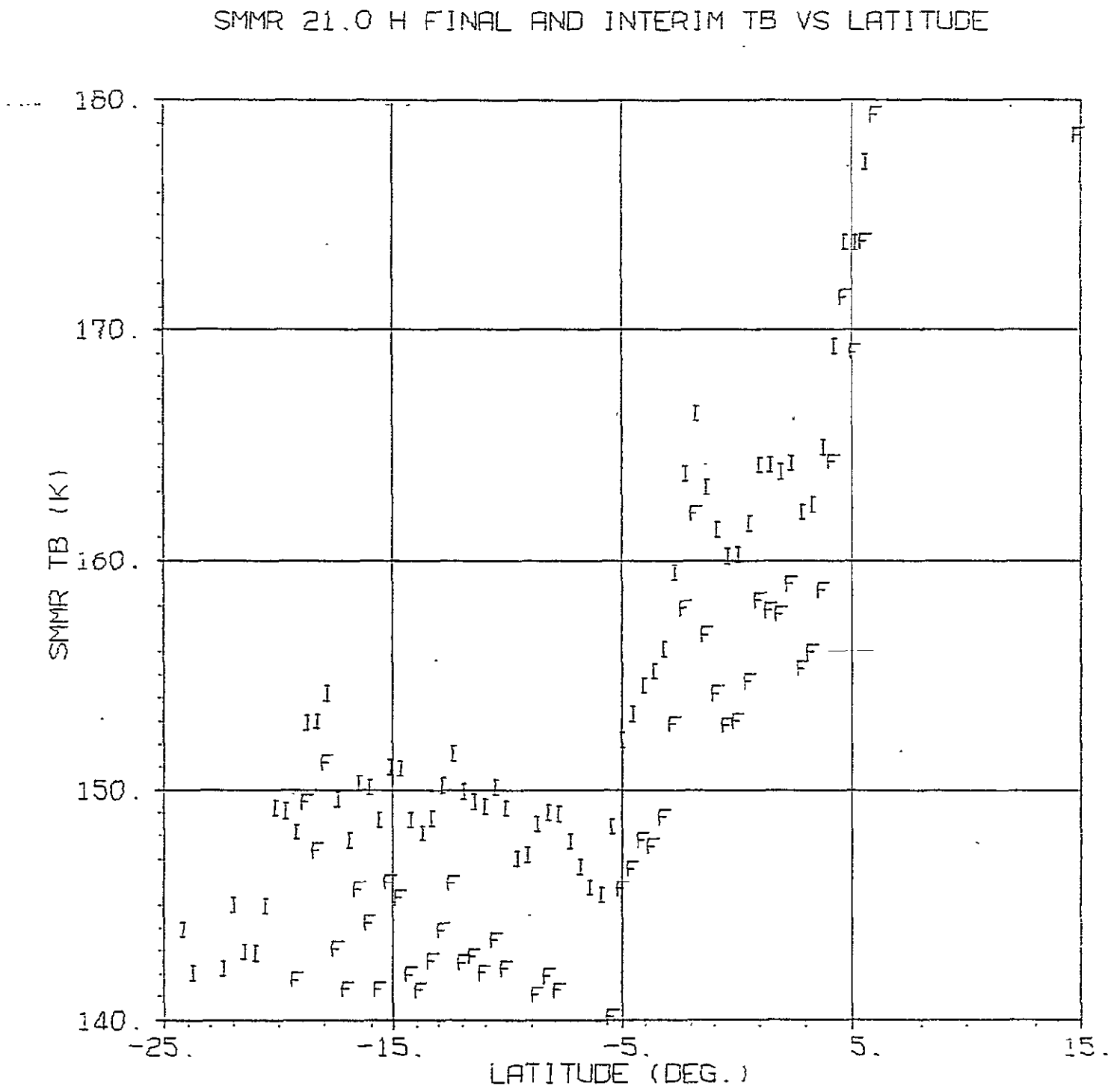

Figure 3.8. Orbit 1255, Grid 3, Column 11

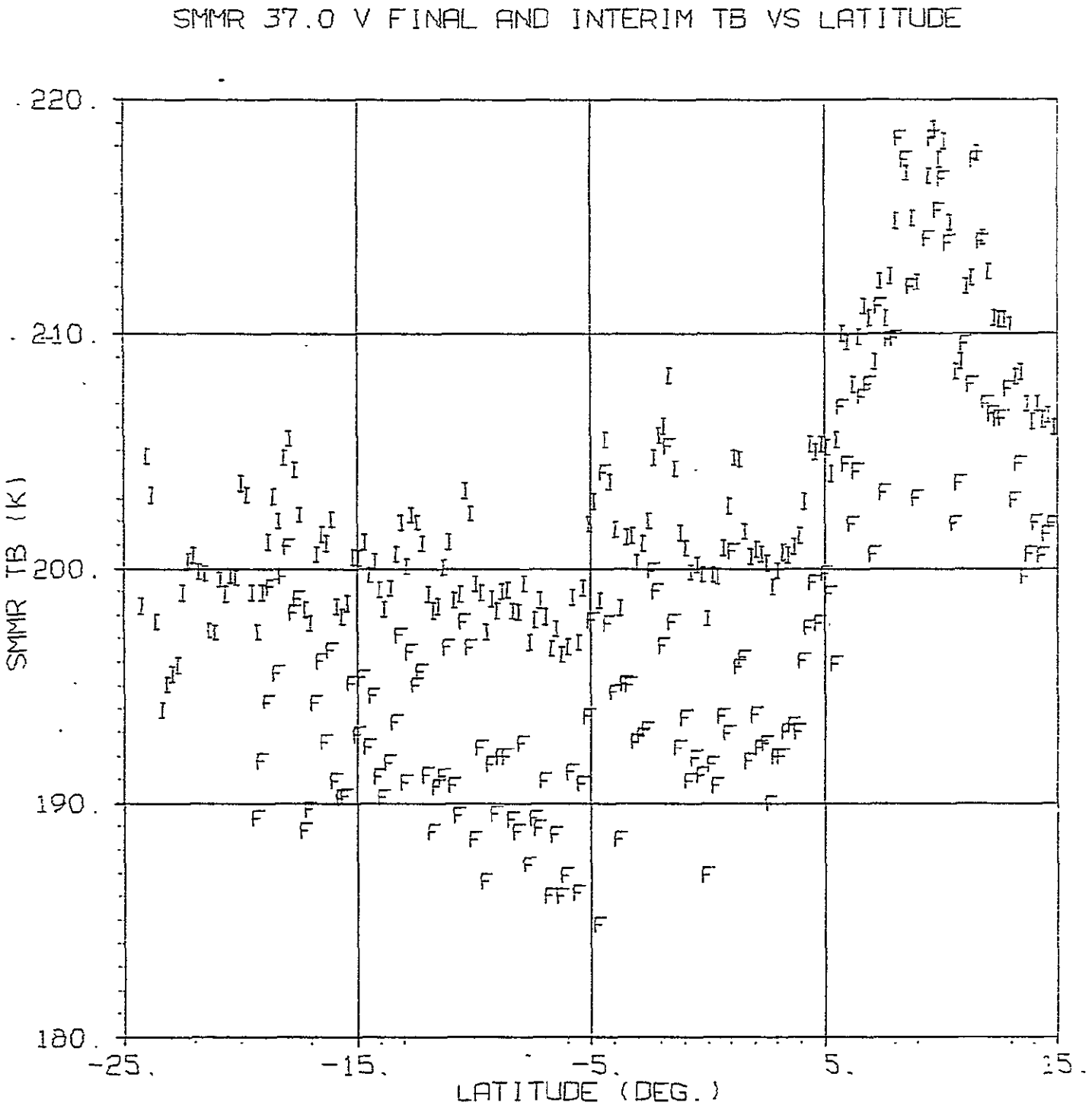

Figure 3.9. Orbit 1255, Grid 4, Column 22

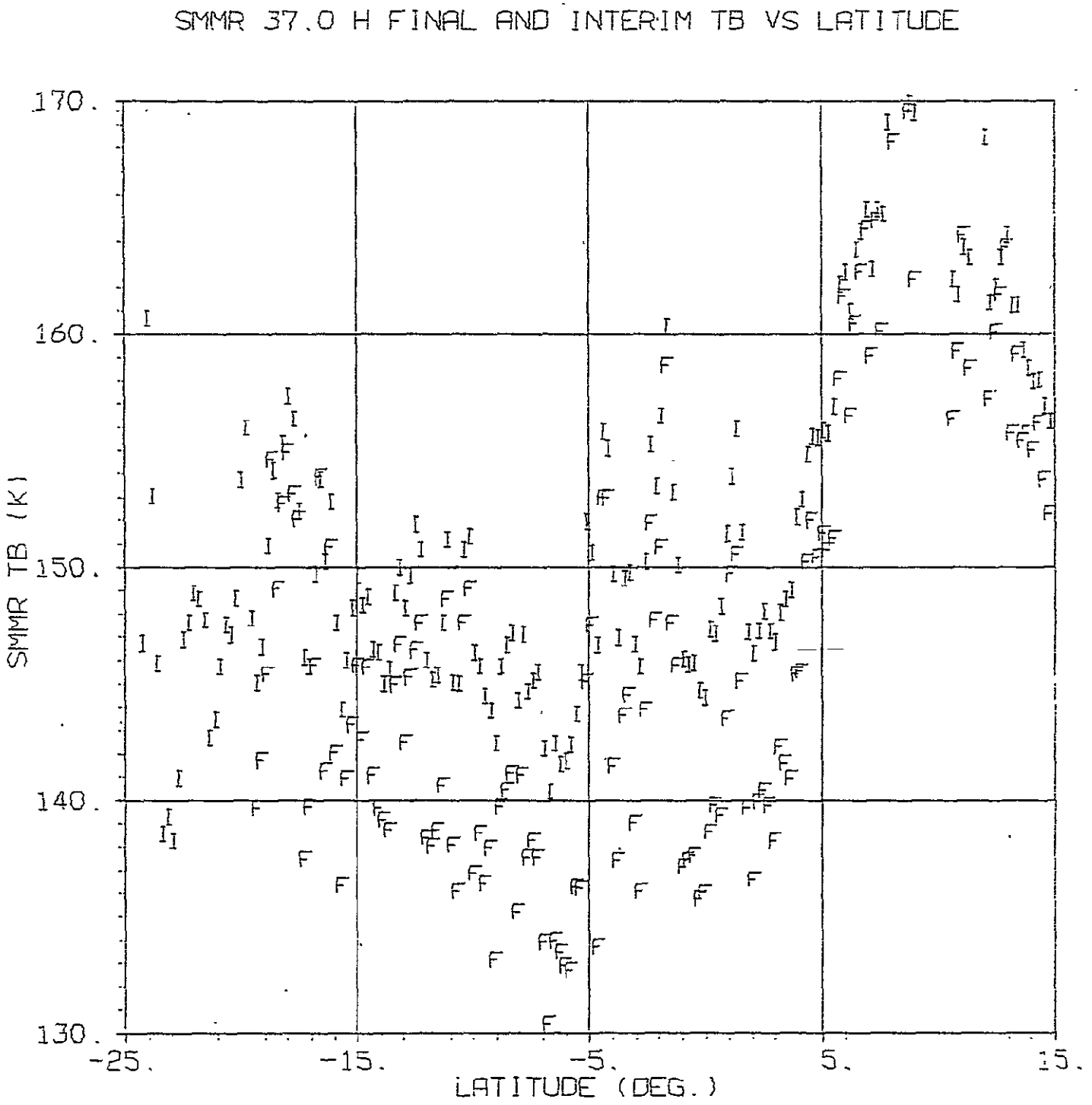

Figure 3.10. Orbit 1255, Grid 4, Column 22

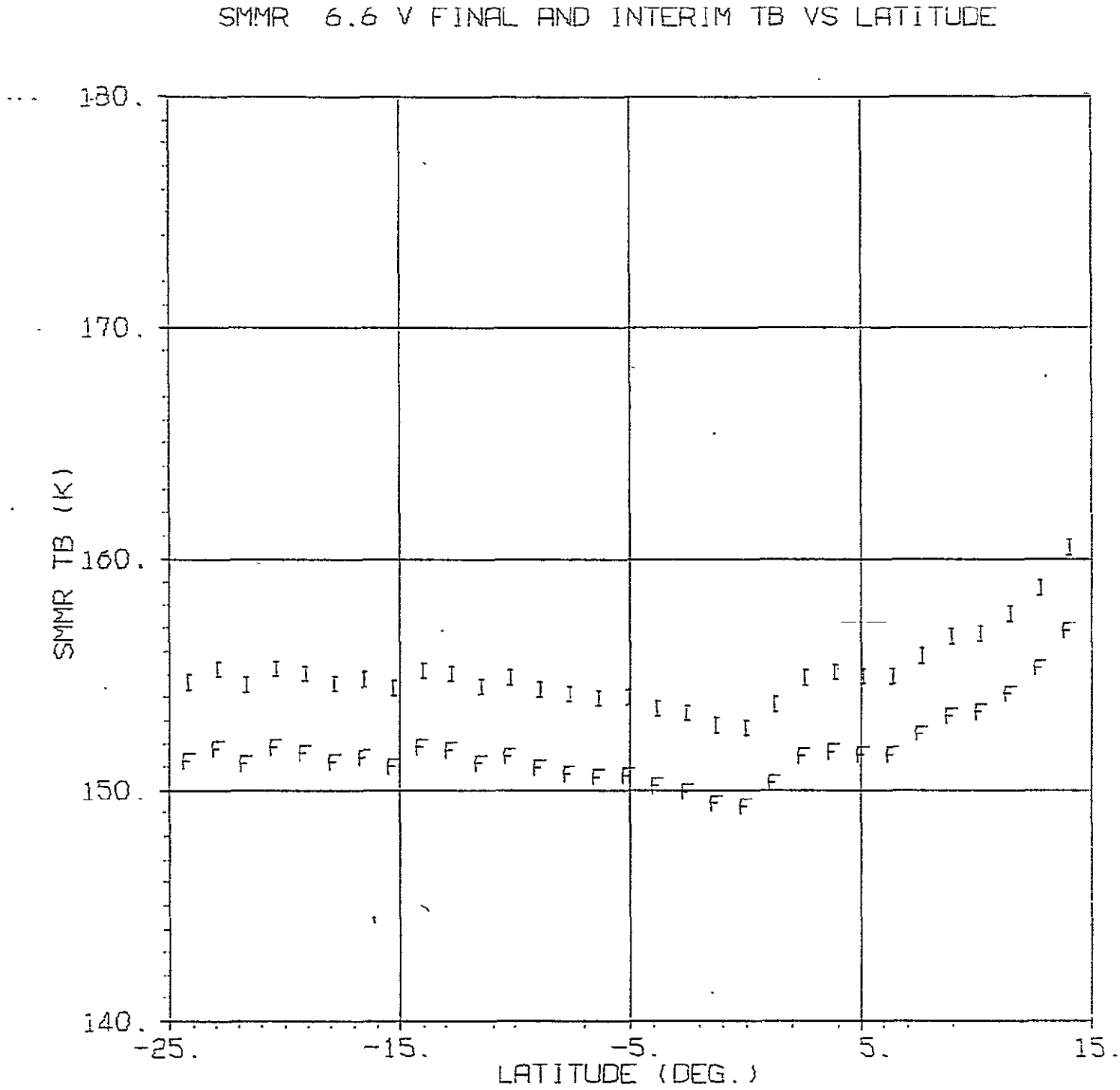

Figure 4.1. Orbit 1255, Grid 1, Column 1
Final Without Sidelobe Corrections

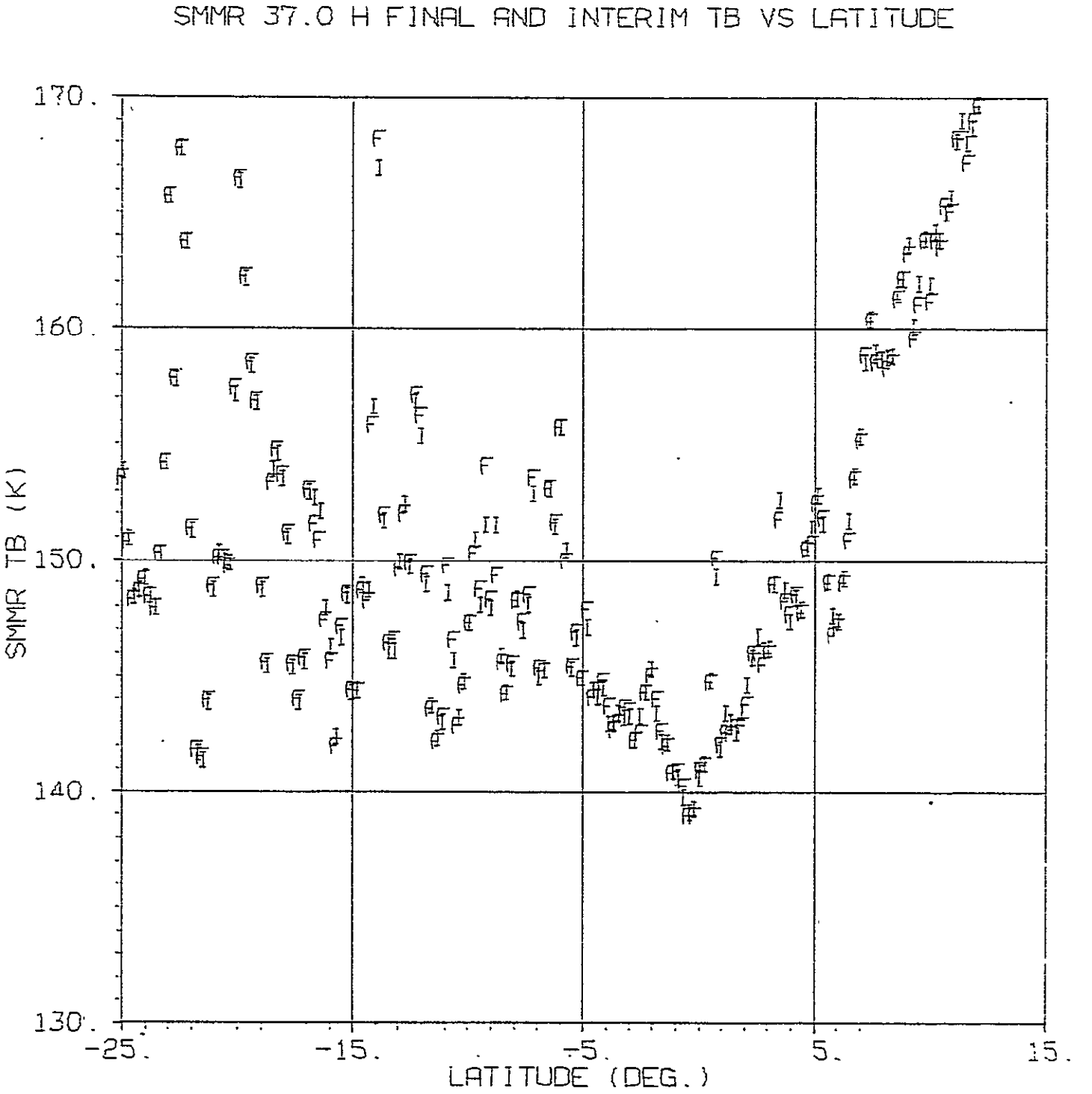

Figure 4.2. Orbit 1255, Grid 4, Column 1
Final Without Sidelobe Corrections

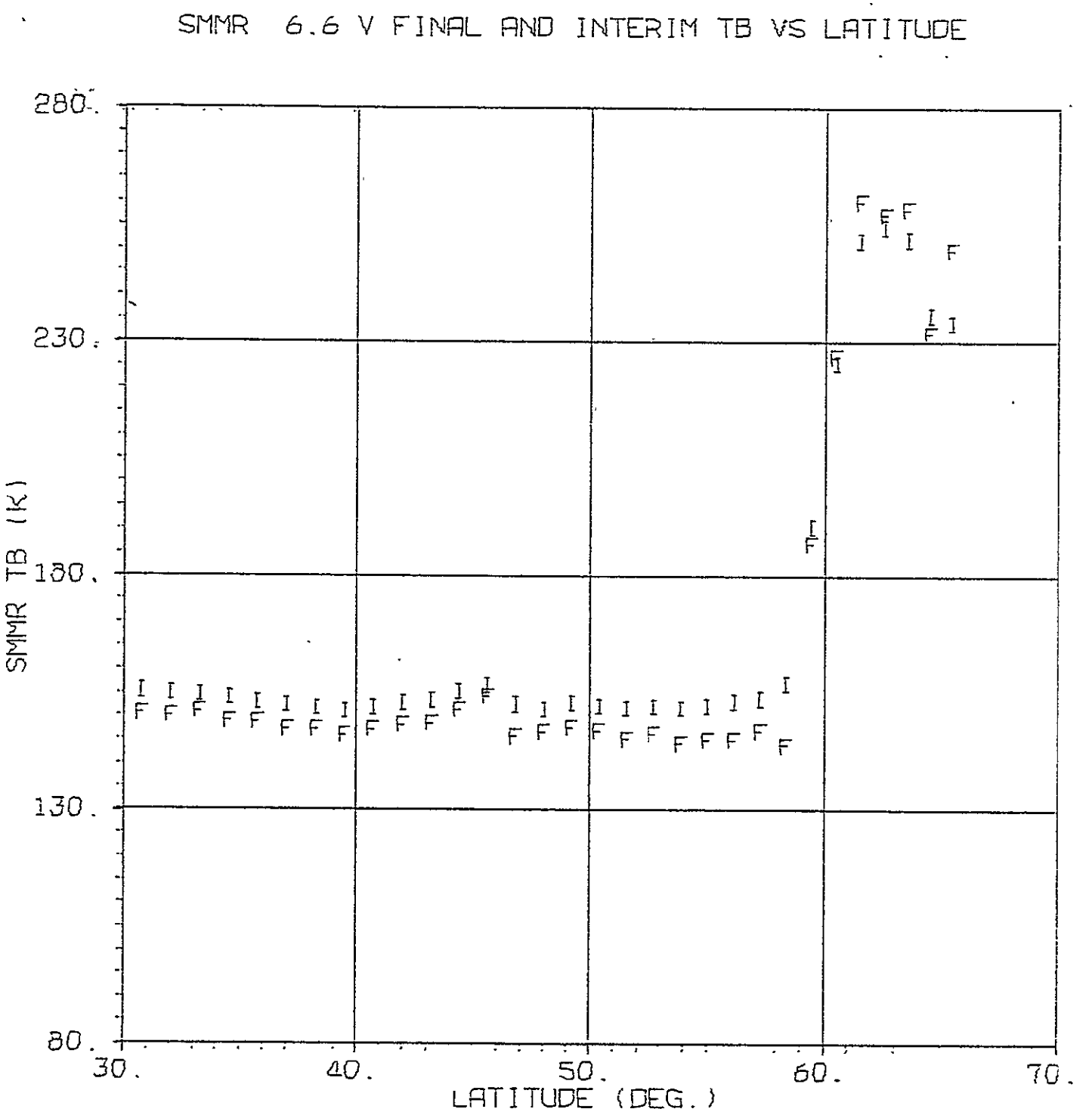

Figure 5.1. Orbit 1212, Grid 1, Column 1

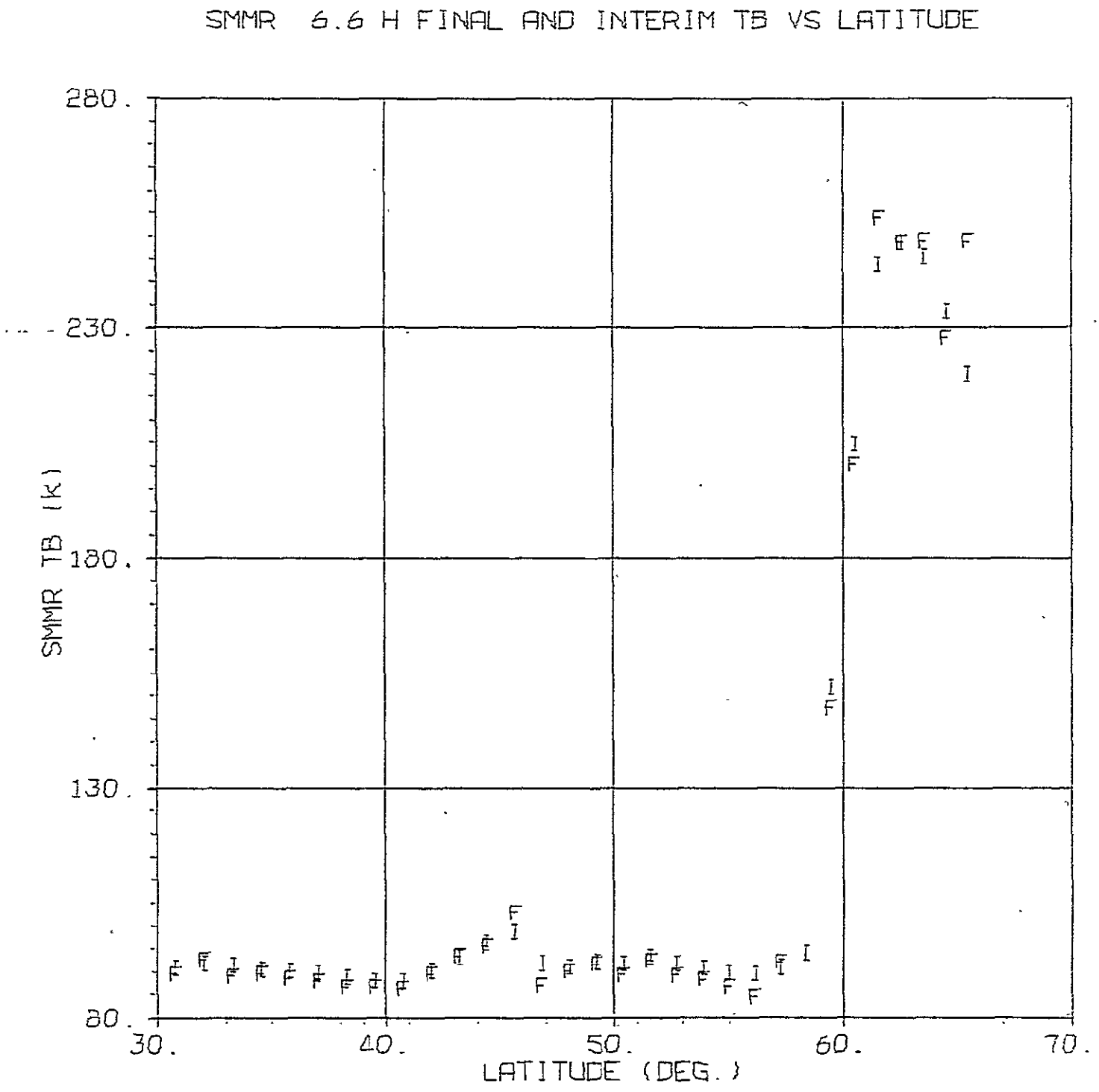

Figure 5.2. Orbit 1212, Grid 1, Column 1

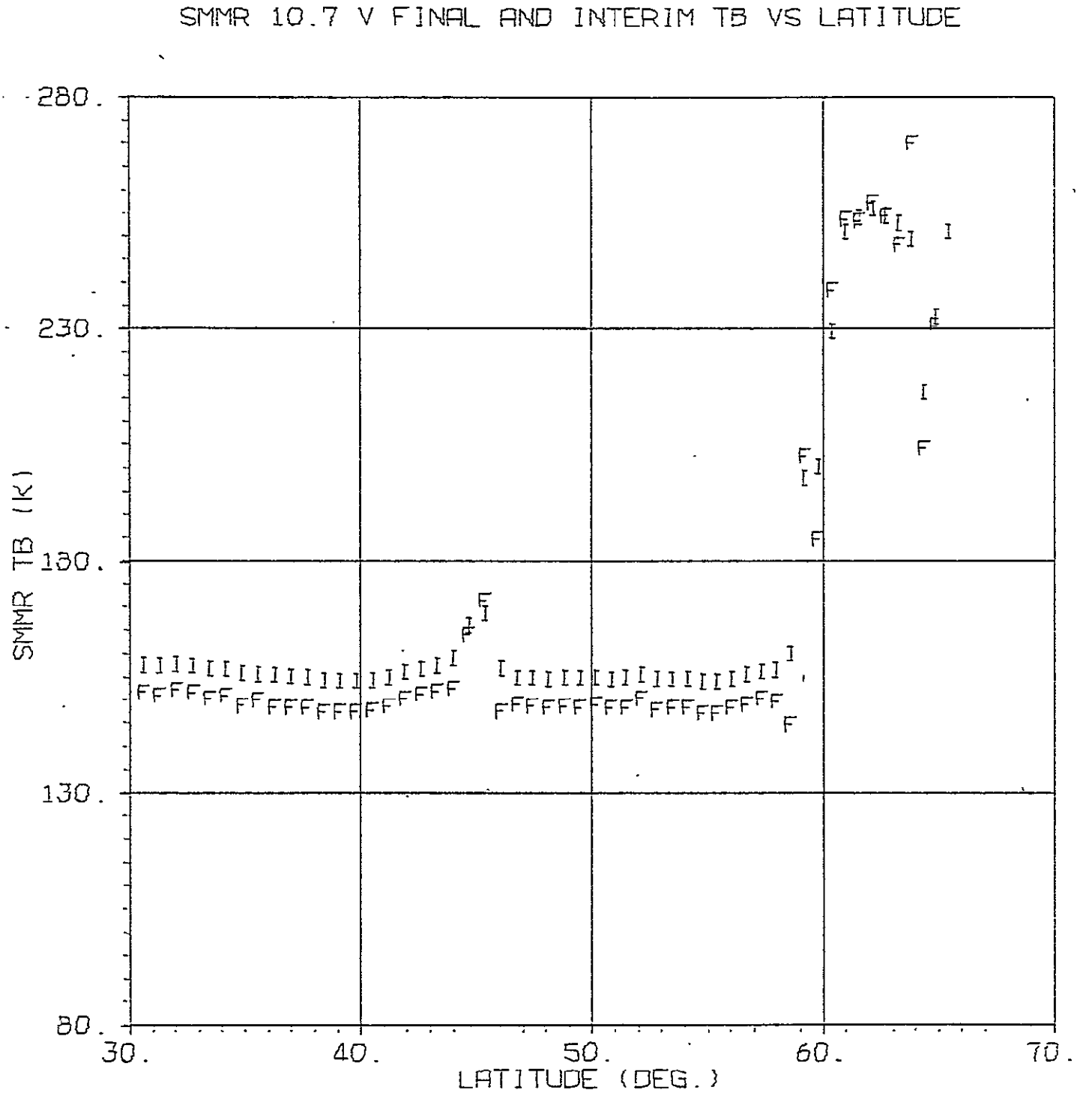

Figure 5.3. Orbit 1212, Grid 2, Column 1

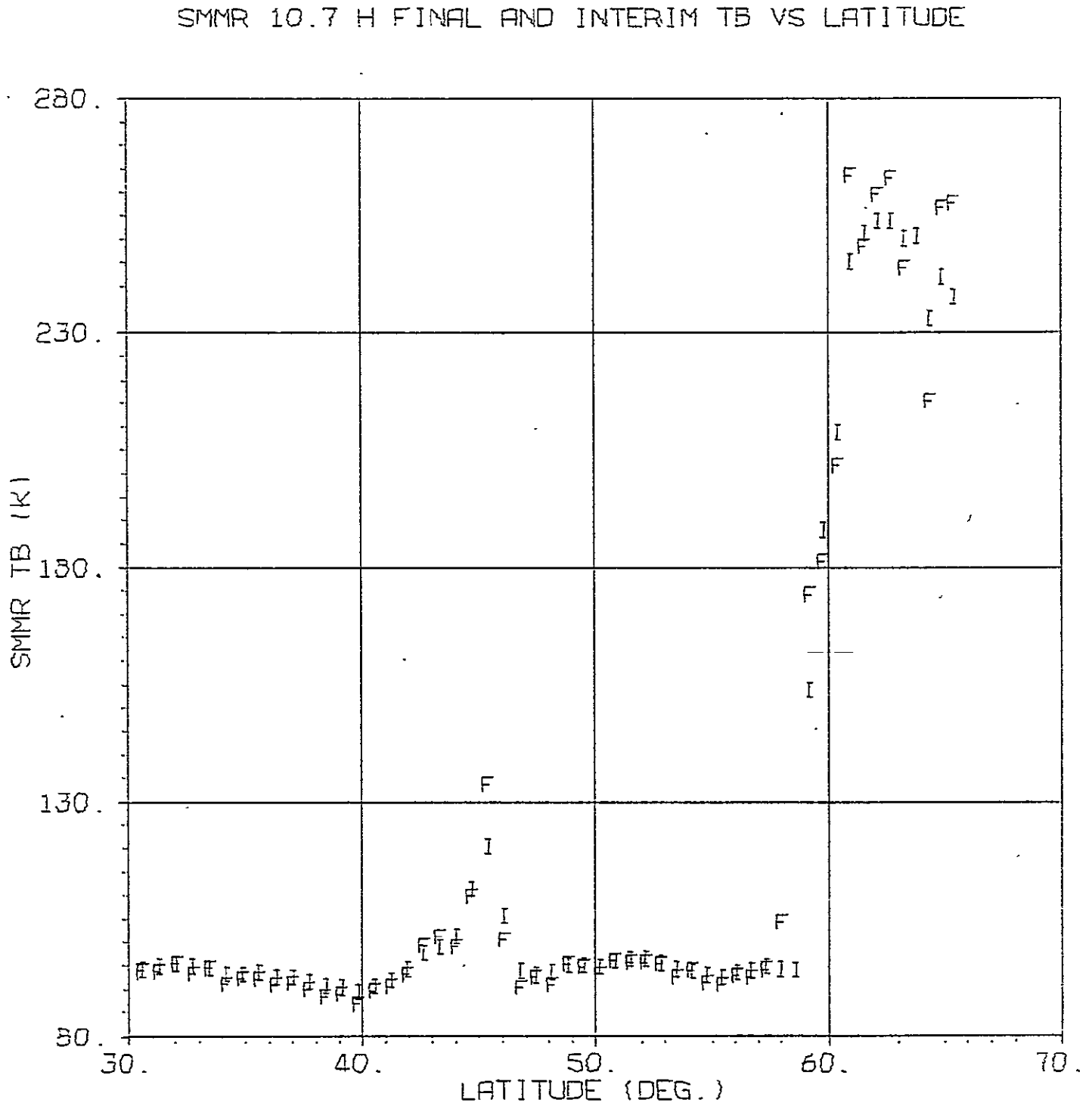

Figure 5.4. Orbit 1212, Grid 2, Column 1

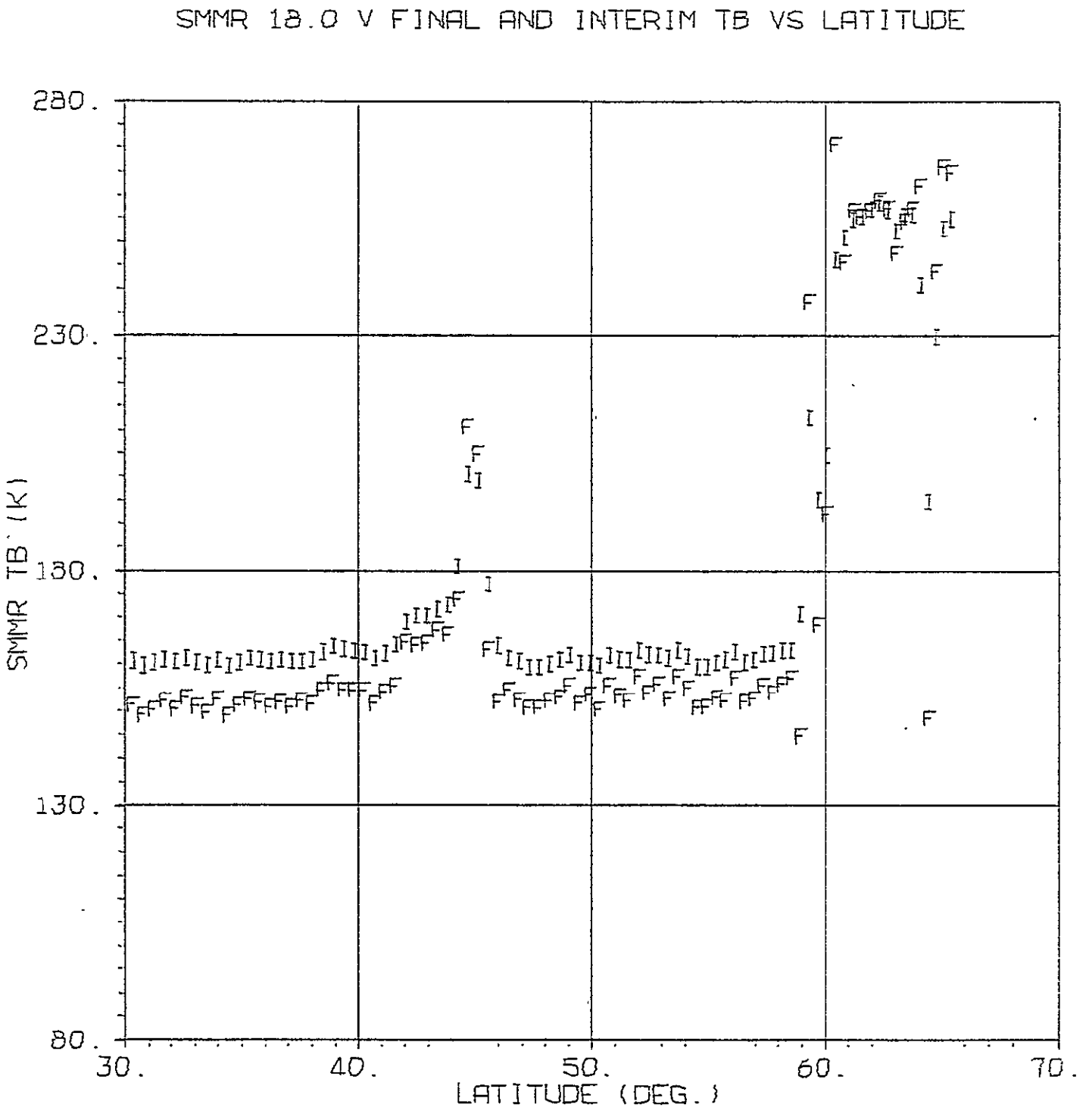

Figure 5.5. Orbit 1212, Grid 3, Column 1

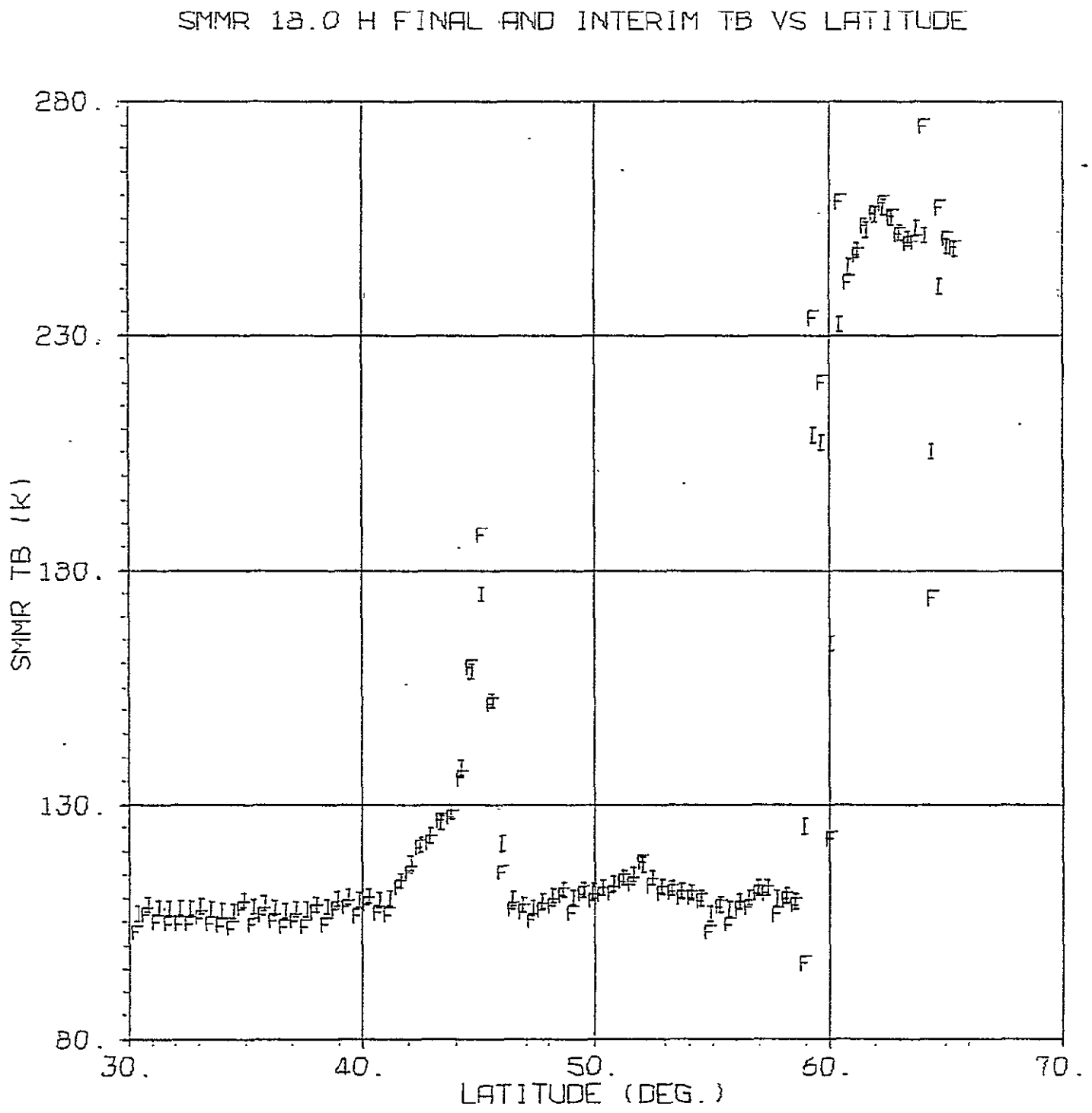

Figure 5.6. Orbit 1212, Grid 3, Column 1

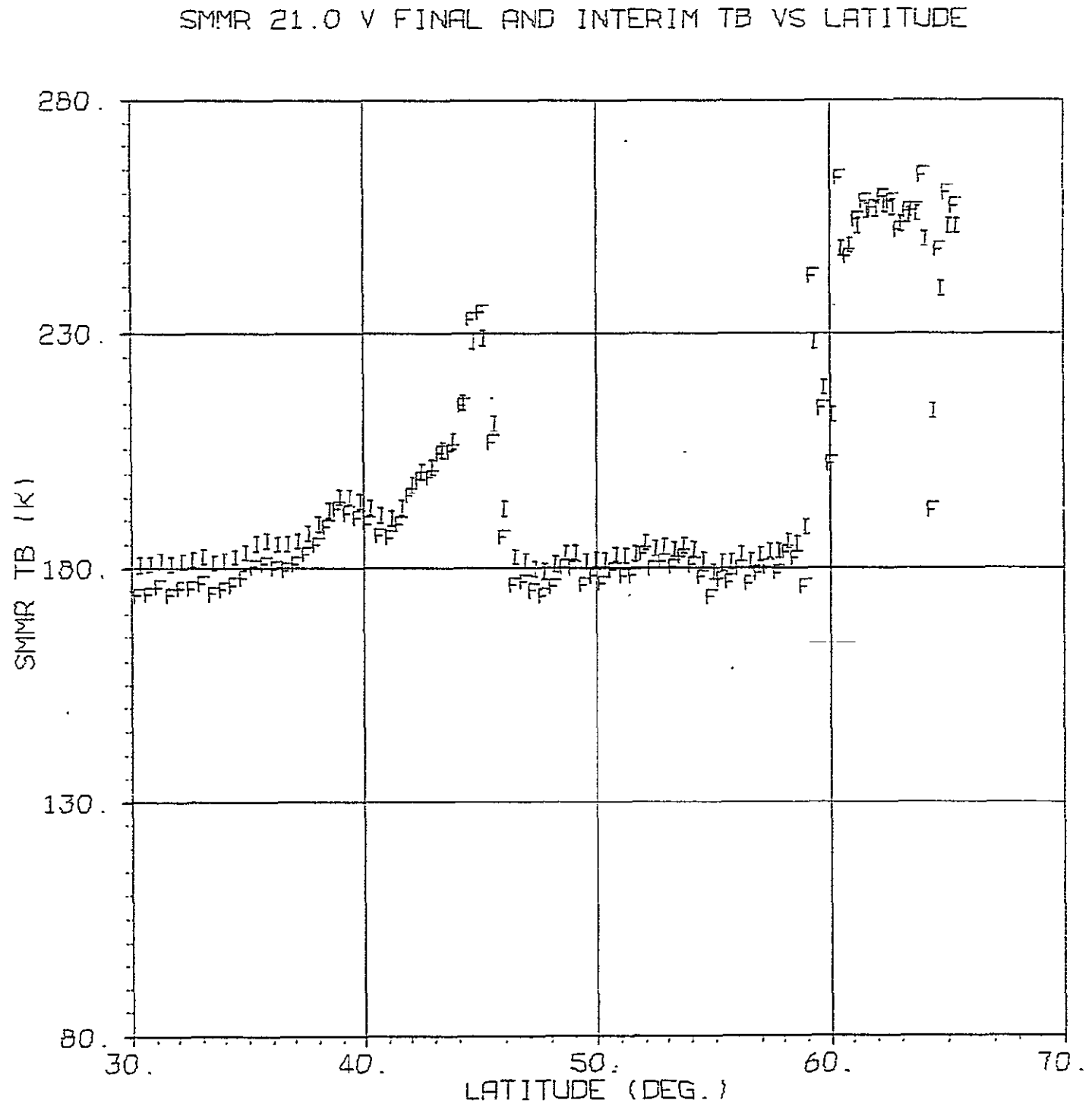

Figure 5.7. Orbit 1212, Grid 3, Column 1

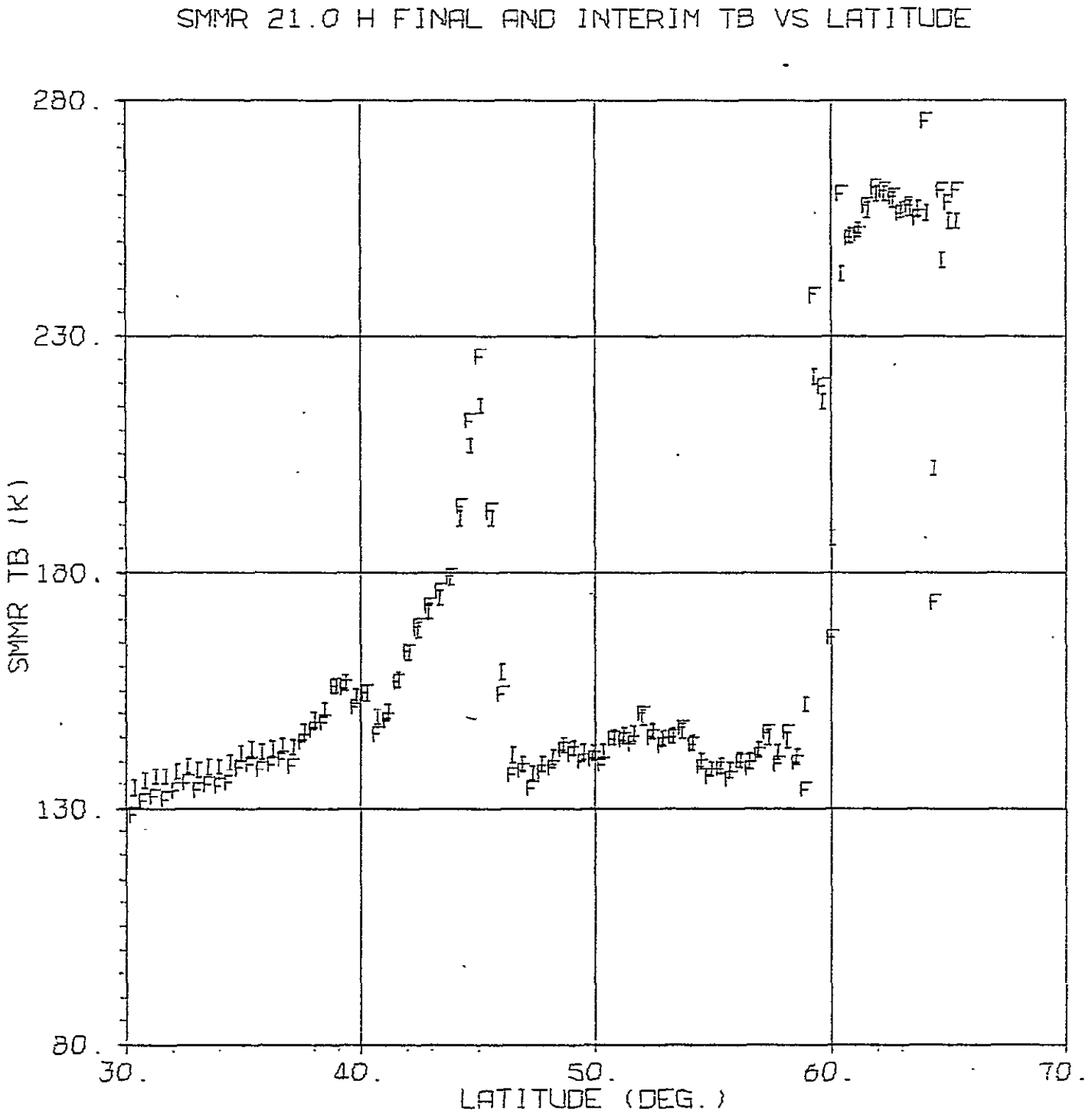

Figure 5.8. Orbit 1212, Grid 3, Column 1

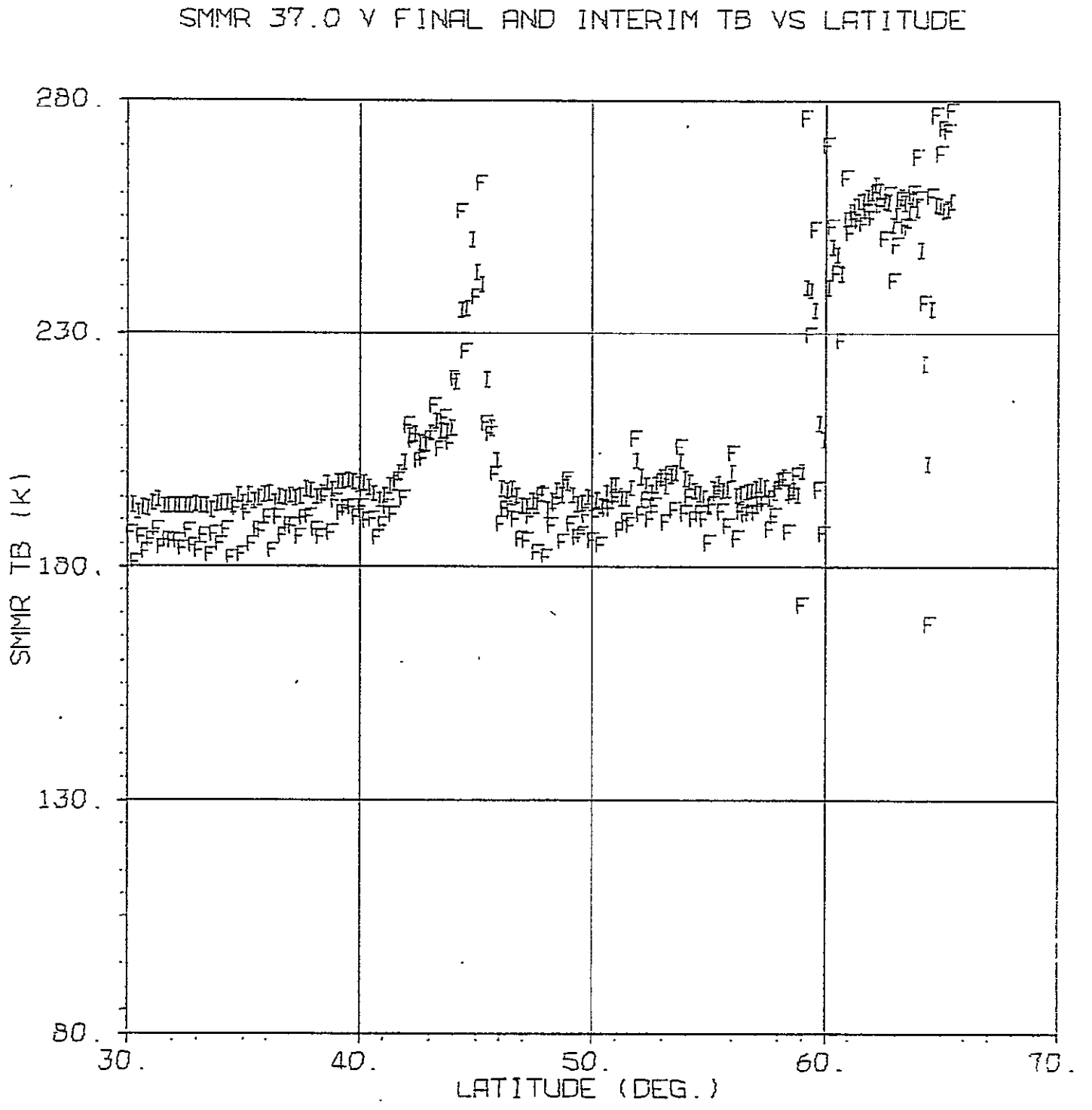

Figure 5.9. Orbit 1212, Grid 4, Column 1

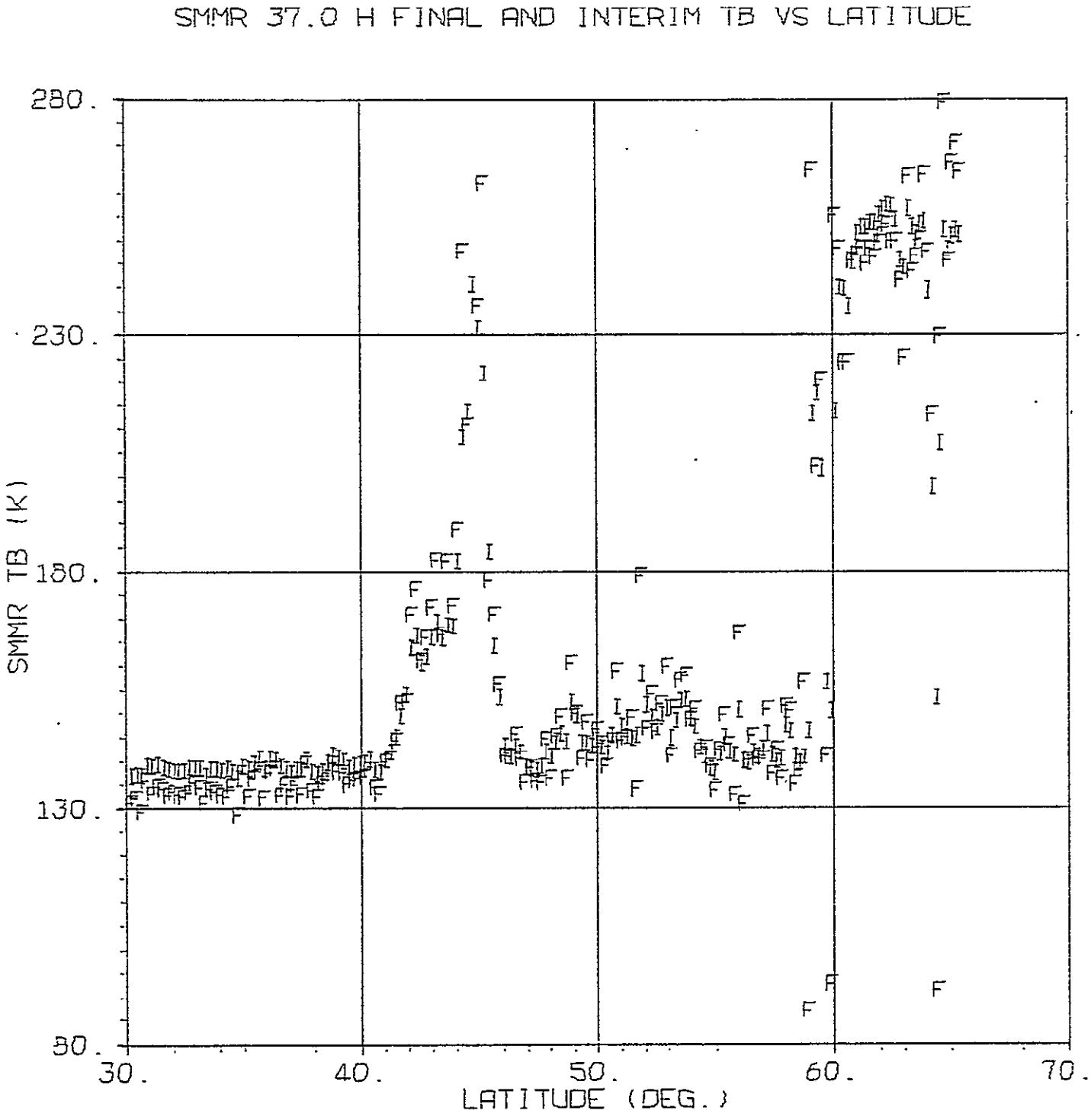

Figure 5.10. Orbit 1212, Grid 4, Column 1

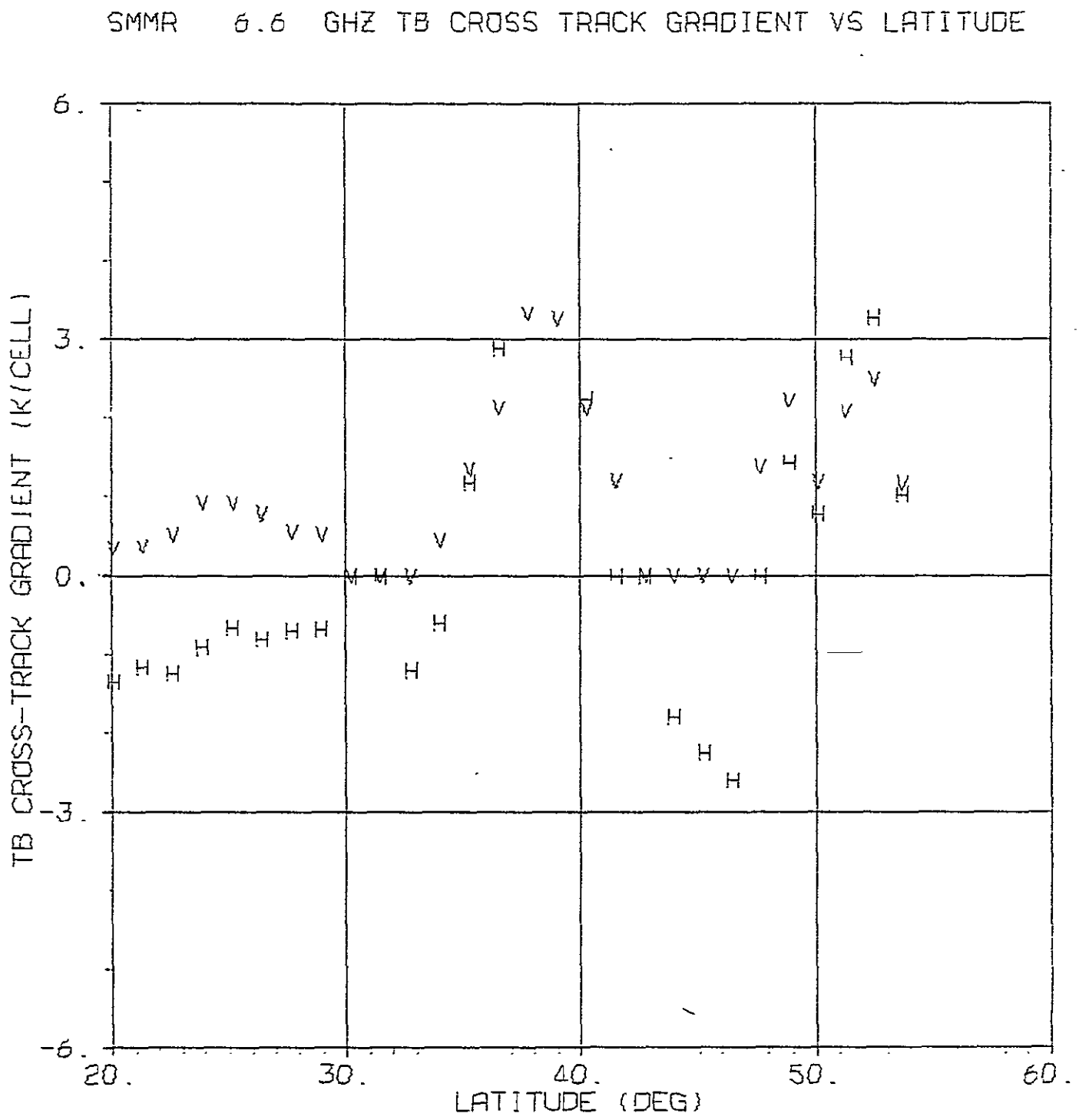

Figure 6.1. Orbit 1212, Interim APC

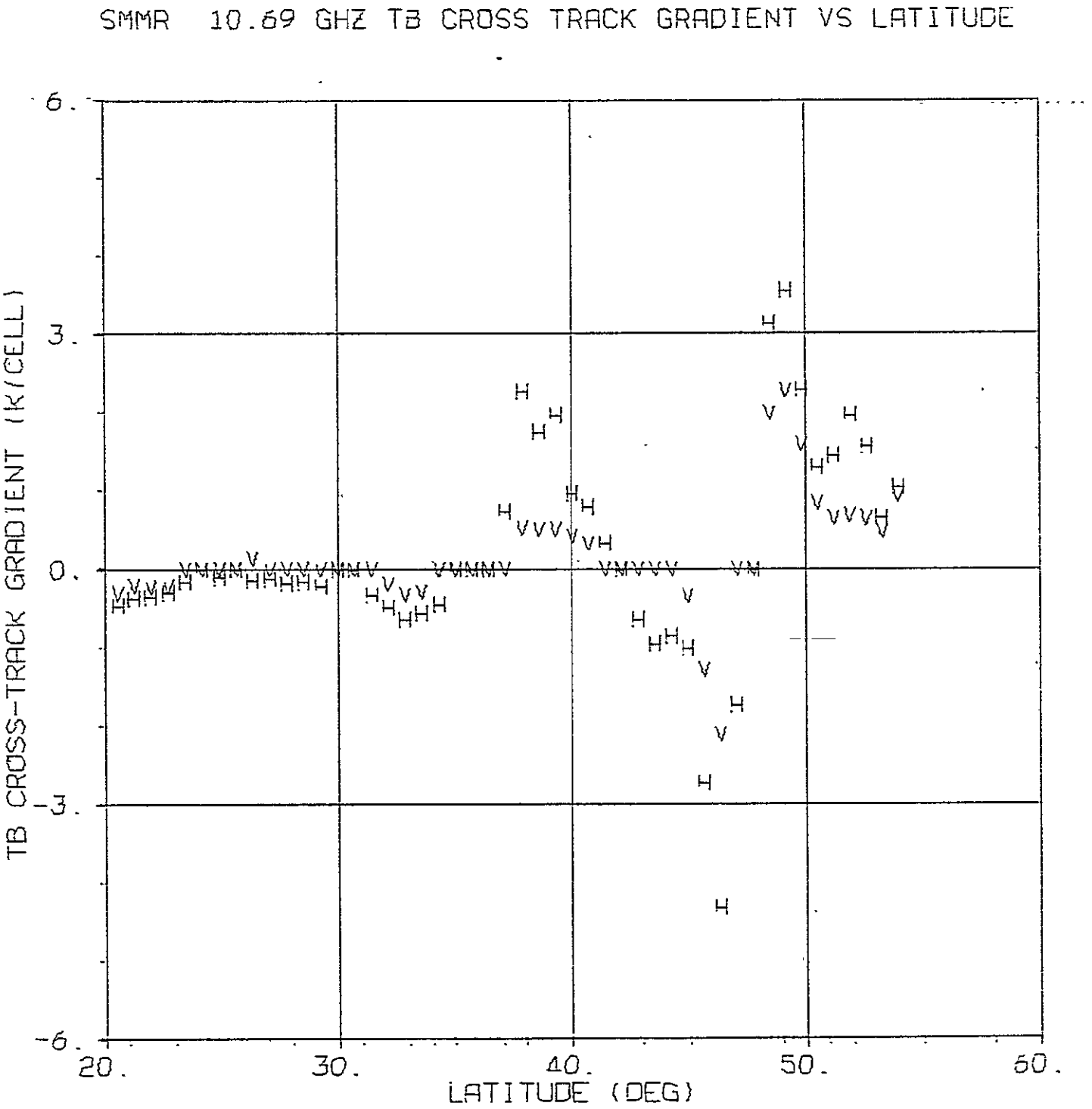

Figure 6.2. Orbit 1212, Interim APC

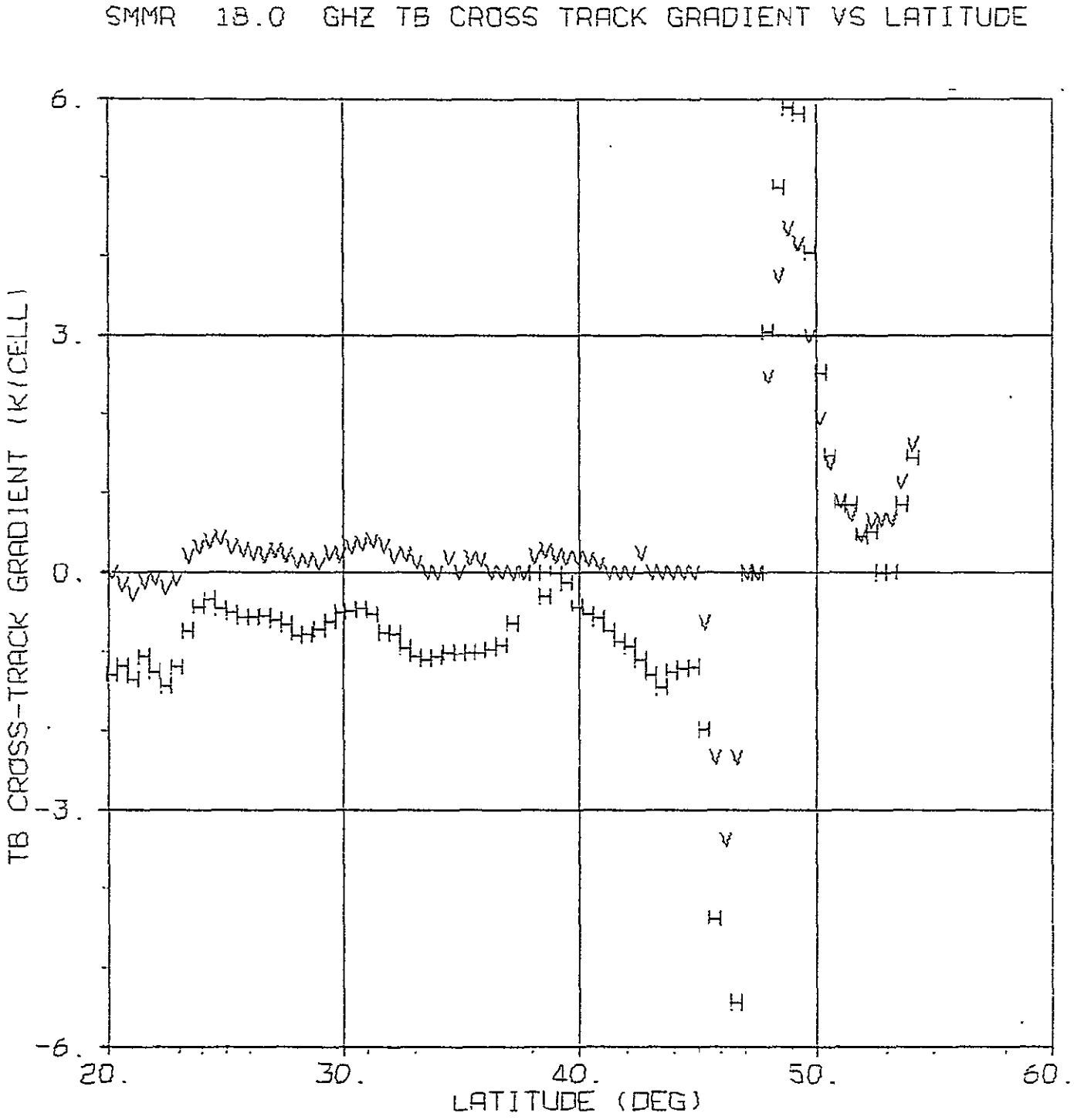

Figure 6.3. Orbit 1212, Interim APC

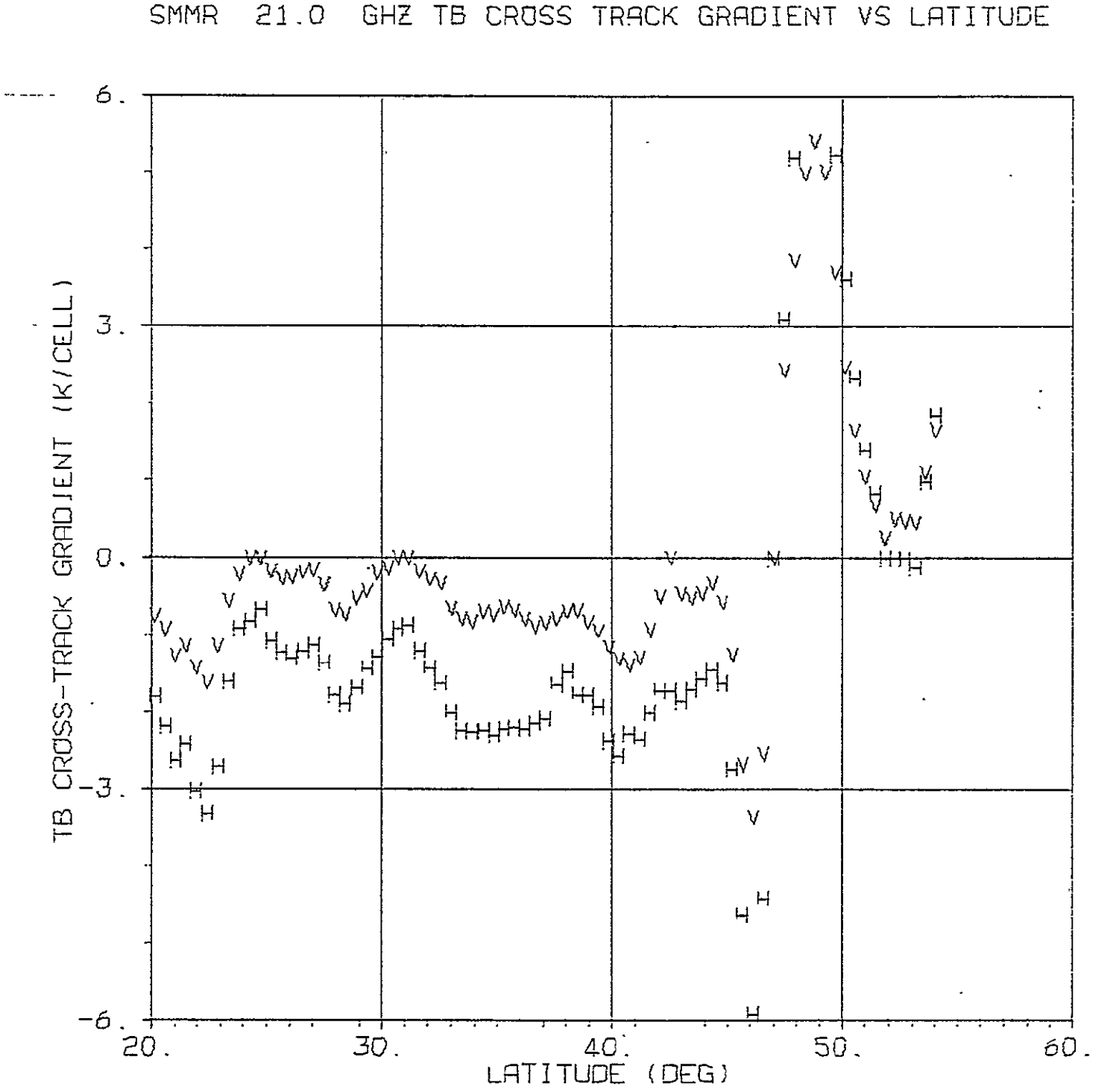

Figure 6.4. Orbit 1212, Interim APC

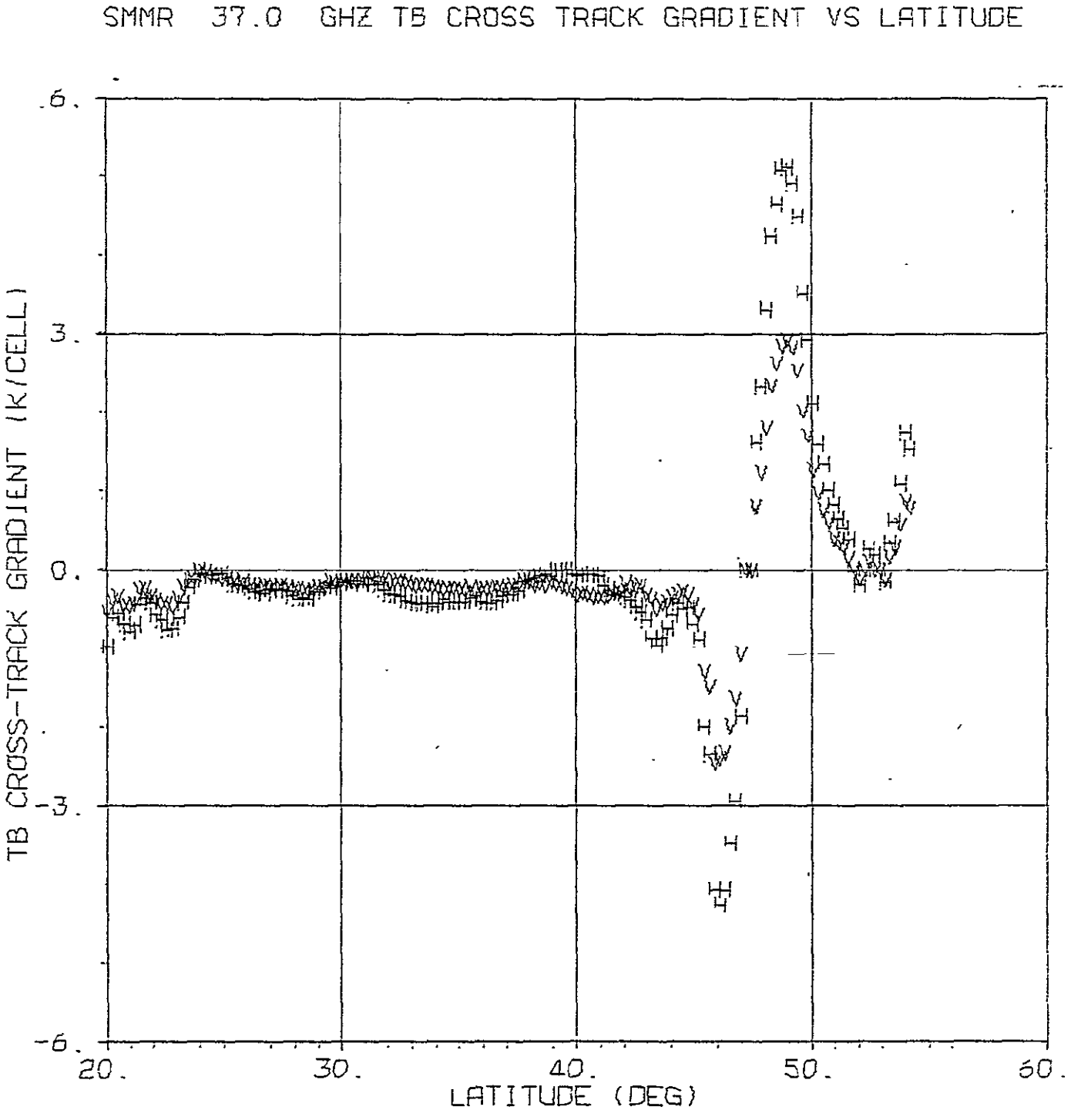

Figure 6.5. Orbit 1212, Interim APC

Table 6. Orbit 1212, Interim APC

CURVE FITS FOR SMMR 18.0 GHZ TB VERSUS CELL NUMBER

			V POL.			H POL.		
BLOCK	ROW	AVERAGE LATITUDE	LINEAR TERM	CONSTANT TERM	RMS	LINEAR TERM	CONSTANT TERM	RMS
1	1	19.66	.000	174.293	.803	-1.075	125.613	.920
	2	20.13	.000	173.919	1.421	-1.291	125.890	1.395
	3	20.59	-.159	172.821	.722	-1.178	122.725	.728
	4	21.05	-.278	172.719	.834	-1.345	122.739	1.046
	5	21.52	-.115	171.229	.699	-1.075	120.186	1.039
	6	21.98	-.085	170.218	.747	-1.258	120.291	.385
	7	22.44	-.197	169.579	.613	-1.434	118.854	.775
	8	22.90	-.084	167.544	.630	-1.194	115.241	.966
	9	23.37	.202	164.917	.659	-.739	111.475	.800
	10	23.83	.321	163.491	.426	-.432	108.910	.792
	11	24.29	.394	162.415	.547	-.345	107.517	.776
2	1	24.75	.424	161.611	.561	-.450	107.400	.670
	2	25.21	.316	161.641	.391	-.500	107.297	.447
	3	25.67	.278	161.666	.639	-.574	107.468	.931
	4	26.14	.237	161.925	.594	-.574	107.562	.623
	5	26.60	.222	162.175	.639	-.544	107.757	.528
	6	27.06	.261	162.387	.557	-.606	108.778	.750
	7	27.52	.228	162.747	.391	-.656	109.217	.616
	8	27.98	.118	163.193	.431	-.788	109.688	.476
	9	28.44	.136	162.420	.342	-.781	109.155	.501
	10	28.90	.115	162.023	.422	-.726	108.381	.677
	11	29.36	.240	160.935	.290	-.627	107.851	.932
3	1	29.82	.223	161.372	.714	-.509	107.023	.809
	2	30.28	.320	160.632	.799	-.483	107.076	1.113
	3	30.74	.355	160.584	1.079	-.450	107.293	1.234
	4	31.20	.390	160.491	.840	-.535	107.905	1.379
	5	31.66	.329	160.651	.912	-.762	109.522	1.125
	6	32.12	.206	161.467	.889	-.777	109.591	1.171
	7	32.58	.212	161.065	.701	-.952	110.099	1.309
	8	33.04	.116	161.196	.680	-1.062	110.229	.879
	9	33.49	.000	162.040	.997	-1.104	110.359	1.092
	10	33.95	.000	162.455	1.187	-1.067	110.666	1.238
	11	34.41	.176	161.313	1.227	-1.005	110.514	1.516

Table 7. Orbit 1212, Final APC

CURVE FITS FOR SSMR 18.0 GHZ TB VERSUS CELL NUMBER

			V POL.			H POL.		
BLOCK	ROW	AVERAGE LATITUDE	LINEAR TERM	CONSTANT TERM	RMS	LINEAR TERM	CONSTANT TERM	RMS
1	1	19.67	-.463	171.750	2.618	-.719	121.457	2.676
	2	20.14	-.468	172.059	4.405	-.975	122.230	2.902
	3	20.60	-.535	169.330	2.711	-.692	117.094	3.506
	4	21.06	-.781	170.406	3.074	-1.175	119.523	3.308
	5	21.52	-.459	167.917	2.868	-.555	114.587	3.665
	6	21.99	-.402	166.730	3.365	-.948	116.346	2.636
	7	22.45	-.663	166.810	2.696	-1.169	114.729	3.344
	8	22.91	-.522	164.397	2.294	-.059	110.457	3.328
	9	23.37	.000	160.442	2.080	.000	104.384	3.942
	10	23.84	.000	159.575	2.979	.000	103.674	3.419
	11	24.30	.000	158.892	2.512	.000	102.796	3.382
2	1	24.76	.000	158.341	2.762	.000	101.899	3.991
	2	25.22	.000	157.517	2.440	.000	101.521	3.279
	3	25.69	.000	157.403	3.254	.000	101.215	3.850
	4	26.15	.000	157.530	2.969	.000	101.305	3.889
	5	26.61	.000	157.518	2.564	.000	101.593	3.318
	6	27.07	.000	158.492	3.369	.000	102.318	4.206
	7	27.53	.000	156.335	2.730	.000	102.673	3.072
	8	27.99	.000	156.253	2.934	-.392	104.748	3.276
	9	28.45	.000	157.387	2.486	-.310	103.588	2.860
	10	28.91	.000	156.935	3.145	.000	101.343	3.659
	11	29.37	.000	156.398	2.070	.000	101.327	3.996
3	1	29.83	.000	157.189	3.256	.000	101.196	4.406
	2	30.29	.000	156.615	2.970	.000	101.432	3.496
	3	30.75	.000	157.092	3.199	.000	102.111	4.186
	4	31.21	.000	157.268	2.869	.000	101.862	4.088
	5	31.67	.000	156.761	3.249	-.433	105.090	3.744
	6	32.13	.000	157.215	3.699	.000	102.415	3.928
	7	32.59	.000	156.706	2.769	-.549	105.237	3.317
	8	33.05	.000	156.118	3.336	-.631	105.170	2.639
	9	33.50	-.373	156.669	2.915	-.741	105.491	3.478
	10	33.96	.000	157.024	3.621	-.701	106.135	4.026
	11	34.42	.000	156.633	3.513	-.603	105.575	3.719

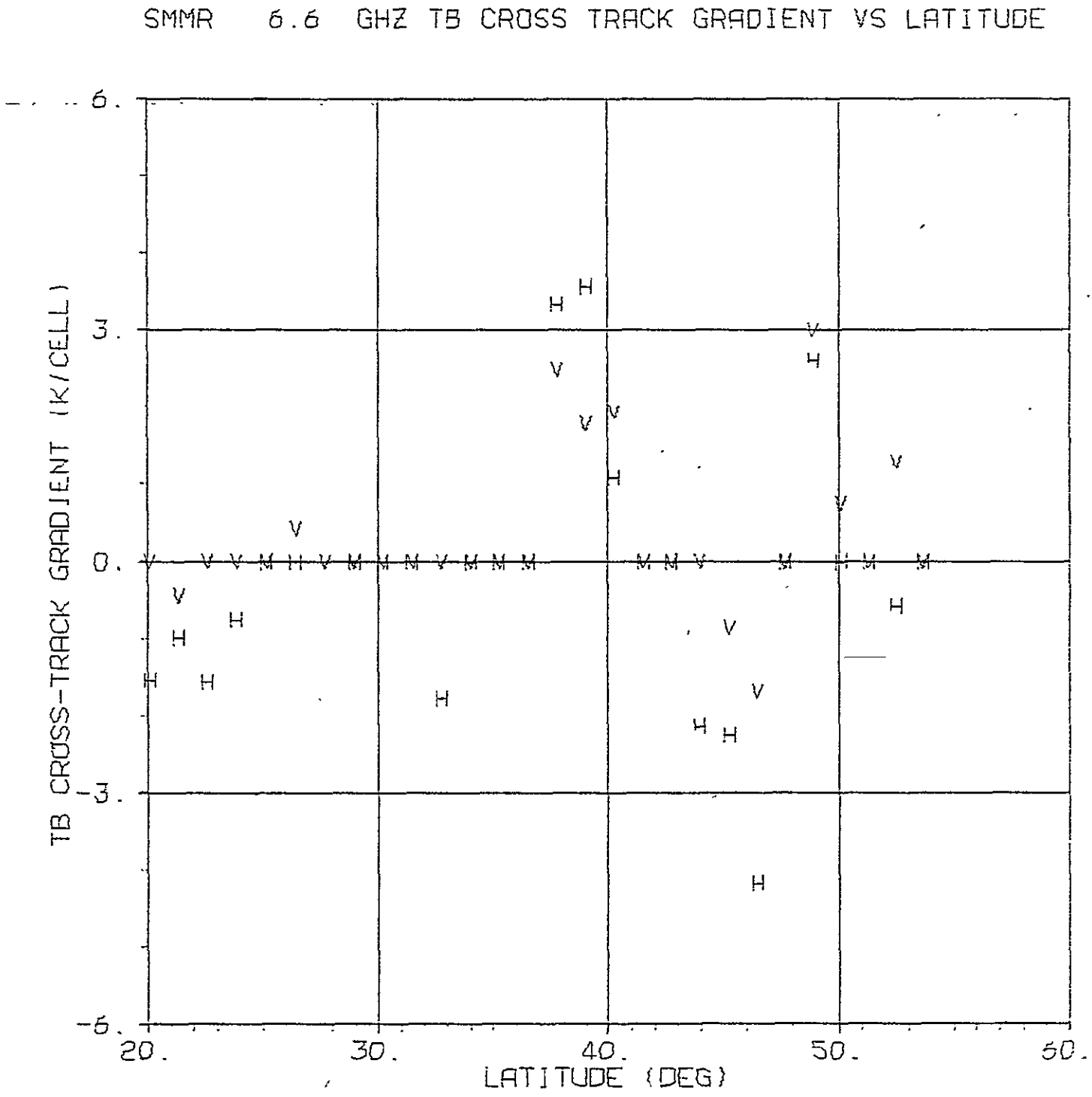

Figure 7.1. Orbit 1212, Final APC

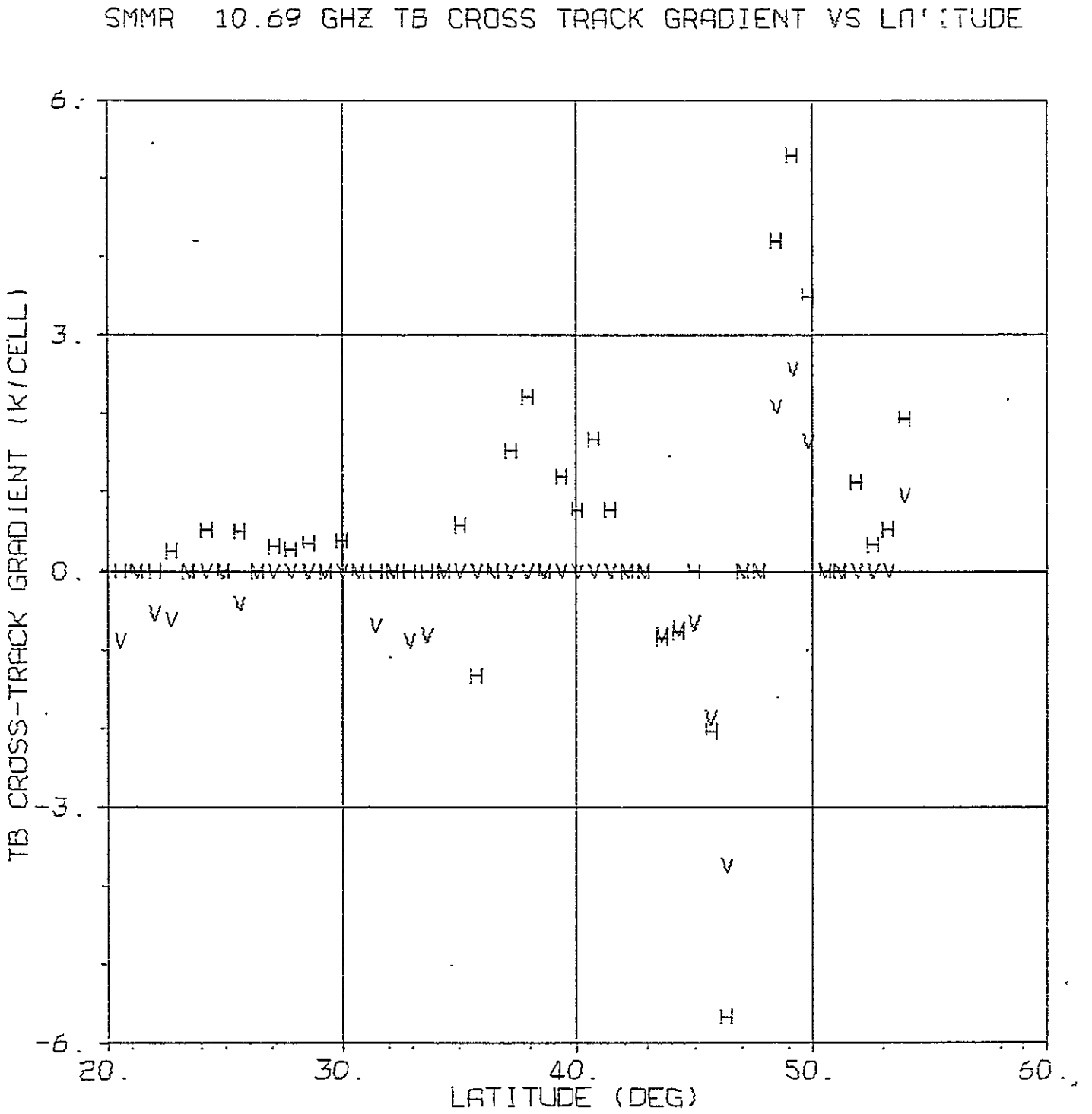

Figure 7.2. Orbit 1212, Final APC

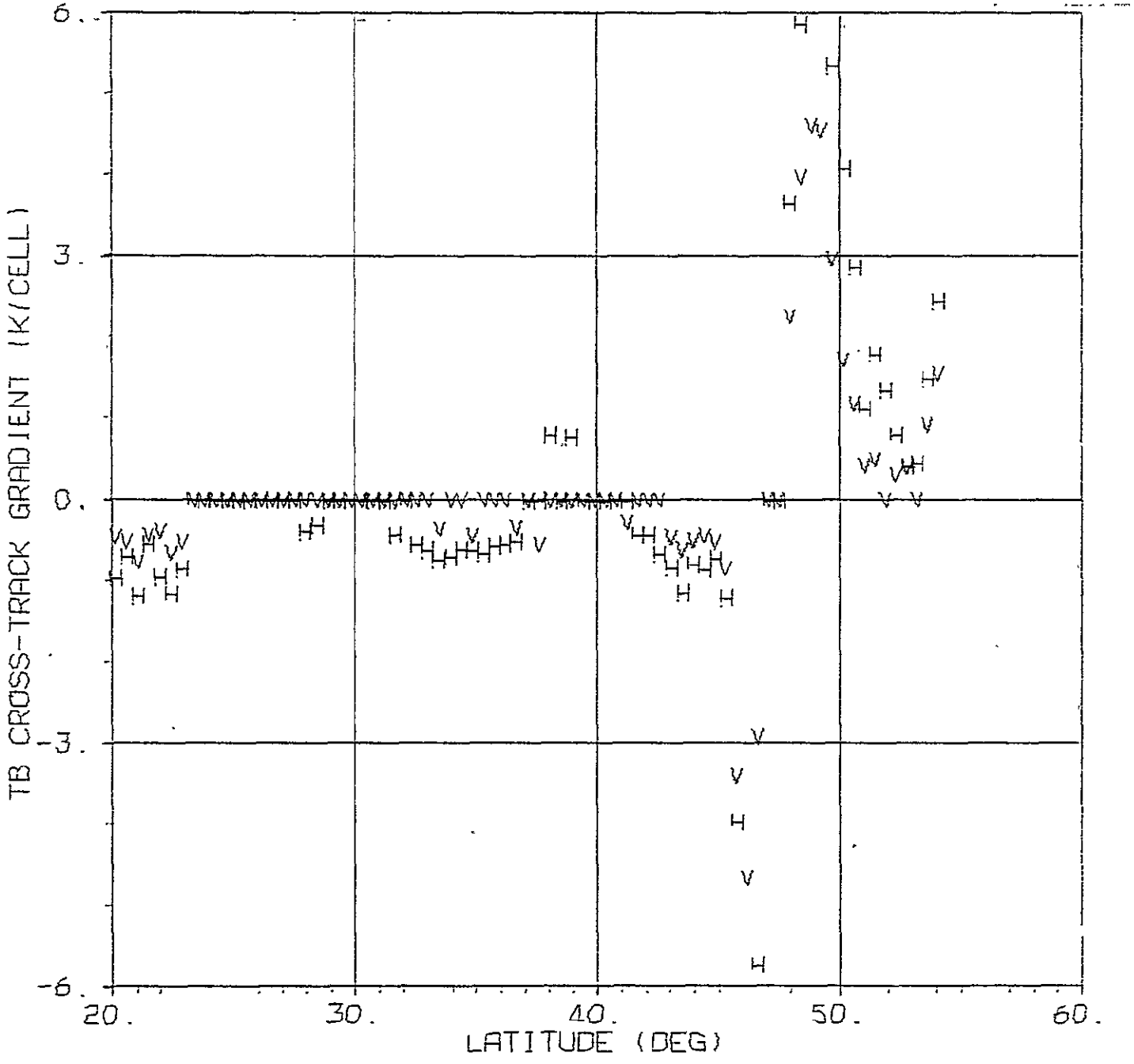

Figure 7.3. Orbit 1212, Final APC

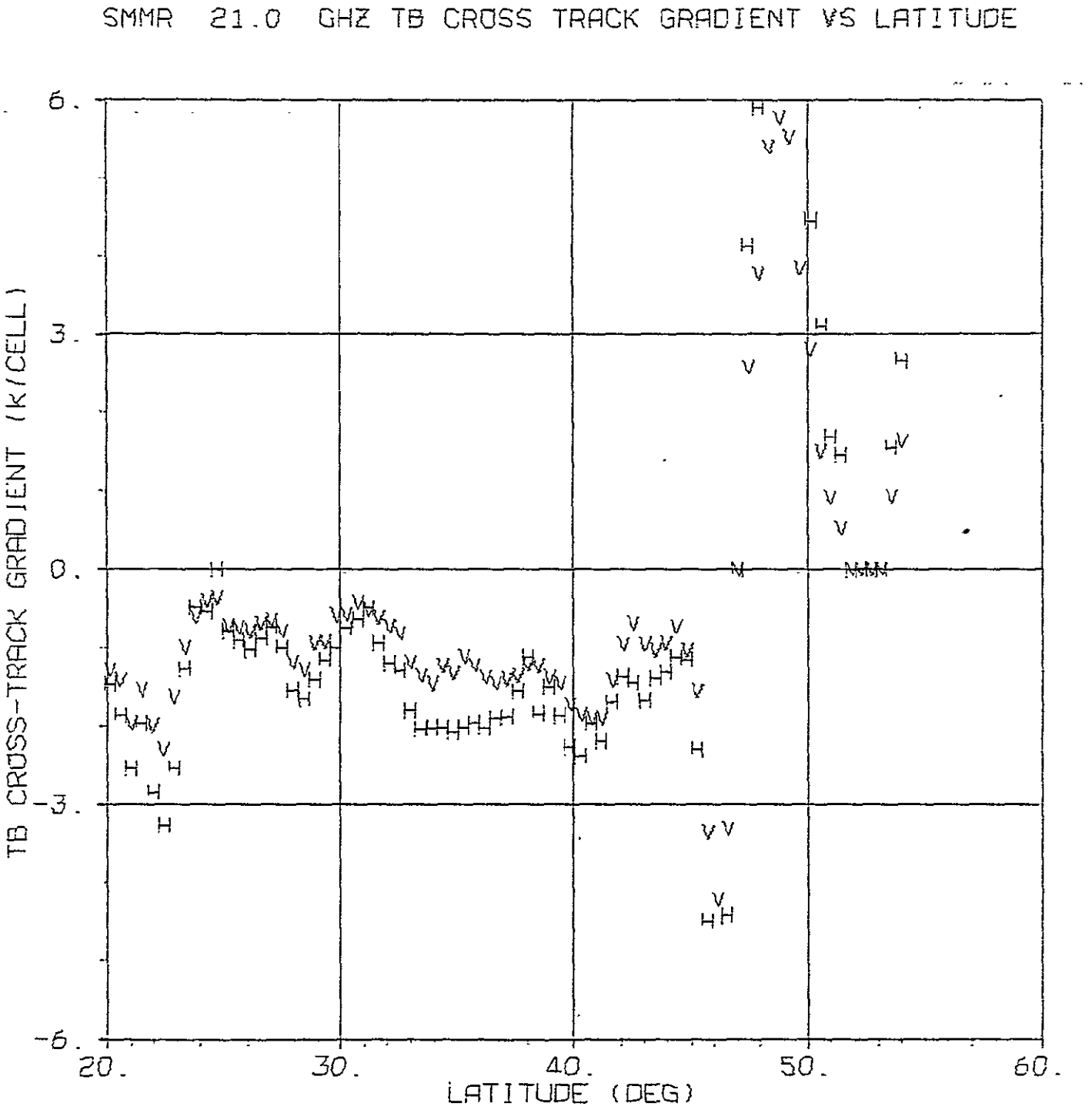

Figure 7.4. Orbit 1212, Final APC

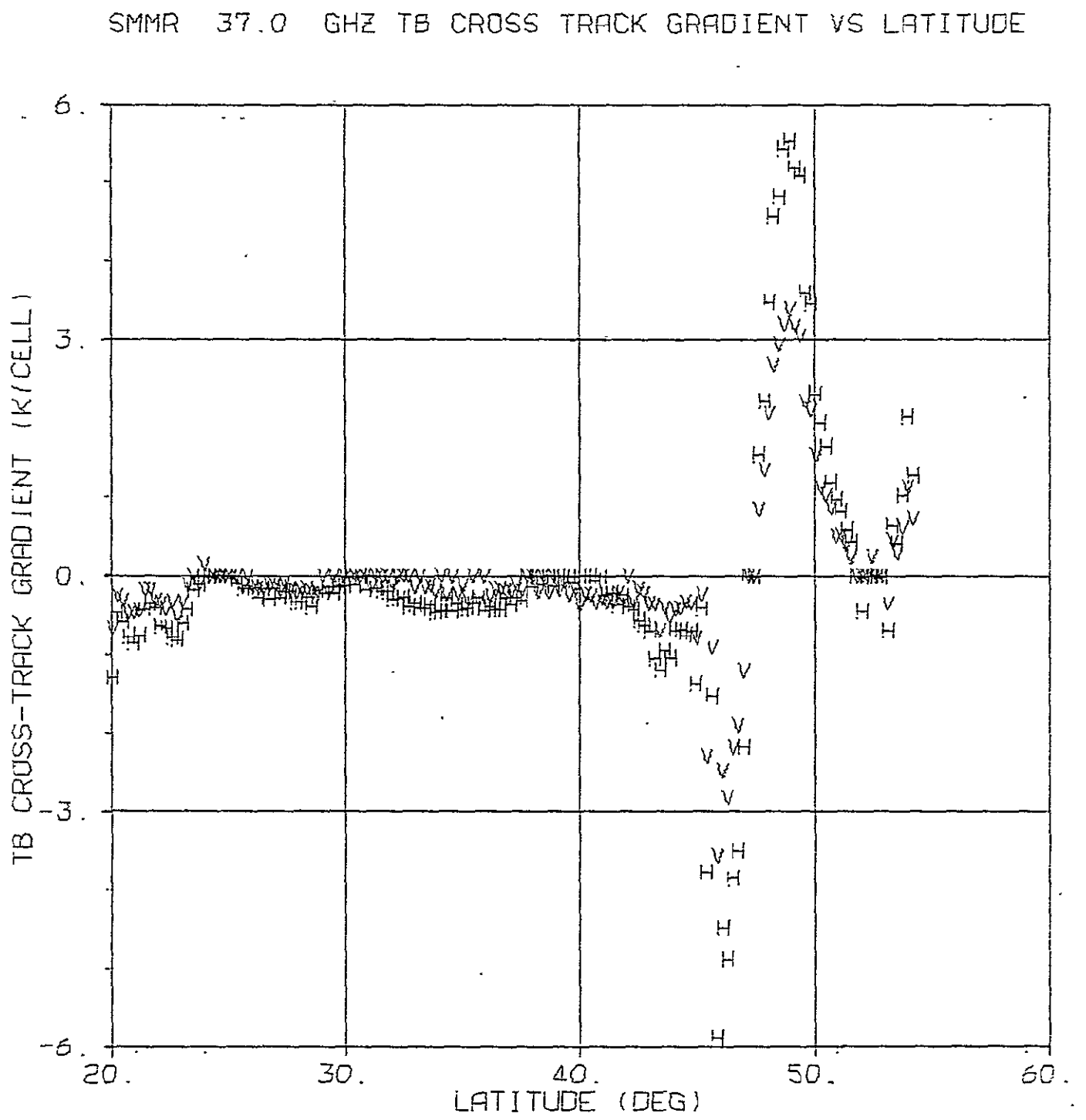

Figure 7.5. Orbit 1212, Final APC

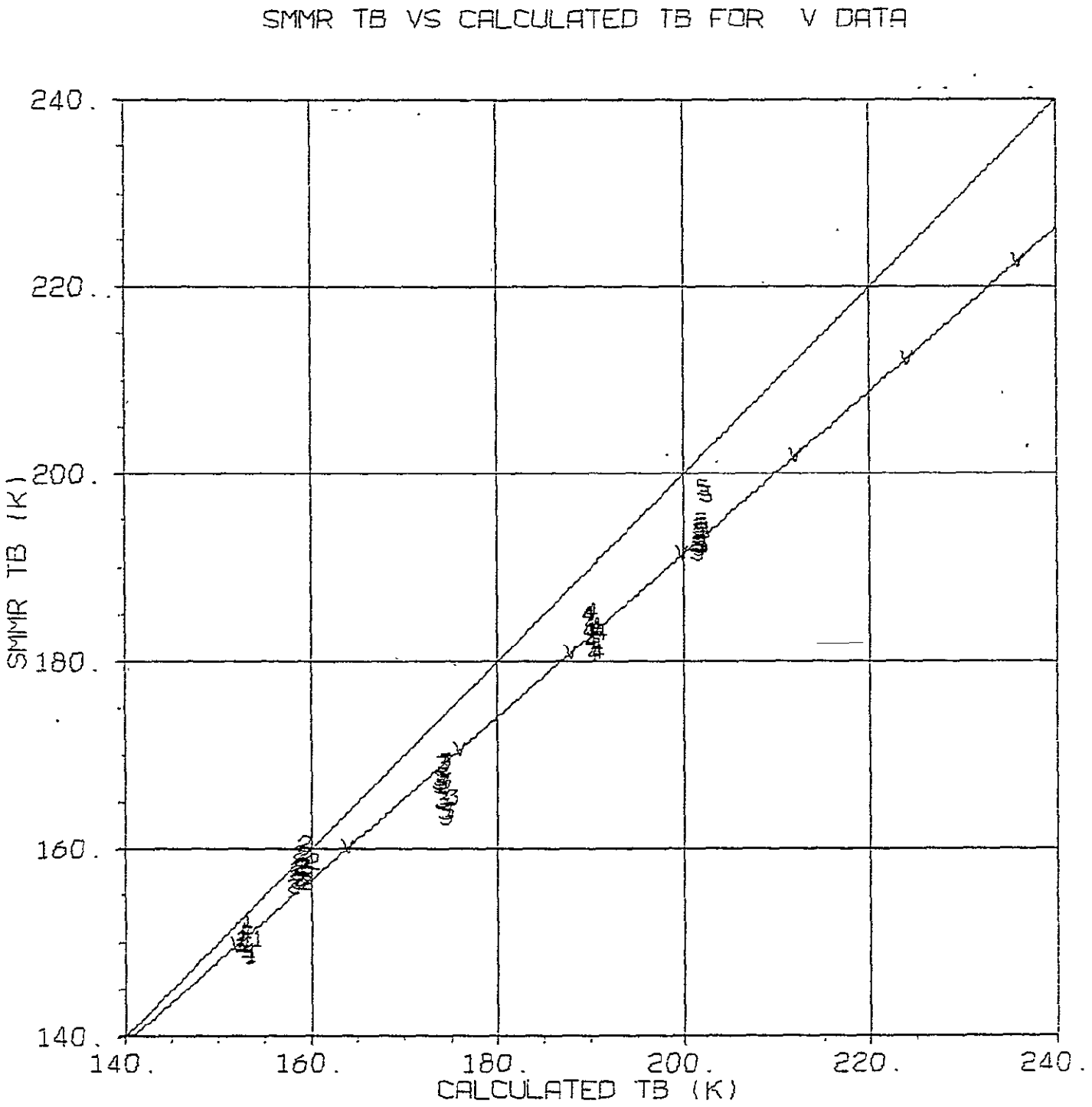

Figure 8.1. Orbit 1135, 46° N. to 52° N., Interim APC

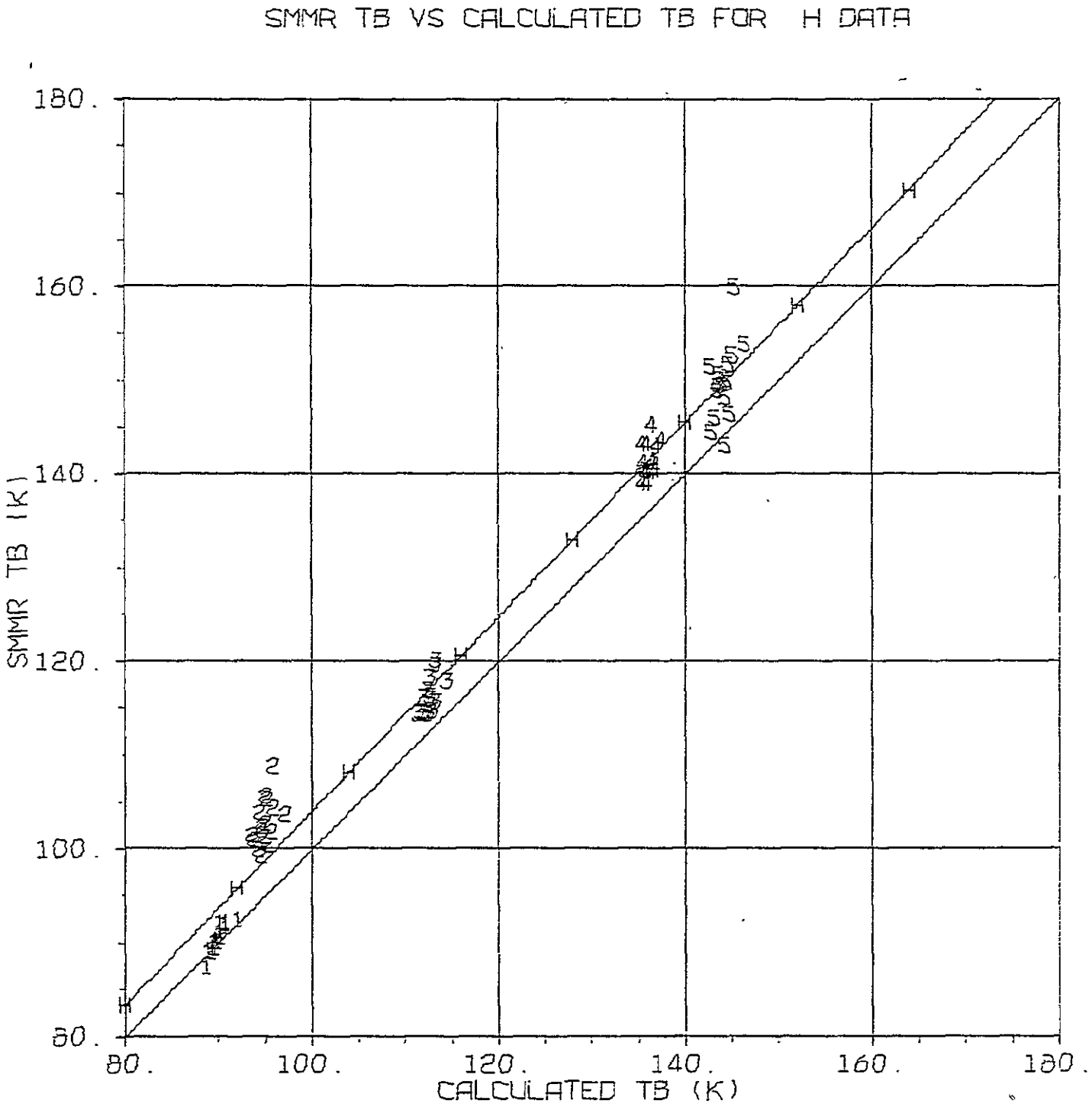

Figure 8.2. Orbit 1135, 46° N. to 52° N., Interim APC

Table 8. Observed Biases, Orbit 1135, 46° N. to 52° N. Interim APC

CHANNEL	BIAS	RMS ABOUT BIASED CURVE
6.6 V	-2.84	1.201
6.6 H	.60	.739
10.69 V	-1.13	1.109
10.69 H	7.82	2.108
18.0 V	-7.61	1.971
18.0 H	3.68	1.495
21.0 V	-7.06	1.542
21.0 H	5.37	1.592
37.0 V	-8.14	1.725
37.0 H	5.48	3.487
ALL V	-5.35	3.218
ALL H	4.59	3.176
ALL V+H	-.38	5.911

Table 9. Observed Biases, Orbit 1135, 46° N., to 52° N. Final APC

CHANNEL	BIAS	RMS ABOUT BIASED CURVE
6.6 V	-6.47	.927
6.6 H	.74	.890
10.69 V	-5.40	2.947
10.69 H	7.89	3.648
18.0 V	-11.94	2.286
18.0 H	1.53	4.222
21.0 V	-7.11	2.149
21.0 H	.17	2.239
37.0 V	-10.70	5.635
37.0 H	3.28	6.910
ALL V	-8.32	4.082
ALL H	2.72	4.971
ALL V+H	-2.80	7.154

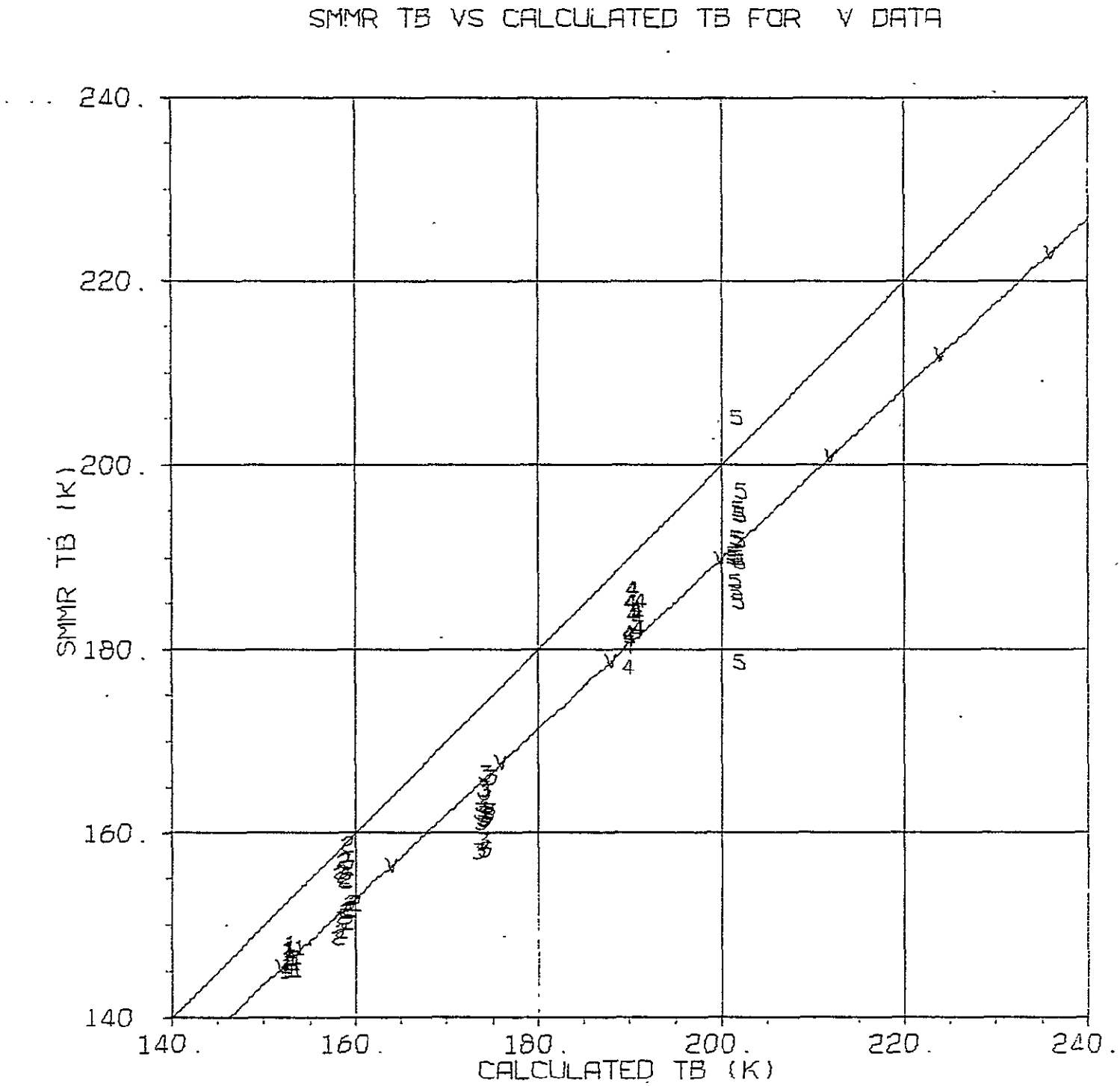

Figure 9.1. Orbit 1135, 46° N. to 52° N., Final APC

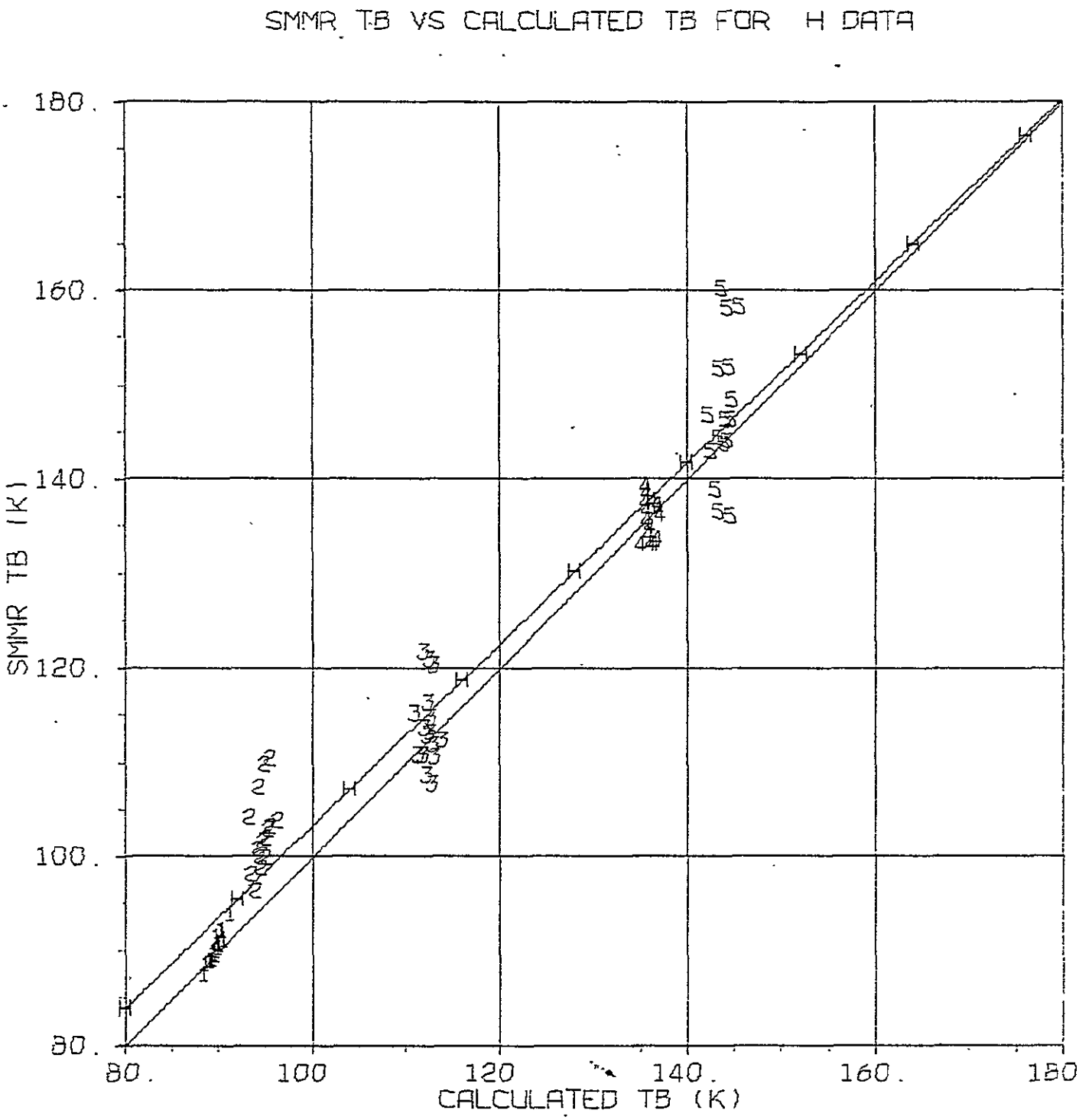

Figure 9.2. Orbit 1135, 46° N. to 52° N., Final APC

Table 10. Cos β Estimates, "Best" Data Set

Channel	Cos β	RMS Around T_A Curve Fit
6.6 V	.03	.13
6.6 H	.21	.57
10.7 V	.06	.32
10.7 H	.04	.21
18 V	-.23	.13
18 H	.23	.16
21 V	-.05	.19
21 H	.31	.62
37 V	.19	.34
37 H	.16	.35

Notes:

"Best" Data Set consists of 103 scans of T_A data taken from the following orbit segments:

Orbit 1126	16°S to 8°S.
Orbit 1198	7°S to 4°S.
Orbit 1255	19°S to 5°S.

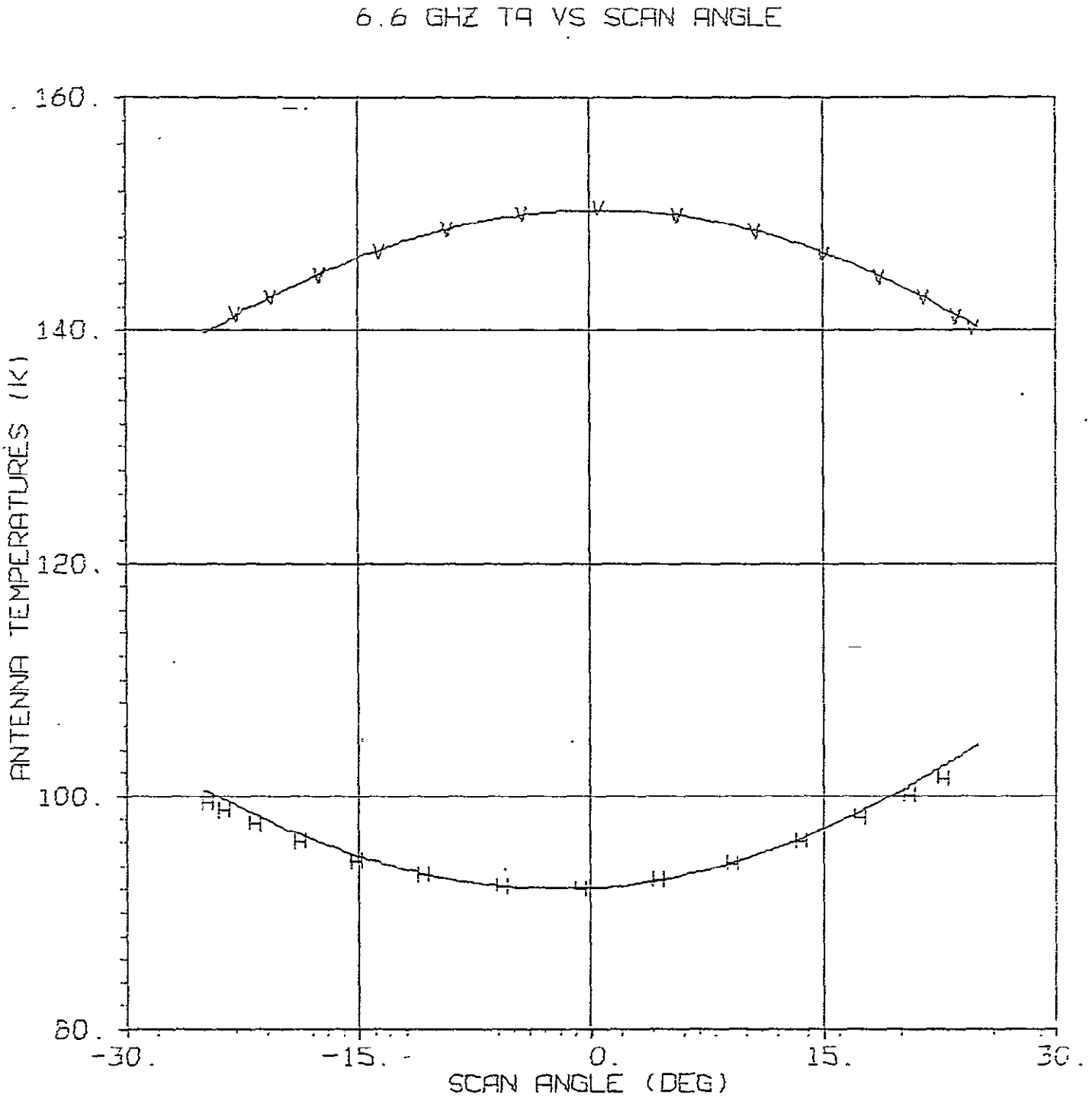

Figure 10.1. "Best" Data Set

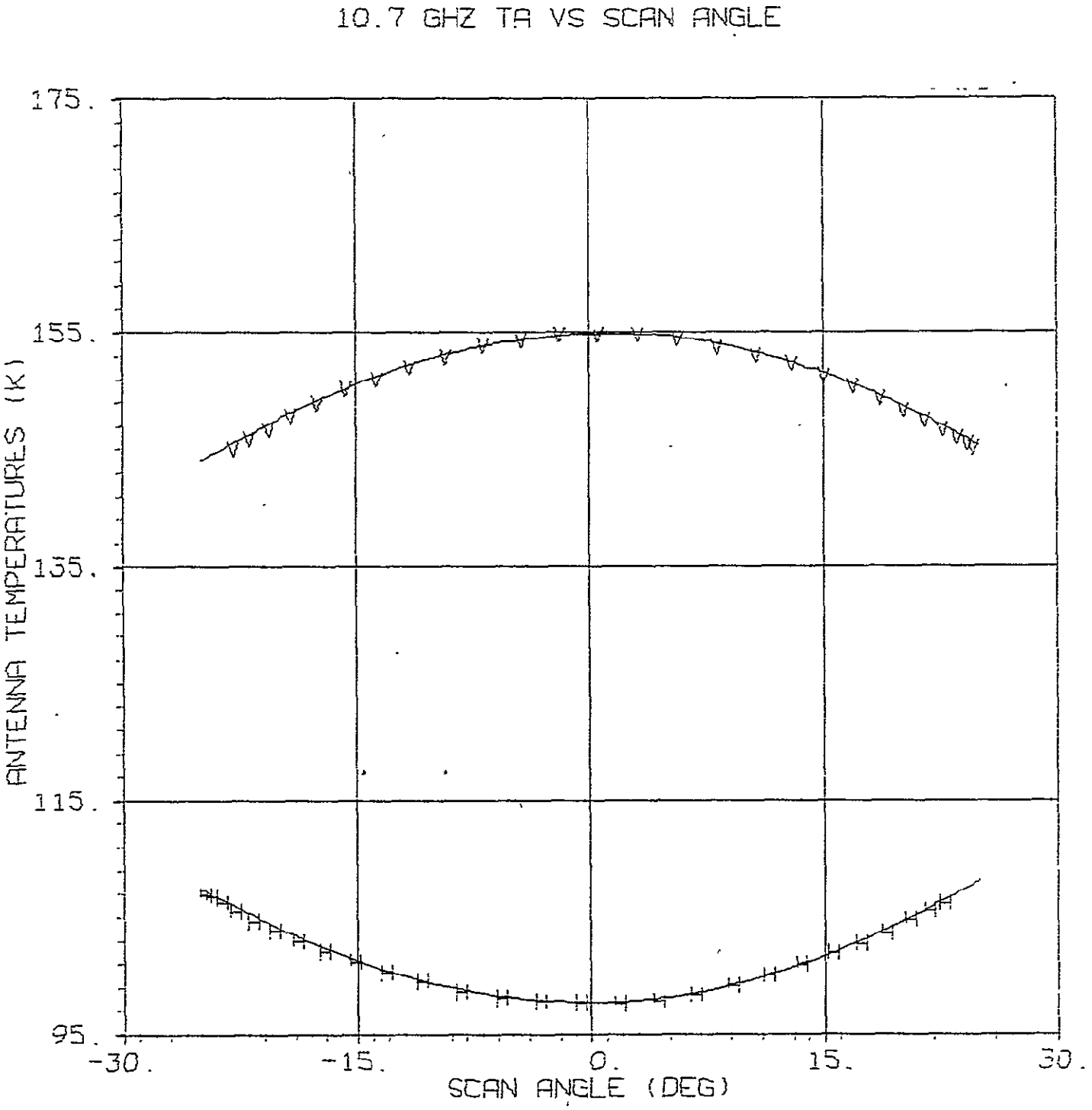

Figure 10.2. "Best" Data Set

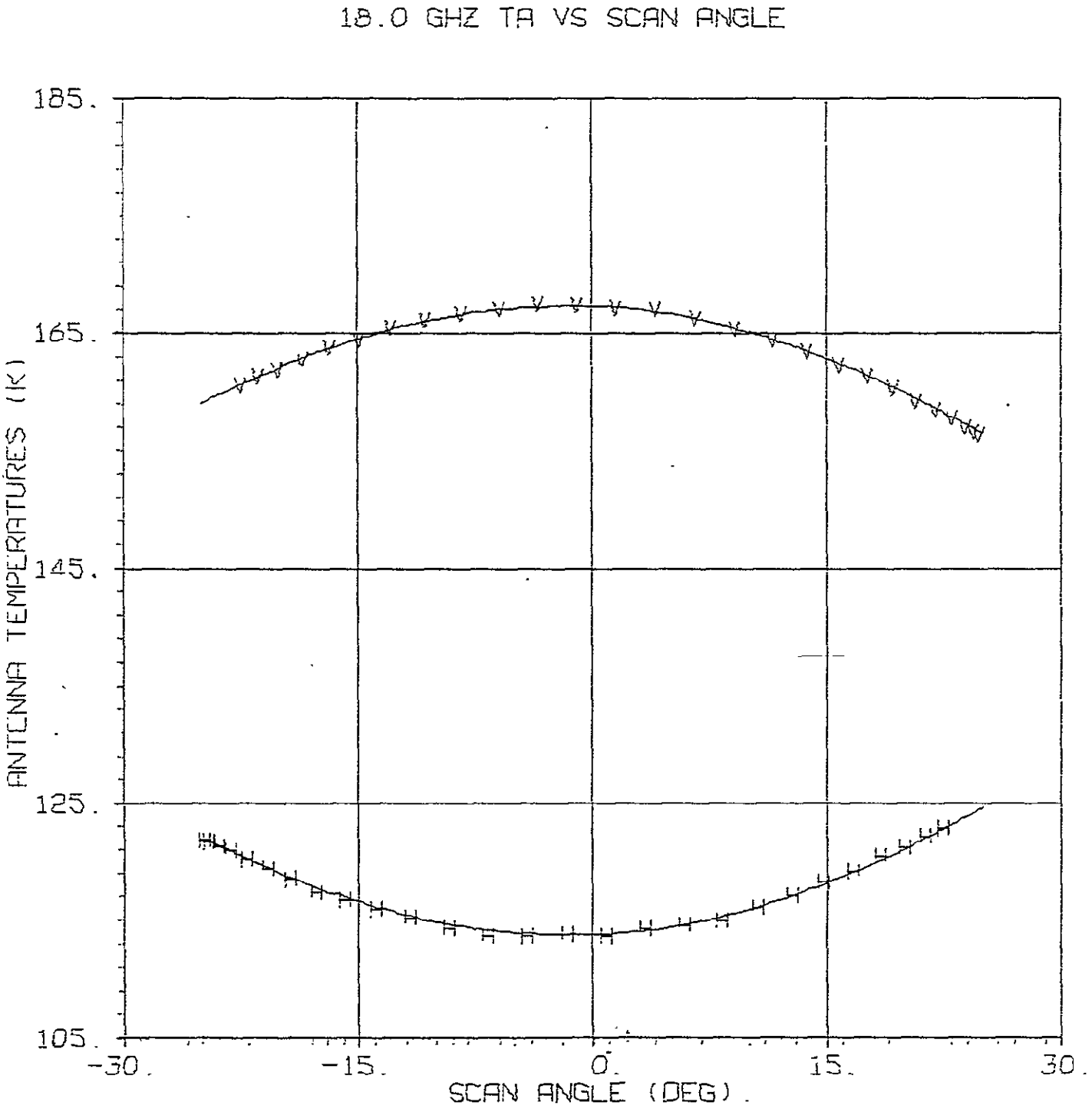

Figure 10.3. "Best" Data Set

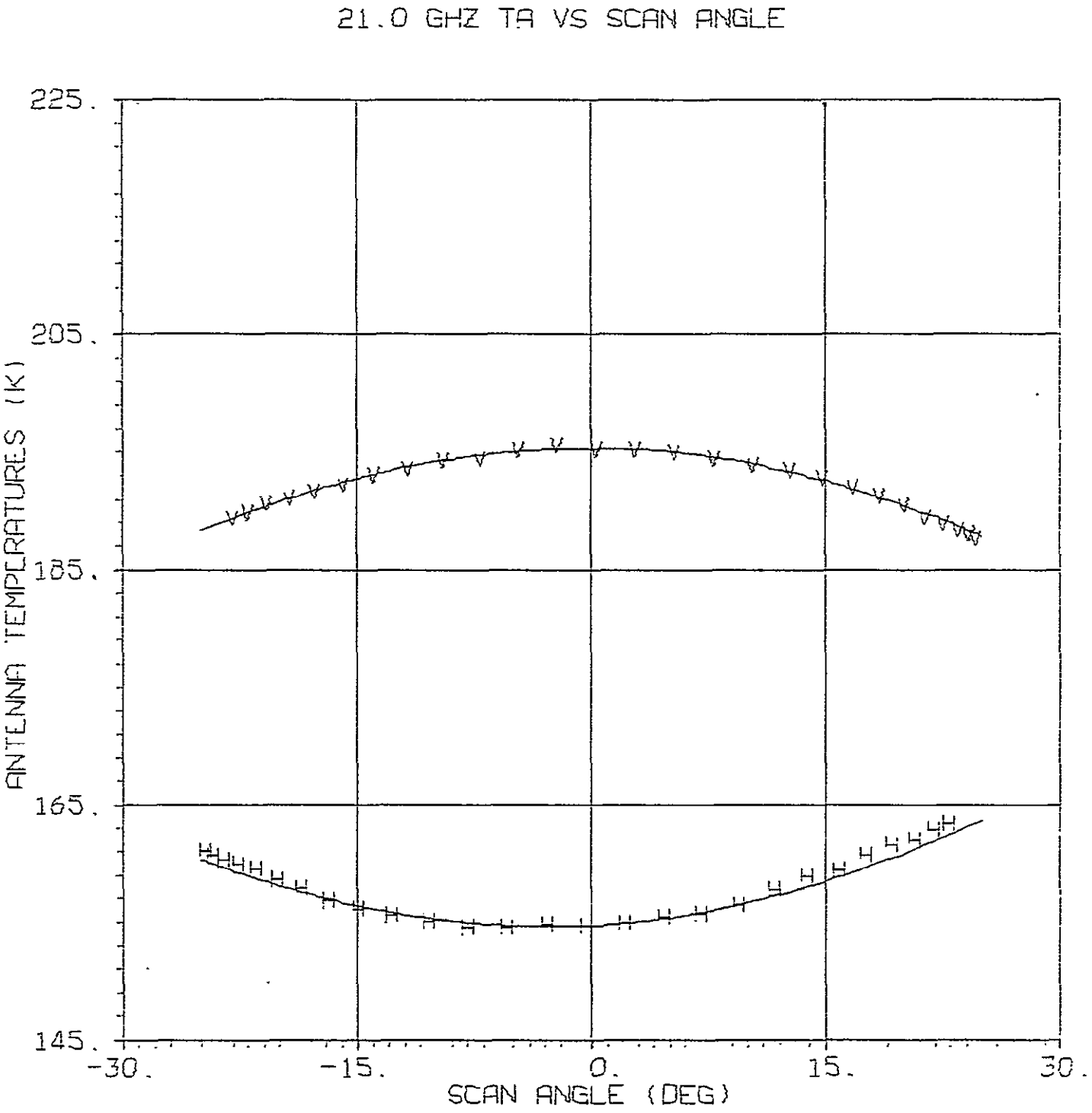

Figure 10.4. "Best" Data Set

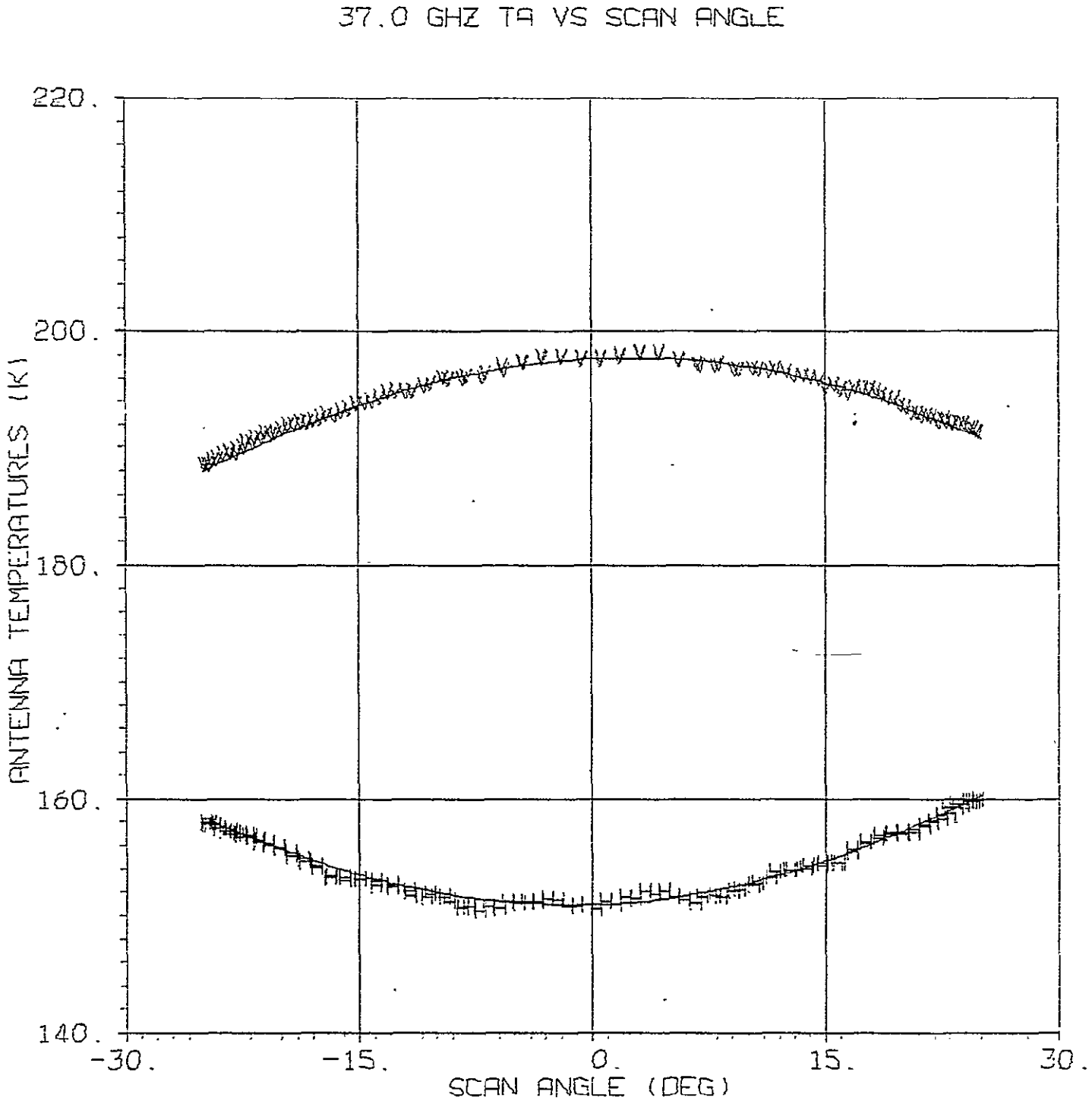

Figure 10.5. "Best" Data Set

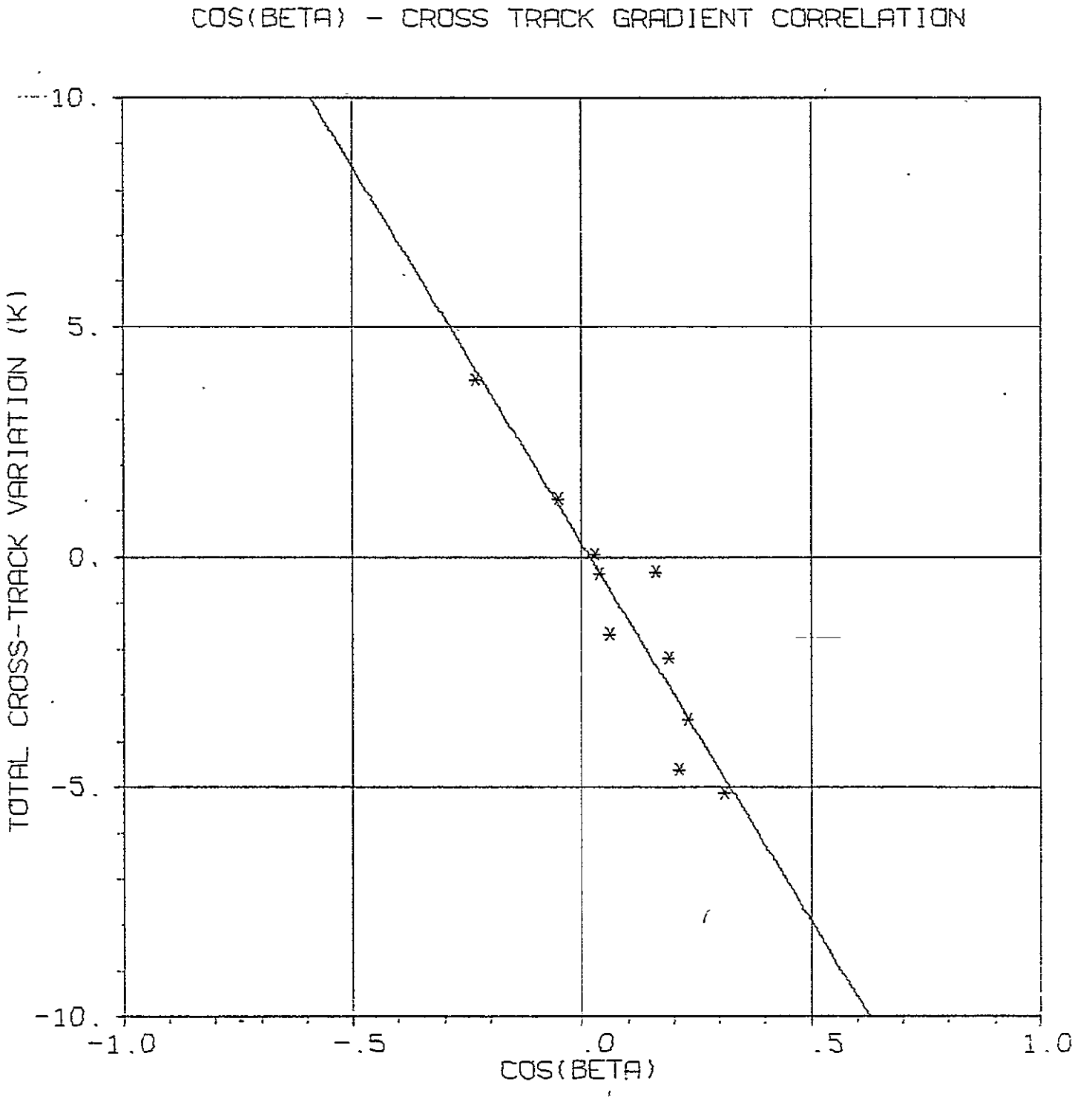

Figure 11.1. "Best" Data Set, Interim APC

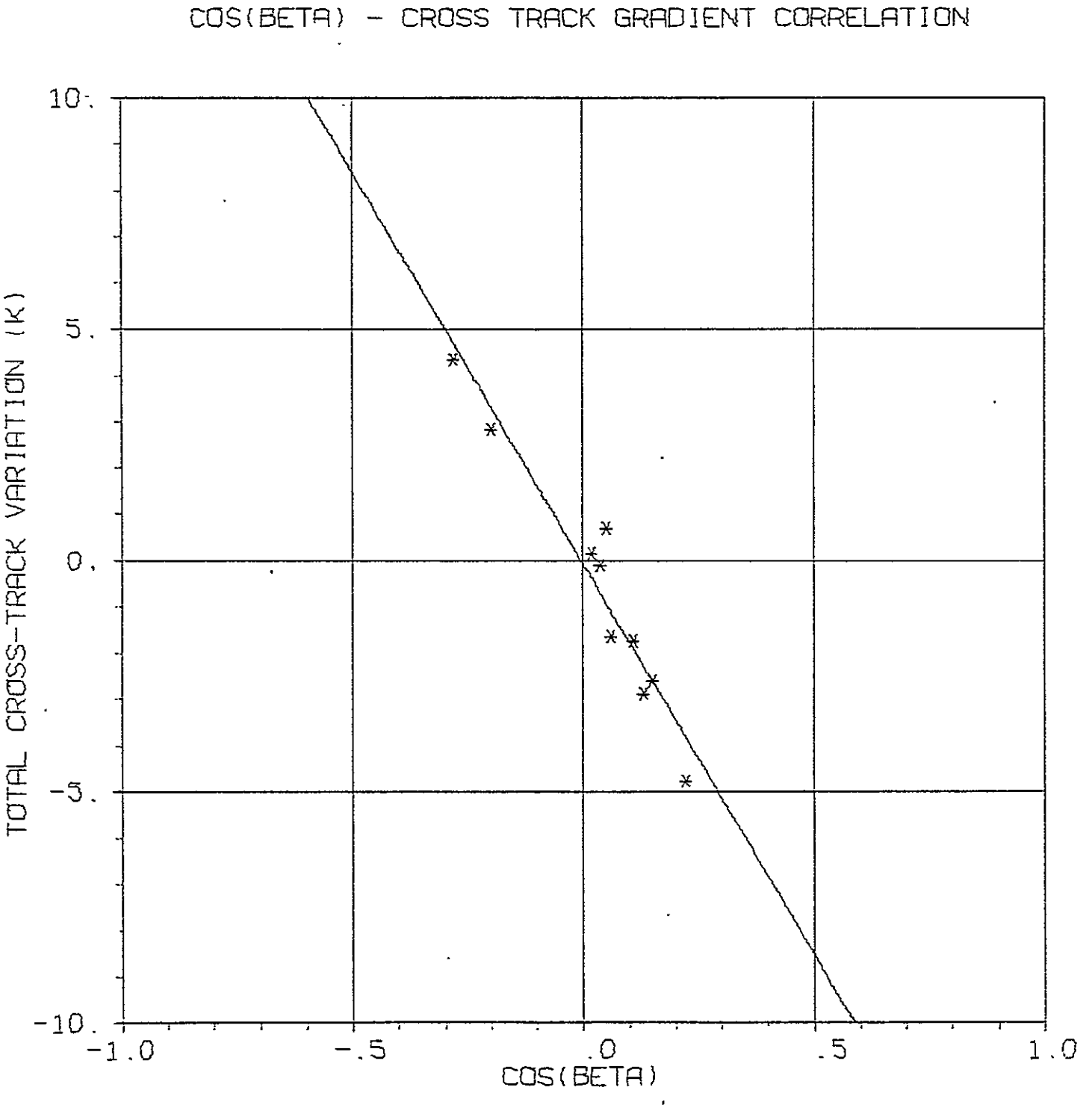

Figure 11.2. Orbit 1255, 25° S. to 5° N., Interim APC

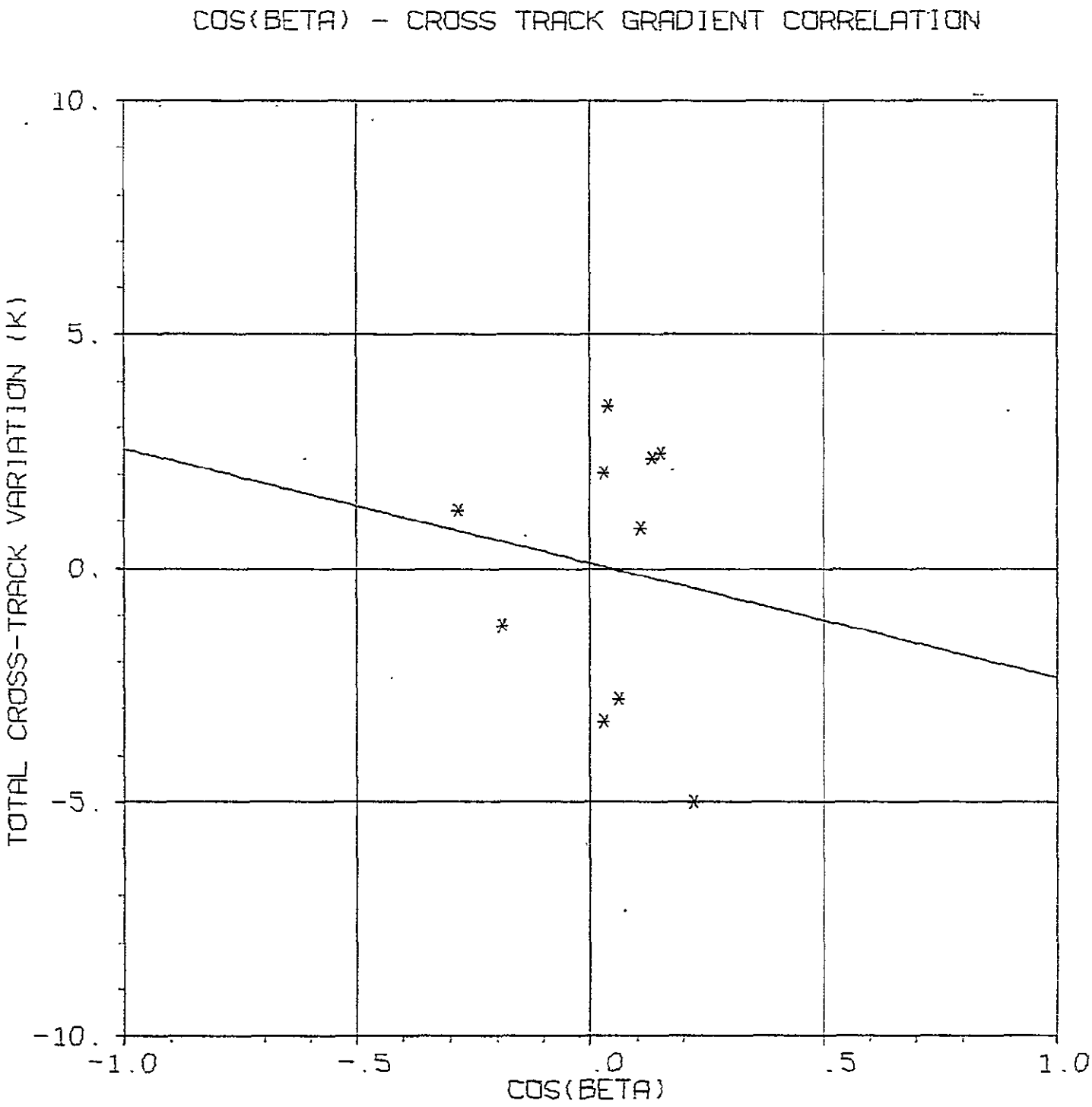

Figure 11.3. Orbit 1255, 25° S. to 5° N., Final APC